Aus dem

Zentrum für Neurologie

Hertie Institut für klinische Hirnforschung

Neuropsychologie der Handlungskontrolle

The functional connectivity of cortical degenerations that are relevant to apraxia in patients with genetic FTD

Inaugural-Dissertation
zur Erlangung des Doktorgrades
der Medizin

der Medizinischen Fakultät
der Eberhard Karls Universität
zu Tübingen

vorgelegt von

Reinermann, Leonie Isabelle

2024

Dekan: Professor Dr. B. Pichler

1. Berichterstatter: Privatdozent Dr. M. Himmelbach
2. Berichterstatter: Professorin Dr. E. Kühn

Tag der Disputation: 18.03.2024

List of contents

List of figures and tables

List of abbreviations

AC:	anterior commissure
AC-PC line:	the line between the anterior and posterior commissure
AD:	Alzheimer's disease
BBR:	Boundary-Based Registration
BOLD:	blood-oxygen-level-dependent
bvFTD:	behavioral variant of Frontotemporal dementia
C9orf72:	chromosome 9 open reading frame 72
CBS:	corticobasal syndrome
CFS:	cerebral spinal fluid
CIFTI:	Connectivity Informatics Technology Initiative
DICOM:	Digital Imaging and Communications in Medicine
DMN:	Default Mode Network
DOF:	degrees of freedom
DPRs:	dipeptide repeat proteins
DTI:	Diffusion Tensor Imaging
FIX:	FMRIB's ICA-based Xnoiseifier
FLIRT:	FMRIB's linear image registration tool
fMRI:	functional Magnetic Resonance Imaging
FNIRT:	FMRIB's nonlinear image registration tool
FoV:	Field of View
FTD:	Frontotemporal dementia
FTLD:	frontotemporal lobar degeneration
FUS:	fused in sarcoma protein
FWER :	family wise error rate correction
FWHM:	Full Width at Half Maximum
GenFI:	Genetic Frontotemporal Dementia Initiative
GIFTI:	Geometry format under the Neuroimaging Informatics Technology Initiative
GM:	grey matter
GRN:	progranulin
HCP:	Human Connectome Project

hcpICA:	data with the automated ICA denoising with FIX as part of the HCP minimal preprocessing pipeline
ICA:	Independent Component Analysis
M+A-:	mutation carriers without apraxia
M+A+:	mutation carriers with apraxia
M-A-:	non-mutation carriers without apraxia
manICA:	data with manual ICA denoising during the preprocessing
MAPT:	microtubule-associated protein tau
MELODIC:	Multivariate Exploratory Linear Optimized Decomposition into Independent Components
MND:	motor neuron disease
NfL:	neurofilament light chain protein
Nfs:	neurofilaments
NIfTI:	Neuroimaging Informatics Technology Initiative
noICA:	data without ICA denoising during the preprocessing
pMTG:	posterior middle temporal gyrus
PPA:	primary progressive aphasia
PSP-S:	progressive supranuclear palsy syndrome
ROI:	region of interest
ROIall:	region of interest where all 3 seed regions, ROI1, ROI2 and ROI3, were combined into one region of interest
rs-fMRI:	Resting state functional Magnetic Resonance Imaging
SD:	semantic dementia
SMA:	supplementary motor area
TDP-43:	TAR DNA-binding protein
TE:	echo time
TI:	inversion time
TR:	repetition time
t-tau:	total tau

1 Introduction

Frontotemporal dementia (FTD) is a heterogeneous group of progressive neurodegenerative diseases characterized by atrophy of the frontal and anterior temporal cortex (Devenney et al., 2019, Neary et al., 1998). It is the second most common cause of presenile dementia (Seelaar et al., 2008, Snowden et al., 2002), with a prevalence of 15 / 100,000 at age 45-64 years (Ratnavalli et al., 2002). FTD is an early-onset dementia, typically beginning before the age of 65 years, with the mean age at onset usually at 52.8 years (Ratnavalli et al., 2002). Frontotemporal dementia thus occurs significantly earlier than Alzheimer's disease (AD) with the mean age at onset usually at 80 years (Ratnavalli et al., 2002, Neary et al., 1998, Masters et al., 2015).

The term frontotemporal lobar degeneration (FTLD) encompasses various clinical syndromes, all of which are associated with degeneration of the frontotemporal cortex (Olney et al., 2017). Originally, FTLD was divided into 3 clinical syndromes: behavioral variant FTD (bvFTD), primary progressive aphasia (PPA) and semantic dementia (SD) (Neary et al., 1998). There is an overlap with motor neuron disease (MND), progressive supranuclear palsy syndrome (PSP-S) and corticobasal syndrome (CBS), which is why these are now included in the FTLD spectrum as well (Seelaar et al., 2011, Olney et al., 2017). Behavioral variant FTD is the most common clinical manifestation of FTLD (Neary et al., 1998). It is mainly characterized by a deterioration of social functions and personality. In addition, there is a loss of insight, economic speech output leading to mutism, and cognitive deficits in attention, abstraction, planning and problem solving (Neary et al., 1998). Memory functions are relatively preserved in FTD especially in early stages of the disease, unlike AD (Neary et al., 1998). PA is an expressive language disorder with difficulties in speech production, phonological and grammatical errors and word retrieval difficulties, as well as difficulties in reading and writing, while understanding the meaning of words is preserved (Neary et al., 1998). SD, on the other hand, is characterized by a loss of semantics, the understanding of verbal and non-verbal concepts. There is fluent, effortless, grammatically correct speech output (Neary et al., 1998). Over the

course of the disease, the symptoms of the different syndromes may overlap (Neary et al., 1998).

The term FTLD is an accepted umbrella term for pathologies specific to FTD subtypes (Devenney et al., 2019). The term FTD is often used inconsistently in the literature. While in many publications it is used to refer only to the most common clinical syndrome of the FTLD spectrum, behavioral variant frontotemporal dementia, in many other publications it is used as an umbrella term for all clinical syndromes of the FTLD spectrum. I will use the term FTD in the following to refer to all FTLD spectrum disorders. The pathology of FTD is characterized by severe focal atrophy of the frontal and temporal regions, subcortical gliosis and neuronal loss (Devenney et al., 2019). In contrast, patients with AD show grey matter atrophy bilaterally in the frontal, parietal, temporal and occipital lobes (Du et al., 2007), particularly pronounced in the posterior temporoparietal and occipital cortex (Rabinovici et al., 2007). Patients with FTLD have selective atrophy of the anterior cingulate, frontal insula, subcallosal gyrus and striatum compared to patients with AD (Rabinovici et al., 2007). Although AD and FTD differ in the location of atrophy, there is also considerable anatomical overlap between the two disorders (Rabinovici et al., 2007). For example, FTD can also cause atrophy in the hippocampus and parietal cortex (Rabinovici et al., 2007). Therefore, although hippocampal atrophy is very sensitive for AD, it is not very specific compared to FTLD (Likeman et al., 2005). In early-onset AD, there is often a loss of volume in the dorsolateral prefrontal cortex (Rabinovici et al., 2007), which is usually more typical for FTD. A good distinction between AD and FTD is possible based on the thickness or volume of the parietal cortex (Du et al., 2007). Posterior more than anterior gradient of atrophy is highly specific for AD when compared to other pathologies such as FTLD (Likeman et al., 2005). AD and FTLD are thus anatomically distinctive, AD being characterized by degenerations of the posterior parietal network, while FTLD shows degenerations of the paralimbic fronto-insular-striatal network (Rabinovici et al., 2007).

FTD presents with intraneuronal protein inclusions. Three main proteins have been identified in FTD: phosphorylated tau protein or ubiquitinated TAR DNA-binding protein (TDP-43) account for the majority of protein inclusions, while

fused in sarcoma (FUS) protein is rarely found (Warren et al., 2013, Devenney et al., 2019). In contrast, AD is characterized by extracellular deposition of Aβ fibrils and an intraneuronal accumulation of abnormally phosphorylated tau protein (Kovacs, 2017). While specific biomarkers exist for AD, these are still lacking for primary tauopathies or TDP-43 proteinopathies (Swift et al., 2021). The cerebral spinal fluid (CSF) profile of AD patients is characterized by reduced levels of amyloid-β42, increased levels of p-tau181 and increased total tau (t-tau) and is also used in clinical practice to detect AD (van der Ende and van Swieten, 2021). In FTD, on the other hand, Aβ42 and p-tau181 are normal, while t-tau can be normal or increased (van der Ende and van Swieten, 2021). Particularly good differentiation of AD from FTD is achieved using the tau/amyloidβ42 ratio in CSF, which is elevated in AD but lower in FTD (Swift et al., 2021, van der Ende and van Swieten, 2021). This is clinically very helpful, as it can distinguish atypical forms of AD from FTD (Swift et al., 2021). Neurofilament light chain protein (NfL) is thought to be an important diagnostic, prognostic and staging marker for FTD (Swift et al., 2021). It is currently the most promising fluid biomarker for FTD (van der Ende and van Swieten, 2021). Neurofilaments (Nfs) are intracellular filaments that are exclusively localized in the neuronal cytoplasm and, as part of the axonal cytoskeleton, maintain cell structure and control axonal diameter (Swift et al., 2021, van der Ende and van Swieten, 2021). In the event of neuronal damage, the neurofilaments leak out and can thus be found in the CSF, as well as in the blood by crossing the blood-brain barrier (Swift et al., 2021, van der Ende and van Swieten, 2021). Nfs thus reflect neuroaxonal damage (van der Ende and van Swieten, 2021). Since it does not matter how this damage occurred, elevations of NfL in CSF and blood occur in several neurological diseases, such as dementia, stroke, traumatic brain injury, multiple sclerosis and Parkinson's disease (van der Ende and van Swieten, 2021). However, it has been shown that despite the overlap with other diseases, significantly higher NfL levels can be found in FTD than in other common causes of dementia, including AD, vascular dementia and Lewy body dementia (Bridel et al., 2019, van der Ende and van Swieten, 2021). In addition, NfL can be used to clearly differentiate FTD from non-neurodegenerative diseases, primarily psychiatric diseases resulting in

similar symptoms (Swift et al., 2021, van der Ende and van Swieten, 2021). In addition to increased NfL levels, progranulin in blood and CSF can be measured in patients with a progranulin (GRN) mutation who have a haploinsufficiency that leads to reduced progranulin (Swift et al., 2021). This is already possible in pre-symptomatic patients (van der Ende and van Swieten, 2021). Chromosome 9 open reading frame 72 (C9orf72) hexanucleotide repeat expansions result in dipeptide repeat proteins (DPRs) (Swift et al., 2021). One of these DPRs, poly(GP), could be measured in the CSF of both pre-symptomatic and symptomatic patients in previous studies (Swift et al., 2021, van der Ende and van Swieten, 2021).

So far, there is no effective pharmacological treatment for FTD (Devenney et al., 2019). The average time between the onset of the first symptoms and death is eight years (Snowden et al., 2002). Therefore, it is particularly important to gain a better understanding of genetic frontotemporal dementia that can be used to track its progression, as it has an important role in therapeutic studies.

FTD is a highly heritable disease (Rohrer et al., 2009), with 30-50% of FTD patients having an autosomal dominant mode of inheritance (Rohrer and Warren, 2011, Chow et al., 1999). The most common genetic causes are mutations in progranulin (GRN), microtubule-associated protein tau (MAPT) or hexanucleotide repeat expansion in C9orf72 (Rohrer and Warren, 2011, Olney et al., 2017). In recent years, other genes associated with autosomal dominant FTD have been identified, however cumulatively these account for less than 5% of cases of genetic FTD and most of these genes have only been found in a small number of families (Greaves and Rohrer, 2019). These are valosin-containing protein (VCP), chromatin-modifying protein 2B (CHMP2B), transactive DNA-binding protein (TARDP), fused in sarcoma (FUS) (Rohrer and Warren, 2011), SQSTM1, CHCHD10, TBK1 (which has now been identified as the fourth most common mutation), OPTN, CCNF and TIA1 (Greaves and Rohrer, 2019).

The Genetic Frontotemporal Dementia Initiative (GenFI) studies genetic FTD. As FTD is a rare disease and individual study centers only have the opportunity to study a small number of participants, the GenFI consortium was formed in 2011

to form a larger cohort for future clinical trials (Rohrer et al., 2013). The GenFI Consortium is a group of research centers in Europe (UK, Netherlands, Belgium, France, Spain, Portugal, Italy, Germany, Sweden and Finland) and Canada. Subjects are included who are either known carriers of a mutation in MAPT, GRN or C9orf72 or who have a 50% risk of developing FTD because they are first-degree relatives of FTD patients (Rohrer et al., 2013, Rohrer et al., 2015). By including such pre-symptomatic or at-risk subjects, it is possible to understand the development of frontotemporal dementia from the onset of the first changes (Rohrer et al., 2015, Rohrer et al., 2013). Ideally, therapies should be started while there is still a minimum of irreversible neuronal loss. Therefore, it is important to find biomarkers that can predict when it would be most beneficial to initiate disease-modifying therapies (Rohrer et al., 2013). Previous studies have already shown a sequence of changes in various potential biomarkers of genetic FTD before clinical onset with symptoms. First, there are changes in plasma and CSF, then changes in functional and structural connectivity, followed by grey matter atrophy and finally neuropsychometric abnormalities close to the first symptoms (Rohrer et al., 2013). It has been shown that changes in structural imaging and cognitive changes can be identified 5-10 years before the expected onset of symptoms in pre-symptomatic adults at genetic risk for frontotemporal dementia (Rohrer et al., 2015). The main goal of the GenFI consortium is to determine markers for disease onset as well as markers for disease progression, which can then be used as outcome measures (Rohrer et al., 2015, Rohrer et al., 2013).

Apraxia is a specific neurological symptom whose relevance in FTD is potentially overlooked. Past studies have shown that limb apraxia is a common early symptom in bvFTD (Johnen et al., 2016) and apraxias are evident in all clinical variants of FTD within the first 4 years of the disease (Yliranta and Jehkonen, 2020). Apraxia is an acquired cognitive-motor disorder (Foundas and Duncan, 2019) characterized by the inability to perform specific and predefined actions or learned skilled movements in the absence of motor, sensory, coordination deficits or a lack of understanding or cooperation (Cubelli, 2017, Foundas, 2013, Park, 2017). The core manifestations of apraxia are difficulties in imitating gestures,

use of single tool and object and production of communicative gestures on command (Goldenberg, 2014). Apraxia occurs in several neurological disorders such as stroke, dementia or other neurodegenerative diseases such as Parkinson's and corticobasal degeneration and many developmental disorders (Foundas and Duncan, 2019, Park, 2017). There is no widely used standardized method or validated neuropsychological test that evaluates apraxia (Park 2017, Foundas 2013). Most test batteries used in clinical practice include imitation of meaningful and meaningless actions, pantomime of object use without the object, and demonstration of object use with the tool (Buxbaum and Randerath, 2018). First descriptions of apraxia can be traced back to Liepmann, who observed that patients with left hemispheric lesions, but not with right hemispheric lesions, were unable to perform goal-directed and learned skilled movements (Park, 2017). He postulated that motor planning takes place in the left hemisphere (Park, 2017). Using lesion symptom mapping of tool use and imitation of meaningless gestures, it has been shown that the left frontoparietal-temporal network is involved in these tasks (Buxbaum and Randerath, 2018). According to the praxis network model, representations of learned skilled movements, i.e. visuokinesthetic engrams are stored in the left inferior parietal lobe, while computations controlling these goal-directed movements are conducted by the left prefrontal cortex (Foundas and Duncan, 2019). Apraxia occurs when there is damage to different localizations in the densely interconnected network of regions in the left temporal, parietal and frontal lobes (Buxbaum and Randerath, 2018). To date, studies to understand the neural correlates of apraxia have been conducted predominantly in stroke patients. The neural correlates of limb apraxia in FTD are not well understood. In patients with bvFTD, Johnen et al. (2016) showed bilateral atrophy of the superior, inferior and middle parietal cortex for limb imitation, and atrophy of the right middle temporal and angular gyrus for object pantomime. Wabersich-Flad (Doctoral thesis, Faculty of Medicine, Eberhard Karls Universität Tübingen, 2021), on the other hand, found a significant focal reduction in cortical thickness in the premotor cortex, inferior frontal and frontal opercular regions specific for apraxia in genetic FTD, but not in the inferior parietal cortex. Hence, we asked whether, in addition to the focal degenerations in the frontal cortex found by

Wabersich-Flad (Doctoral thesis, Faculty of Medicine, Eberhard Karls Universität Tübingen, 2021), functional connectivity with the inferior parietal cortex is also altered in patients with apraxia and genetic FTD. This study therefore aimed to identify the functional networks associated with the apraxia-specific frontal degenerations found by Wabersich-Flad (Doctoral thesis, Faculty of Medicine, Eberhard Karls Universität Tübingen, 2021) to gain a better understanding of the neural correlates of apraxia in genetic FTD.

Connectivity is defined as how two brain regions interact with each other (Bijsterbosch et al., 2017, Smitha et al., 2017). Anatomical connectivity is the physical connection between two anatomical areas of the brain and can be determined by diffusion tensor imaging (DTI) (Smitha et al., 2017). Functional connectivity is defined as the temporal correlation between two electrophysiological or neurophysiological measurements in different areas of the brain (Bijsterbosch et al., 2017). There does not necessarily have to be a direct anatomical connection between brain regions to allow for functional connectivity, which can occur through indirect anatomical connections. Resting state functional magnetic resonance imaging (rs-fMRI) can be used to investigate functional connectivity. Resting state fMRI examines spontaneous low frequency fluctuations in the range of 0.01-0.08 Hz in the blood-oxygen-level-dependent (BOLD) signal in the absence of explicit tasks or other input (Smitha et al., 2017). The BOLD signal is an indirect measurement of neuronal activity (Bijsterbosch et al., 2017), which leads to an increase in blood flow via a hemodynamic response. This regional increase in blood flow is accompanied by an increase in oxygen supply that exceeds demand, resulting in a change in the relative levels of oxyhemoglobin and deoxyhemoglobin, which can be measured using BOLD-contrast imaging (Bijsterbosch et al., 2017, Lv et al., 2018). The BOLD signal is based on the diamagnetic effect of oxyhemoglobin and the paramagnetic effect of deoxyhemoglobin, whereby voxels with low concentrations of deoxyhemoglobin show an increased BOLD signal, while voxels with high concentrations of deoxyhemoglobin show a decreased BOLD signal (Smitha et al., 2017). The measurement of functional connectivity using rs-fMRI is based on the assumption that regions with similar BOLD signals are functionally connected

over time (Bijsterbosch et al., 2017). That functionally connected regions show correlations of low frequency fluctuations in the BOLD signal in the resting state, was first shown by Biswal et. al (1995). To determine functional connectivity from rs-fMRI data, a seed-based analysis can be conducted. In a seed-based analysis, a region of interest (ROI) is selected, from which the mean BOLD timeseries of the voxels are extracted. Based on the BOLD timeseries of the region of interest, linear correlations with all other voxels of the entire brain are calculated resulting in a seed-based, voxel-wise functional connectivity map (Bijsterbosch et al., 2017, Smitha et al., 2017). This map describes how strongly each individual voxel is functionally connected to the region of interest (Bijsterbosch et al., 2017).

The BOLD signal is generally very noisy (De Blasi et al., 2020, Caballero-Gaudes and Reynolds, 2017) and strongly affected by non-neuronal contributions such as head movements, physiological noise and scanner artefacts (De Blasi et al., 2020). Since functional connectivity analysis in resting state fMRI relies on finding similarities in the BOLD signal between two different brain regions, and many types of noise also induce exactly such similarities, it is essential to perform good preprocessing and noise clean-up in resting state studies (Bijsterbosch et al., 2017, Salimi-Khorshidi et al., 2014). Unlike task fMRI, there is no prior knowledge of the temporal signal of interest in rs-fMRI (Griffanti et al., 2014, De Blasi et al., 2020), so in rs-fMRI any non-neuronal activity occurring across multiple voxels can lead to false results (Griffanti et al., 2014). Hence, the correct identification of non-neuronal fluctuations in the BOLD signal is especially important for rs-fMRI. Independent component analysis (ICA) is a powerful technique to identify different sources of neuronal and artefactual fluctuations in the BOLD signal (Griffanti et al., 2014, Salimi-Khorshidi et al., 2014). ICA can decompose separate origins of neural signal, structured noise and random noise into different components and these components can then be used to clean the resting state fMRI data (Kelly et al., 2010) by removing noise components from the data (Bijsterbosch et al., 2017, Caballero-Gaudes and Reynolds, 2017). The individual ICA components are described by a spatial map and a timecourse (Griffanti et al., 2014, Bijsterbosch et al., 2017). After the independent component analysis has been run and different components have been identified, these components

must be classified as to whether they are noise or signal. This can be done either manually or automatically (Bijsterbosch et al., 2017). Manual classification requires visual inspection and manual labelling of each component (Bijsterbosch et al., 2017), which is time consuming, difficult to reproduce and requires experience (Kelly et al., 2010, De Blasi et al., 2020) and deep knowledge of signal and noise fluctuations' typical spatiotemporal characteristics (Griffanti et al., 2014, Salimi-Khorshidi et al., 2014). To overcome these limitations of manual classification, it is therefore desirable to have an automatic algorithm that can reliably detect different types of noise (Griffanti et al., 2014, Salimi-Khorshidi et al., 2014, Caballero-Gaudes and Reynolds, 2017). Toolboxes such as FIX (FMRIB's ICA-based Xnoiseifier) have been developed that generate a set of more than 180 distinct spatial and temporal features for each component, each describing a different aspect of the data (Salimi-Khorshidi et al., 2014). Based on these features, a multi-level classifier is then used to calculate a score of how likely the component is a signal (Griffanti et al., 2014, Salimi-Khorshidi et al., 2014, Bijsterbosch et al., 2017). However, before FIX can automatically classify components, the classifier must be trained with manually classified data (Griffanti et al., 2014, Salimi-Khorshidi et al., 2014, Bijsterbosch et al., 2017). FIX is very sensitive to acquisition parameters such as repetition time (TR), voxel size, coverage and run length, as well as preprocessing parameters such as smoothing and highpass filtering (Bijsterbosch et al., 2017). If the characteristics of the data deviate strongly from the training sample, the classification accuracy can decrease (Caballero-Gaudes and Reynolds, 2017). Manual denoising, on the other hand, is subjective. Automatic ICA denoising makes the method more objective, but the training sample must of course be very similar to the sample under investigation. Therefore, I investigated the advantages and disadvantages of manual ICA denoising in the preprocessing of resting state fMRI data compared to the standard Human Connectome Project (HCP) minimal preprocessing pipeline that is based on FIX for the GenFI dataset.

In previous studies in FTD patients, it could be shown with rs-fMRI, that in addition to grey matter atrophy, there is also a change in functional connectivity. Whitwell et al. (2011) showed that reduced connectivity was already present in

asymptomatic MAPT carriers, especially in the Default Mode Network (DMN), even before atrophy could be found. This indicates that functional connectivity changes may be one of the first features of the disease (Whitwell et al., 2011). Zhou et al. (2010) showed that altered correlation patterns are present in bvFTD, which they used to differentiate bvFTD from AD. Resting state fMRI could thus serve as a non-invasive method for diagnosing gene carriers and monitoring patients during the course of therapy (Zhou et al., 2010, Whitwell et al., 2011).

The current study was based on the findings of a previous work by Wabersich-Flad (Doctoral thesis, Faculty of Medicine, Eberhard Karls Universität Tübingen, 2021), who found focal cortical degenerations in the left frontal cortex associated with the occurrence of apraxia in genetic FTD, but not regions in the inferior parietal cortex, which are typical for limb apraxia in stroke patients. From these observations, the question arose whether the occurrence of limb apraxia in genetic FTD is caused exclusively by focal degeneration of the inferior frontal cortex. Alternatively, the expression of apraxia symptoms may be at least partly caused by disruption of an inferior frontoparietal network. To date, studies to understand the neural correlates of apraxia have been conducted predominantly in stroke patients and the neural correlates of limb apraxia in FTD are not yet well understood. Additionally, it is generally not yet well researched how the progression of genetic FTD affects the functional and anatomical connectivity of circumscribed systems. The goal was to investigate this with the example of apraxia in patients with genetic FTD. The three delineated regions of cortical degeneration correlating with limb apraxia in patients with genetic FTD (Wabersich-Flad, Doctoral thesis, Faculty of Medicine, Eberhard Karls Universität Tübingen, 2021) were taken as ROIs in three seed-based correlation analyses, to define their functional network. In addition, correlation analyses were calculated based on a seed region that combined all three regions with cortical atrophy as one ROI to test whether it is reasonable to consider the three regions found as functionally independent. My hypothesis was that the three regions are functionally related. The correlation analyses were carried out for FTD patients with apraxia, FTD patients without apraxia and healthy control subjects. Subsequently, between group comparisons were performed with the correlation

maps to investigate whether significant differences in correlations exist between subjects with apraxia and genetic FTD, subjects with genetic FTD but without apraxia and healthy controls. My hypothesis was that there should be reduced correlations in the inferior frontoparietal network in patients with apraxia and genetic FTD compared to healthy controls and patients with genetic FTD without apraxia.

2 Methods

2.1 Study population

The data analyzed in this study are part of the third datafreeze in 2017 of the GenFI consortium. The data acquisition of the GenFI consortium consisted of two phases, GenFI 1 and GenFI 2. The data for GenFI 1 were collected between 2012 and 2015. The second phase with GenFI 2 started in 2015 and is still running today. There are some differences in the collection of data between the two phases, which is why the collection of subjects was restarted for the second phase and data acquisition had to be redone for GenFI 2 even for subjects that were initially included in GenFI 1. For my analyses, I used the data from GenFI 2, whose collection began in March 2015 and ended on the 30th of January 2017 (datafreeze 2017). All participants have been genotyped and underwent a standardized clinical and behavioral assessment. Furthermore, structural and functional MR images were obtained, as well as cerebrospinal fluid and blood biomarkers. For the analyses presented here, not all of this information was relevant. I only used parts of the data from the structural and functional MRI scans, clinical examination, neuropsychological testing and genetic group. All research centers had both informed consent from the local ethics committee and written informed consent from study participants at study enrollment.

For the current study, I divided the study population into three groups, a group of mutation carriers with the symptom apraxia (M+A+), a control group with mutation carriers without apraxia (M+A-) and a further control group with healthy subjects without mutation and without apraxia (M-A-).

2.1.1 Selection of subjects

Since the results of Wabersich-Flad (Doctoral thesis, Faculty of Medicine, Eberhard Karls Universität Tübingen, 2021) have been used for this study, I adopted the same subject sample. The study population of Wabersich-Flad (Doctoral thesis, Faculty of Medicine, Eberhard Karls Universität Tübingen, 2021) included 31 subjects in the group of mutation carriers with apraxia, one age-matched control group with mutation carriers without apraxia with 62 subjects and another age-matched control group with 62 subjects with no mutation and without

apraxia. However, some subjects had to be excluded from this study due to missing rs-fMRI data or problems during preprocessing.

First, only those subjects were selected from whom rs-fMRI data were available with a number of temporal positions of 200, a repetition time (TR) of 2.5s, a slice thickness of 3.5mm, a pixel spacing of [3;3], a flip angle of 80°, and an echo time (TE) of 30ms. At this step, 5 M+A+ subjects, 21 M+A-, and 16 M-A- had to be excluded because either no rs-fMRI data was available at all, or not with the appropriate sequence parameters. To address a significant age difference of 5 years (M+A+ (26 subjects) mean age: 61.47 y SD: 10.94 y; M-A- (46 subjects) mean age: 56.48 y SD: 9.98 y; p=0.053) resulting from the omission of some subjects in the M+A+, I excluded the 6 youngest subjects in the M-A- group. For preprocessing of the data with the HCP minimal preprocessing pipeline, T2w images and Fieldmaps for all subjects are needed. One subject of the control group M-A- had to be excluded because no T2w images were available. Additionally, subjects that had data from a Philips scanner were excluded because there is a difference in preprocessing with the HCP pipeline. Therefore, 6 more M+A- subjects and 7 M-A- were excluded. During preprocessing with the HCP pipeline, errors occurred in some subjects that could not be corrected and therefore led to the exclusion of 4 subjects from group M+A- and 6 subjects from group M-A-. After the correlation analyses were performed for all subjects, I reviewed the correlation maps. It was noticed that parts of the correlation maps were missing for some subjects, probably due to an incorrect registration during preprocessing. These subjects were excluded (4 M+A+, 2 M+A-, 2 M-A-). During manual ICA denoising, an error occurred in one subject of group M+A-, therefore the subject was excluded for further group analyses. This resulted in a subject group of 22 mutation carriers with apraxia (M+A+), one control group of 28 mutation carriers without apraxia (M+A-) and another control group with 25 subjects without an FTD mutation and without apraxia (M-A-). With these subject groups the following statistical analyses were performed.

To determine that age and education differences between groups had no relevant effect on the results of the group analyses, unpaired t-tests were performed,

demonstrating that there were no significant differences in age and education between groups.

2.2 Apraxia scores

As part of the GenFI clinical examination protocol, a screening for upper limb apraxia was conducted by an experienced neurologist. Left and right hand were tested separately. An ordinal scale was used to classify the presence and severity of apraxic symptoms (0: absent, 0.5: very mild/questionable, 1: mild, 2: moderate, 3: severe). In this study, all participants with an apraxic score greater than zero for either hand were selected as part of the apraxia group.

2.3 MR image acquisition

MRI data were collected at all GenFI consortium sites according to the standardized GenFI 2 protocol. T1- and T2-weighted images were acquired, rs-fMRI, FieldMap, DTI and Arterial Spin Labelling (ASL). All images were acquired on 3 Tesla scanners. For the upcoming analyses the anatomical T1-weighted and T2-weighted images, rs-fMRI and FieldMaps were used. The T1-weighted images were acquired with an isotropic resolution of 1.1mm, TR=2000ms, TE=2.85ms, TI=850ms, FoV=282mm, 208 sagittal slices, flip angle of 8°, acquisition time of 8 minutes and 32 seconds, phase encoding direction from anterior to posterior and base resolution of 256. The T2-weighted images were acquired with an isotropic resolution of 1.1mm, TR=3200ms, TE=401ms, FoV=282, 176 sagittal slices, acquisition time of 4 minutes and 46 seconds, phase encoding direction from anterior to posterior and base resolution of 256. The resting state functional MR images were acquired with a resolution of 3*3*3.5mm, TR=2500ms, TE=30ms, FoV=192, 42 slices with an orientation transversal>sagittal-2.9, flip angle of 80°, number of temporal positions 200, acquisition time of 8 minutes and 29 seconds, phase encoding direction from anterior to posterior and base resolution 64. The FieldMaps were acquired with an isotropic resolution of 3mm, TR=688ms, TE 1=4.92ms, FoV=192mm, 55 slices with an orientation transveral>sagittal-2.9, flip angle of 60°, acquisition time of 1 minute and 31 seconds, phase encoding direction from anterior to posterior and base resolution 64.

2.4 Preprocessing of imaging data

Preprocessing of all scans was performed using the HCP minimal preprocessing pipeline ((Glasser et al., 2013); v.4.0.1; https://www.humanconnectome.org/software/hcp-mr-pipelines).

The raw data produced by the GenFI consortium were available in Digital Imaging and Communications in Medicine (DICOM) format. To process the data, they were first converted into the Neuroimaging Informatics Technology Initiative (NIfTI) format. I converted the T1w, T2w images and FieldMaps with the Statistical Parametric Mapping software (SPM12, version 6225, https://www.fil.ion.ucl.ac.uk). The magnitude FieldMap images are available in DICOM format as 2 separate files. For further preprocessing with the HCP minimal preprocessing pipeline, one 4D file must be available. Therefore, after converting the two magnitude FieldMap files to NIfTI format, I converted them with the 3D to 4D conversion of SPM12. The rs-fMRI images were converted with the command line dcm2niix, because in contrast to the conversion with SPM12 the header information is retained here, which is necessary for the later preprocessing with the HCP pipeline.

2.4.1 HCP minimal preprocessing pipeline

The HCP minimal preprocessing pipeline is built on MATLAB (version R2017b used, The MathWorks, Inc. Natick, MA, USA), FSL (v6.0, https://fsl.fmrib.ox.ac.uk/fsl/fslwiki/), FreeSurfer (v6, https://surfer.nmr.mgh.harvard.edu/) and the HCP Connectome Workbench (v1.4.1, https://www.humanconnectome.org/). I worked with a Linux operating system. For a detailed description of the individual preprocessing steps of the HCP minimal preprocessing pipeline, please see Glasser et al. (2013). I adjusted environment variables but made no changes to the scripts that affect the processing of the data.

2.4.1.1 PreFreeSurfer

The HCP minimal preprocessing pipeline usually starts with a gradient distortion correction, because in the custom HCP Skyra scanner the head is above the isocenter and therefore gradient nonlinearities are increased compared to

standard 3T scanners (Glasser et al., 2013). Since our data were not measured with HCP scanners, the gradient distortion correction was not performed during preprocessing. First, the T1w and T2w images have been cropped to a smaller field of view, with the neck removed, using FSL's automated robustfov tool. Furthermore, the images have been registered with an affine FLIRT transformation (12 degrees of freedom (DOF)) to the MNI152 space templates. Subsequently, the T1w and T2w images have been aligned to the MNI space template using a rigid 6 DOF transformation. Images have been aligned using the anterior commissure (AC), the line between the anterior and posterior commissure (AC-PC line) and the interhemispheric plane. This put the images in approximately the same orientation as the template. Next, an initial brain mask was created to enable the later final registration with the MNI space. For this purpose, an initial brain extraction has been performed in which the image has been registered to the MNI template with a linear (FLIRT) and non-linear (FNIRT) registration. The template brain mask has then been inverted again and brought back into the acpc-alignment space. A readout-distortion-correction of the T1w images, as normally done by the HCP minimal preprocessing pipeline, was not performed. The T2w images have been registered with FLIRT BBR to the T1w images. A bias field correction has been performed, where the bias field was estimated by the square root of the product of T1w and T2w after thresholding out non-brain tissue. Finally, the T1w images have been registered to MNI space with a FLIRT 12 DOF affine and a FNIRT nonlinear registration.

2.4.1.2 FreeSurfer

The coregistration of the data across modalities and with the template space was followed by further preprocessing with FreeSurfer's recon-all pipeline. The HCP minimal preprocessing pipeline runs FreeSurfer's recon-all pipeline with interruptions at certain steps to improve the robustness of the brain extraction, as well as the registration from T2w to T1w (Glasser et al., 2013). An automated segmentation of the T1w volume into cortex, white matter and subcortical structures has been performed (Fischl et al., 2002). Then, the surface tessellation and topology correction of the initial white matter surface has been carried out. The registration from T2w to T1w was optimized by FreeSurfer's BBRegister

algorithm. The next steps of recon-all included spherical inflation of the white matter surface, registration to the fsaverage surface template based on cortical folding patterns and automated segmentation of the sulci and gyri. The HCP minimal preprocessing pipeline used an improved algorithm to generate the pial surfaces, again interrupting recon-all. Subsequently, the final steps of recon-all have been completed, in which surface and volume anatomical parcellation was performed and morphometric measurements of structure volumes and surface areas have been made.

2.4.1.3 PostFreeSurfer

In the final step of preprocessing the structural data, the HCP minimal preprocessing pipeline first converted the outputs of recon-all into standard NIfTI and GIFTI formats. It also created the final brain mask and myelin maps.

2.4.1.4 fMRIVolume

Next, the functional data has been preprocessed. First, the fMRI volume pipeline has been run. The default setting included a correction for gradient-nonlinearity-induced distortion, which I did not carry out, as already explained in the paragraph about the PreFreesurfer pipeline (please see above). There was a realignment of the timeseries to correct for subject motion. Normally, this is done using a 6 DOF FLIRT registration of each frame to a single-band reference image. However, I did not have a single-band reference image, so I used the alternative setting of the HCP minimal preprocessing pipeline, where the registration was done to the first volume of the timeseries. A correction of the distortion in the phase encoding direction was carried out with the help of gradient-echo field maps. The undistorted rs-fMRI images have been registered to the T1w images, using 6 DOF FLIRT with the BBR cost function and FreeSurfer's BBRegister for fine-tuning. Registration from native volume to MNI nonlinear was performed. All transformations have been concatenated and applied to the rs-fMRI timeseries in a single spline interpolation. By default, a bias field correction would be performed, but I did not apply this. Finally, the data was masked by the final brain mask from PostFreeSurfer and the intensity has been normalized to the 4D global mean.

2.4.1.5 fMRISurface

With the fMRISurface pipeline, the volume timeseries of the rs-fMRI data are mapped to the standard CIFTI greyordinates space. For this purpose, a partial volume-weighted ribbon-constrained volume to surface mapping algorithm is first used to determine which rs-fMRI voxels are located in the grey matter ribbon. This is done using the white and pial surfaces. Voxels with a high coefficient of variation in the timeseries (more than 0.5 standard deviation above the mean coefficient of variation of the other voxels in a 5 mm sigma Gaussian neighborhood) are excluded from the volume to surface mapping. The aim is to remove voxels that are close to the edge of the brain parenchyma or contain large blood vessels. Subsequently, the surface timeseries are resampled from a high-resolution native mesh to the registered downsampled 32k_fs_LR mesh. In addition, a slight smoothing of the data with a 3mm Full Width at Half Maximum (FWHM) is performed. The smoothing is performed using a geodesic Gaussian surface smoothing algorithm. The standard CIFTI greyordinates space is formed by sampling the individual timeseries of the subjects onto a standard set of left and right hemisphere surface vertices and a standard set of subcortical grey matter voxels. The final output of the pipeline is a CIFTI dense timeseries file containing the surface timeseries of both hemispheres and the subcortical volume timeseries of all subcortical structures.

2.4.1.6 rs-fMRI Denoising

Further preprocessing of the rs-fMRI data is done with the ICAFIX pipeline. This involves temporal preprocessing and artefact removal. No slice-time correction is performed. Minimal highpass filtering is carried out using the -bptf option in FSL's fIsmaths tool with a cutoff of 2000s. No lowpass filtering is performed. Subsequently, ICA-based artefact removal is applied using FIX (FMRIB's ICA-based Xnoiseifier, v1.06, (Griffanti et al., 2014, Salimi-Khorshidi et al., 2014)). First, an automatic dimensionality estimation is performed using MELODIC (Multivariate Exploratory Linear Optimized Decomposition into Independent Components). The components identified by MELODIC are then fed into FIX and classified into good and bad components by the multivariate classifier. These steps are done with the volumetric data. I defined the Standard.RData training

data file for the classifier, which has the following properties: TR=3s, Resolution=3.5x3.5x3.5mm³, Session=6mins, default FEAT preprocessing (including default spatial smoothing) (https://fsl.fmrib.ox.ac.uk/fsl/fslwiki/FIX/UserGuide#Training_datasets). Preferably, the classifier should be trained with data from the respective, specific sample and study, as FIX is very sensitive to acquisition parameters such as TR, voxel size, coverage and run length, as well as preprocessing parameters such as smoothing and highpass filtering (Bijsterbosch et al., 2017). Here, the acquisition parameters of the standard training dataset used or the classifier do not match well with the parameters of my dataset. The components classified as artefacts by the classifier are removed non-aggressively from the volumetric and greyordinates data. In addition, as part of the cleanup, the motion parameters are aggressively regressed out of the data. I then used the outputs from the ICAFIX pipeline for the first correlation analyses.

2.4.2 Manual ICA Denoising of resting state data

In addition to the automatic ICA denoising by the HCP pipeline described above, I performed a manual ICA denoising of the data, because the available training data file did not correspond well to the acquisition parameters of my data and when looking at the individual correlation maps later on, I noticed that for some subjects no meaningful results were obtained by the automated ICA denoising.

For the manual classification of the ICA components, I used the outputs of MELODIC, which were previously created by the HCP minimal preprocessing pipeline. For the visualization I used FSLeyes. The goal of denoising is to reduce noise while preserving as much signal as possible (Griffanti et al., 2017, Kelly et al., 2010). Therefore, in case of doubt, if I was unsure whether the component contained signal or not, I classified it as signal and retained it in the data. I classified components as noise that showed activations in the spatial map that were irregularly distributed throughout the brain and did not show a region with a clear clustering of signals (Griffanti et al., 2017, Kelly et al., 2010, Rummel et al., 2013). In contrast, signal components were characterized by the presence of a small number of relatively large clusters of consistent correlations in the spatial map (Griffanti et al., 2017). I also classified components which were localized in

white matter, cerebrospinal fluid or blood vessels as noise. Components that were confined to the borders of the brain and had a ring-like structure, which is typical for motion artefacts (Griffanti et al., 2017, Rummel et al., 2013), were also classified as noise. Non-physiological patterns such as stripes or clusters that only occurred in alternating slices were also classified as noise. Other indications that a component was a noise component were sudden jumps in the time course, which are indicative of a motion artefact (Griffanti et al., 2017, Kelly et al., 2010), and a power spectrum dominated by high frequencies, as BOLD signal components are characterized by low frequency fluctuations (Griffanti et al., 2017, Kelly et al., 2010). I cleaned the data with the function fix_3_clean. The components that I had previously classified as noise were aggressively regressed out of the CIFTI dense timeseries with highpass filtering with a cutoff at 2000s. Motion-related timecourses were not regressed out of the data.

2.5 Correlation analyses

The previous work of Wabersich-Flad (Doctoral thesis, Faculty of Medicine, Eberhard Karls Universität Tübingen, 2021) has identified, among others, 3 regions that showed a significant focal reduction of cortical thickness in the between group comparison M+A+ vs. M+A-. Based on these 3 regions, which appear to play an important role in apraxia in genetic FTLD (Wabersich-Flad, Doctoral thesis, Faculty of Medicine, Eberhard Karls Universität Tübingen, 2021), I performed correlation analyses to identify the functional network of apraxia. Based on the functional network of apraxia, I then investigated whether, in addition to cortical degenerations in the inferior frontal cortex, changes in connectivity in the inferior frontoparietal network also play a role in the development of apraxia symptoms in patients with genetic FTD.

In order to use Wabersich-Flad's 3 regions (Doctoral thesis, Faculty of Medicine, Eberhard Karls Universität Tübingen, 2021) as regions of interest for my correlation analyses, I mapped them from the FreeSurfer fsaverage mesh to the HCP standard fs_LR_mesh. I first used the mris_convert command, followed by the wb_command -label-resample and -gifti-label-to-roi. I ran these steps for

ROI1, ROI2 and ROI3, so that in the end I had a metric file in GIFTI format for all 3 ROIs with which I could perform the following correlation analyses.

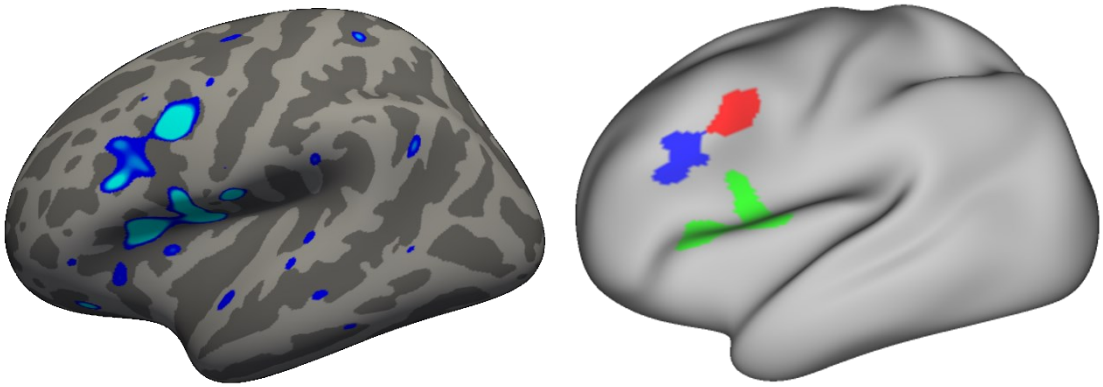

Figure 1: *On the left areas that have a significant focal reduction in cortical thickness when comparing M+A+ vs. M+A- for p<0.01 and in dark blue for p<0.05 are shown in light blue, mapped on the left hemisphere surface of the fsaverage subject (Wabersich-Flad, Doctoral thesis, Faculty of Medicine, Eberhard Karls Universität Tübingen, 2021). On the right are the three ROIs that were converted to the HCP mesh and used for the following correlation analyses. In red ROI1, in green ROI2 and in blue ROI3.*

I conducted the first correlation analyses with the outputs of the HCP pipeline, hence with the rs-fMRI data that went through the automated ICA denoising with FIX. In preparation for the first correlation analyses, I first used the wb_command -cifti-create-dense-from-template to create a file for each subject for ROI1, ROI2 and ROI3, which contain the time series in the region of interest. I then used the wb_command -cifti-average-roi-correlation to perform the correlation analyses. The command first averages the timecourse of all the voxels of the ROI and then calculates the correlation with all other voxels. Finally, the command performs a Fisher z-transformation. Thus, I obtained a correlation map for ROI1, ROI2 and ROI3 for each subject. I also performed correlation analyses with the automatically ICA denoised data and 6 mm smoothing. For this purpose, I first smoothed the data with the command wb_command -cifti-smoothing with a smoothing kernel of 6 mm as sigma. Then, I went through the steps mentioned above again for the smoothed data and obtained correlation maps for all 3 ROIs for each subject, based on the automatically ICA denoised data with 6 mm smoothing.

Since in these first correlation maps I noticed that no meaningful correlations with the region of interest occurred for some subjects, I conducted further correlation

analyses with differently preprocessed data to investigate the effect of denoising on the correlation analyses. I performed the second correlation analyses with the outputs of the HCP pipeline that underwent highpass filtering but not ICA denoising. I first smoothed this data using the wb_command -cifti-smoothing with a smoothing kernel of 6mm as sigma. Then, I again ran the wb_command -cifti-create-dense-from-template and wb_command -cifti-average-roi-correlation for each subject for all three ROIs.

Finally, I performed further correlation analyses with the outputs that were created after the manual ICA denoising. First, I smoothed the data with the wb_command -cifti-smoothing, once with a smoothing kernel of 6mm and once with a smoothing kernel of 9mm as sigma. Subsequently, I performed the correlation analyses for all subjects for ROI1, ROI2 and ROI3 once with 6mm smoothing and once with 9mm smoothing using the commands wb_command -cifti-create-dense-from-template and wb_command -cifti-average-roi-correlation.

In addition to the correlation analyses performed with the 3 separate seed regions, I also performed correlation analyses with the seed region ROIall, where all 3 seed regions were combined into one. I created ROIall by merging the label files of ROI1, ROI2 and ROI3 with mri_mergelabels. I then mapped ROIall from the FreeSurfer fsaverage mesh to the HCP standard fs_LR_mesh using mris_convert, wb_command -label-resample and wb_command -gifit-label-to-roi. Based on the previously created rs-fMRI data with manual ICA denoising and 9mm smoothing, I then performed the correlation analyses with ROIall for all subjects with wb_command -cifti-create-dense-from-template and -cifti-average-roi-correlation.

To compare the correlation maps between the three groups of subjects, I created an average correlation map for each of the three groups based on the individual correlation maps. For this purpose, I used the individual correlation maps that were created on the basis of the manually ICA denoised data with 9mm smoothing. Using the wb_command -cifti-average, I created an average correlation map for ROI1, ROI2, ROI3 and ROIall for the groups M+A+, M+A- and M-A-.

2.6 Comparison of the different ICA denoising methods

To show the differences in the correlation maps caused by the different denoising methods for the entire study population in each vertex, I created subtraction images of the correlation maps with the different ICA denoising methods. I used the wb_command -cifti-math to subtract for each subject the output of the correlation analysis with the data with no ICA denoising and 6mm smoothing minus the output of the correlation analysis with the data with HCP ICA denoising and 6mm smoothing. I also created subtraction images of the correlation maps for each subject for HCP ICA denoising with 6mm smoothing minus manual ICA denoising with 6mm smoothing and no ICA denoising with 6mm smoothing minus manual ICA denoising with 6mm smoothing. I performed this for all subjects for the correlation analyses with ROI1, ROI2 and ROI3. To show the differences between the denoising methods for the entire study population, I created an average subtraction image from the individual subtraction images of all subjects with the wb_command -cifti-average for the respective subtraction.

In order to statistically quantify the changes in the correlation maps due to the different ICA denoising methods, paired voxelwise t-tests were carried out with the individual correlation maps of all subjects. For this purpose, I used the tool Permutation Analysis of Linear Models (PALM, version alpha116, https://fsl.fmrib.ox.ac.uk/ fsl/fslwiki/PALM). I performed a paired t-test that tested whether there was a significant difference between the correlation maps based on the data with no ICA denoising and 6mm smoothing and the data with manual ICA denoising and 6mm smoothing. I also performed a paired t-test testing the correlation maps of no ICA denoising with 6mm against those with HCP ICA denoising and 6mm, and another testing HCP ICA denoising with 6mm smoothing against manual ICA denoising with 6mm smoothing. In all cases, the analyses were carried out with 5000 permutations. PALM performs a family wise error rate correction (FWER) for multiple testing, which is permutation based (Winkler et al., 2014).

2.7 Between group comparison of network maps

I then performed between group comparisons based on the individual correlation maps created from the data with manual ICA denoising and 9mm smoothing. I used PALM to perform 2-sample voxelwise t-tests for M+A+ vs. M-A-, M+A+ vs. M-A- and M+A- vs. M-A- to see if there were significant differences in the correlations with the respective seed region between the groups. I conducted the 2-sample voxelwise t-tests for ROI1, ROI2, ROI3 and ROIall. In all cases, the analyses were carried out with 5000 permutations.

In addition to the t-tests, I also created effect size maps for the respective between group comparisons to also get an indication of how big the difference is between the correlations of the respective groups. For this purpose, I calculated the Cohen's d according to the following equation using the wb_command -cifti-math based on the t-value maps produced by the PALM 2-sample voxelwise t-tests:

$$d = t\sqrt{\frac{n_1 + n_2}{n_1 * n_2}}$$

3 Results

Resting state correlations with the 3 seed regions that showed significant atrophy of the frontal cortex in relation to the symptom apraxia were identified. In the between group comparisons, it was examined whether there was a significant difference in these correlations between the groups M+A+ and M-A-, as well as M+A+ and M+A- and M+A- vs. M-A-, and thus whether it could be assumed that the symptom of apraxia in FTD patients is not only caused by cortical degeneration in the frontal cortex, but is also based on the fact that the connectivity with the inferior frontoparietal network is altered.

3.1 Study population

The study population for the correlation analyses and between group comparisons consisted of three groups: M+A+ with 22 subjects, M+A- with 28 subjects and M-A- with 25 subjects. An overview of the demographic data of these groups is shown in Table 1.

	M+A+	M+A-	M-A-
N (male/female)	22 (12/10)	28 (13/15)	25 (11/14)
Age	62.08 (9.76)	58.57 (12.08)	59.39 (6.8)
Education	11.95 (3.81)	13.57 (3.99)	13.4 (3.66)

Table 1: *Descriptive statistics of the groups. Age and education are given as means with standard deviation in brackets.*

Unpaired t-tests were performed to determine that age and education differences between groups were non-significant and had no relevant effect on the results of the between group comparisons. The unpaired t-test for the groups M+A+ and M+A- resulted in a non-significant p-value of 0.2736 for age and 0.1526 for education. Also, the unpaired t-tests for the groups M+A+ and M-A- resulted in non-significant p-values of 0.2742 for age and 0.1904 for education. For the groups M+A- vs. M-A- non-significant p-values of 0.7658 for age and 0.8728 for education were obtained.

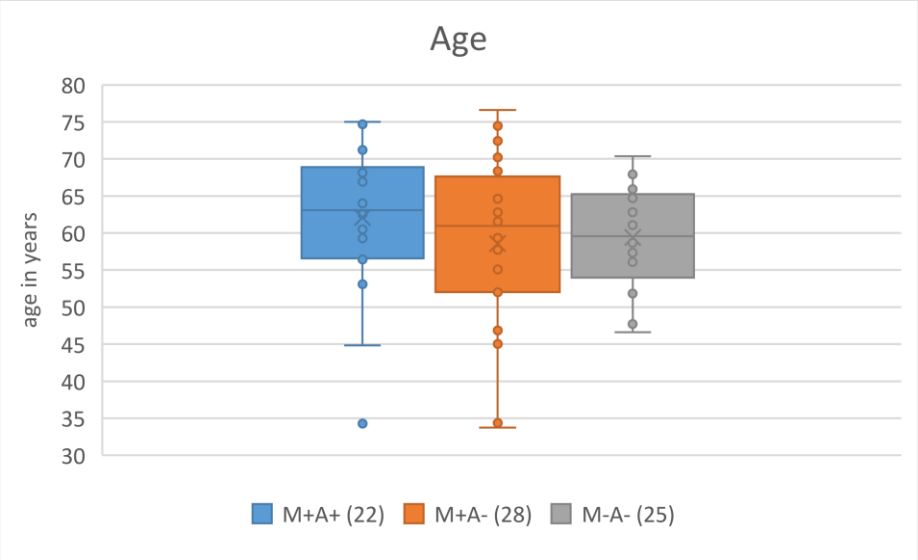

Figure 2: *Box plots showing the dispersion of age of the groups. The middle line of each box shows the median, upper and lower lines indicate the 25th and 75th percentile, respectively. Whiskers show the 5th and 95th percentile. The cross marks the mean. Dots show each individual's datapoint.*

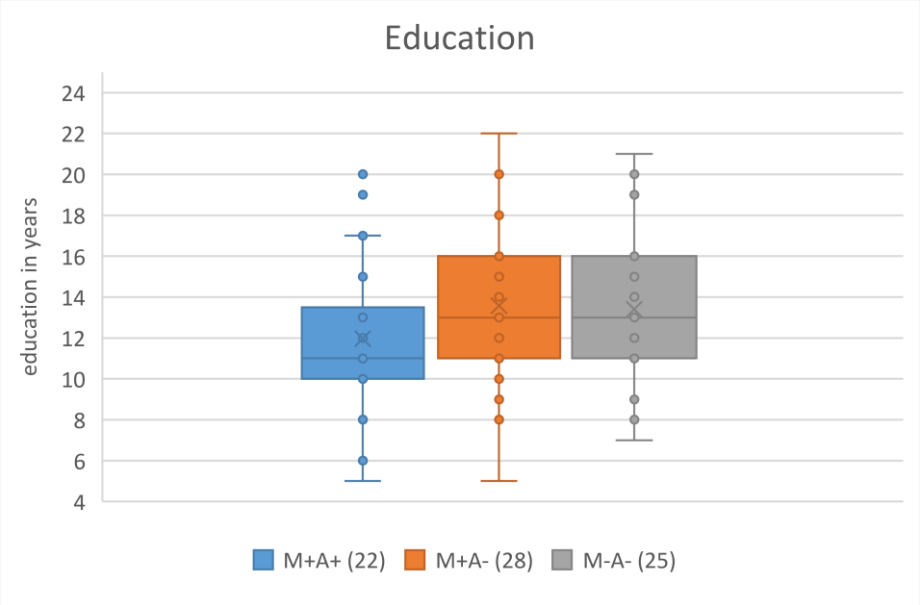

Figure 3: *Box plots showing the dispersion of years of education of the groups. The middle line of each box shows the median, upper and lower lines indicate the 25th and 75th percentile, respectively. Whiskers show the 5th and 95th percentile. The cross marks the mean. Dots show each individual's datapoint.*

3.2 Impact of manual ICA denoising

I decided to do a hand classification of fMRI noise components, as I noticed that some errors occurred during the automated ICA denoising by the HCP pipeline. The cause was probably that our MRI data is of lower quality than recommended by the HCP Minimal Preprocessing Pipeline. The training sample used in ICA denoising by the HCP Minimal Preprocessing Pipeline does not have the same acquisition parameters as our data, which explains the discrepancies in classification. In manually classifying the individual independent components, I followed the recommendations of the current literature on the procedure, which was described in the methods section above.

3.2.1 Approach for manual classification

In the following, individual independent components are presented as examples of how they were manually classified. Figure 4 shows an example of a component that had been classified as a signal. It can be seen in the spatial map that there was predominantly a small number of relatively large clusters. This and the fact that the clusters were located within the grey matter indicated that it was a signal component. The distribution of the large clusters within the medial prefrontal cortex, precuneus, and angular gyrus is typical for the default mode network. In addition, the time series and power spectrum also suggested a signal component, as the time series did not show sudden jumps and the power spectrum was predominantly in the low frequencies.

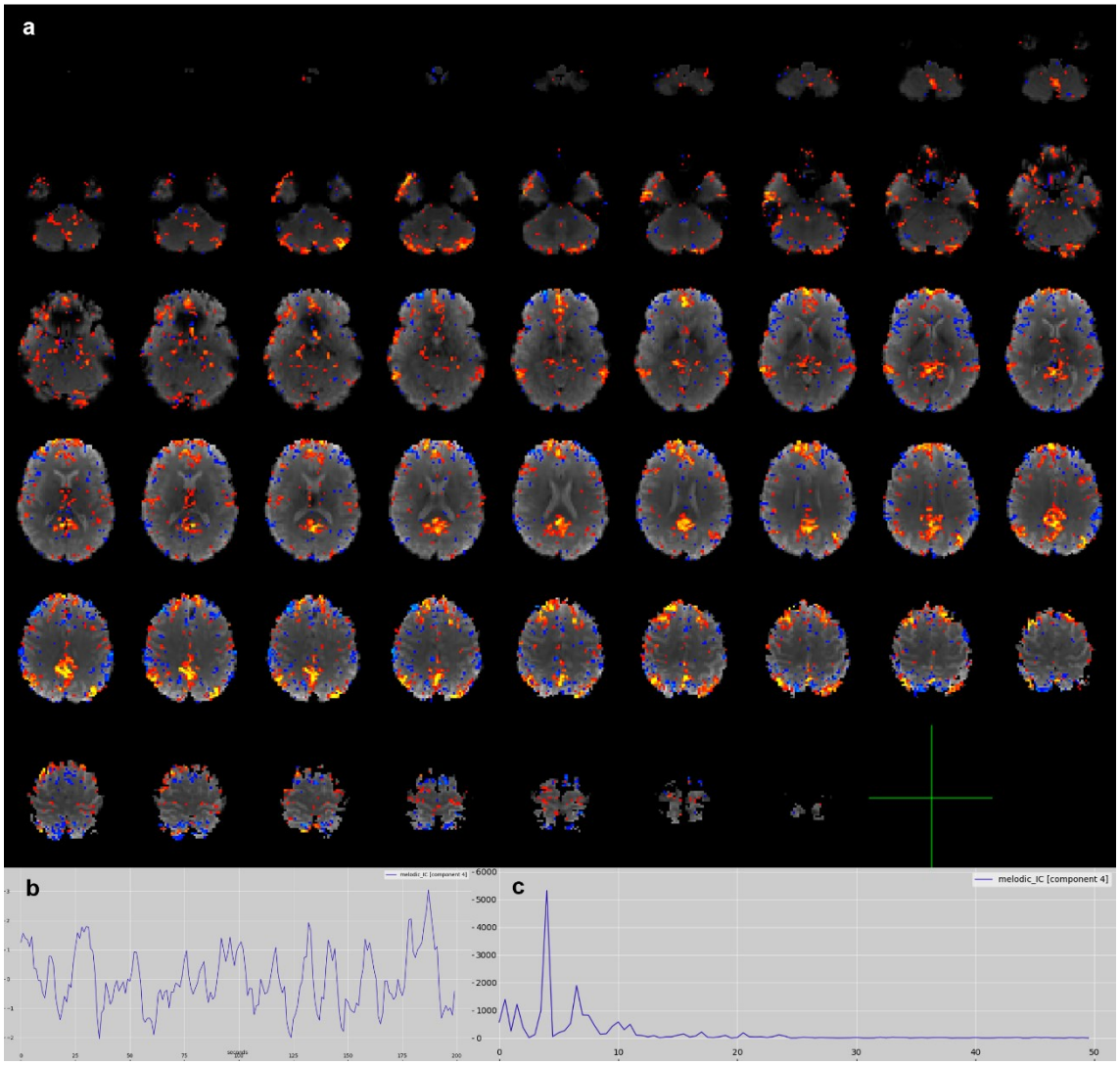

Figure 4: *Signal. a: An example signal component presumably showing the Default Mode Network. Spatial map of thresholded z-scores with z>2. b: Time series of the component. c: Power spectrum of the component.*

The component shown in Figure 5 was classified as a noise component during manual ICA denoising. The spatial map showed predominantly many small clusters, without any clustering. These were mainly located in a ring-like shape at the edge of the brain, which is typical for motion artefacts. There are also small clusters in the lateral ventricles, therefore not located within grey matter, which also indicates that it is a noise component. In the time course (Figure 5b) one sees several sudden jumps, which indicates fast head movements. Therefore, I classified this component as noise. The HCP pipeline, on the other hand, classified this component as unknown and thus it was left in the data set that was used in the first correlation analyses.

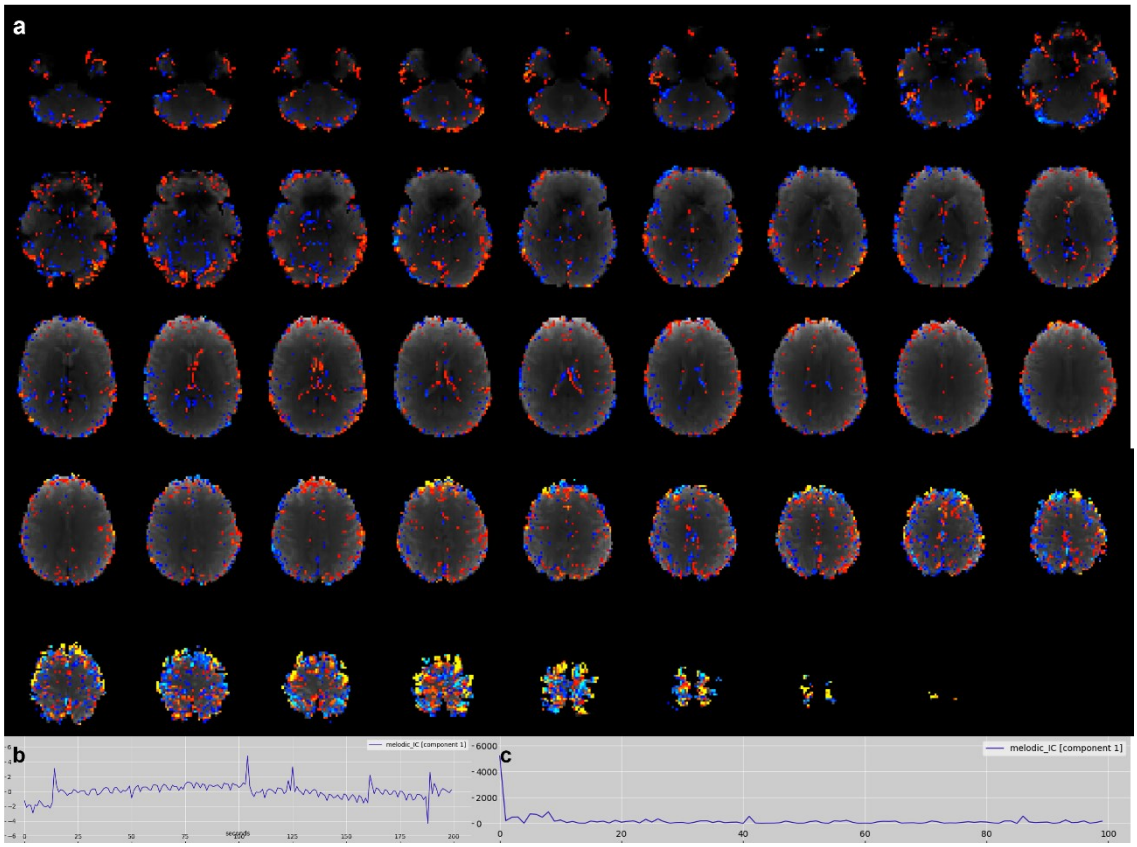

Figure 5: *Motion artefact. a: The spatial map shows a typical ring of small clusters at the edge of the brain. Thresholded z-scores with z>2. b: Time course of the component. c: Power spectrum of the component.*

The component in Figure 6 was classified as a noise component. In the spatial map, there were many rather small clusters in the area of the middle cerebral artery. The middle cerebral artery runs through the insula and can therefore be confused with a grey matter signal from the insula. Therefore, in this case, it was particularly important to also look at the power spectrum. Further clusters could be found in the area of the posterior cerebral artery and the anterior cerebral artery. Anterior to the pons, clusters were seen corresponding to the basilar artery. In addition, the component showed a typical high frequency spectrum in the power spectrum, which was also indicative of an arterial noise component.

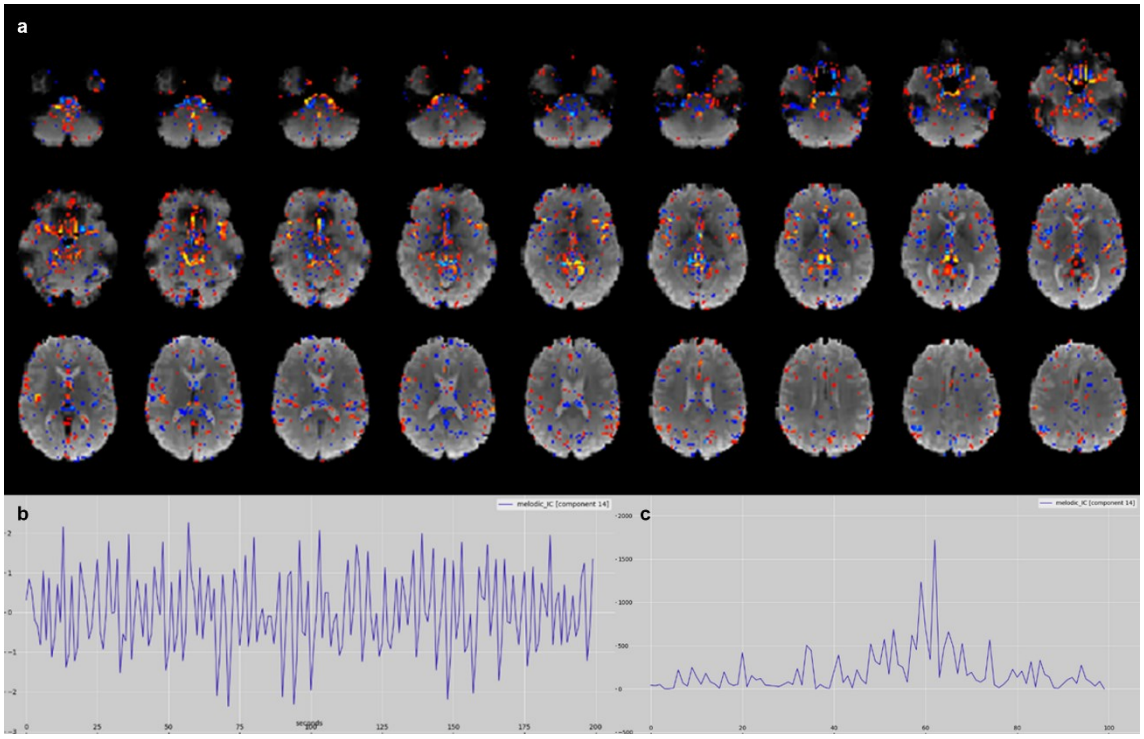

Figure 6: *Noise component, arteries. a: Spatial map with thresholded z-scores with z>2. b: Time course of the component. c: Distinctive power spectrum with predominantly high frequencies.*

Figure 7 shows a component that was classified as a noise component during manual ICA denoising. In the spatial map, there were predominantly small clusters that were irregularly distributed across the brain. Some clusters were located in the lateral ventricles and thus were not grey matter signal. In the power spectrum, in addition to a peak in the low frequencies, there were peaks in the high frequencies, which also suggested the presence of a noise component. Therefore, in contrast to the automated ICA denoising by the HCP pipeline, this component was classified as noise and removed from the data set before the second correlation analyses.

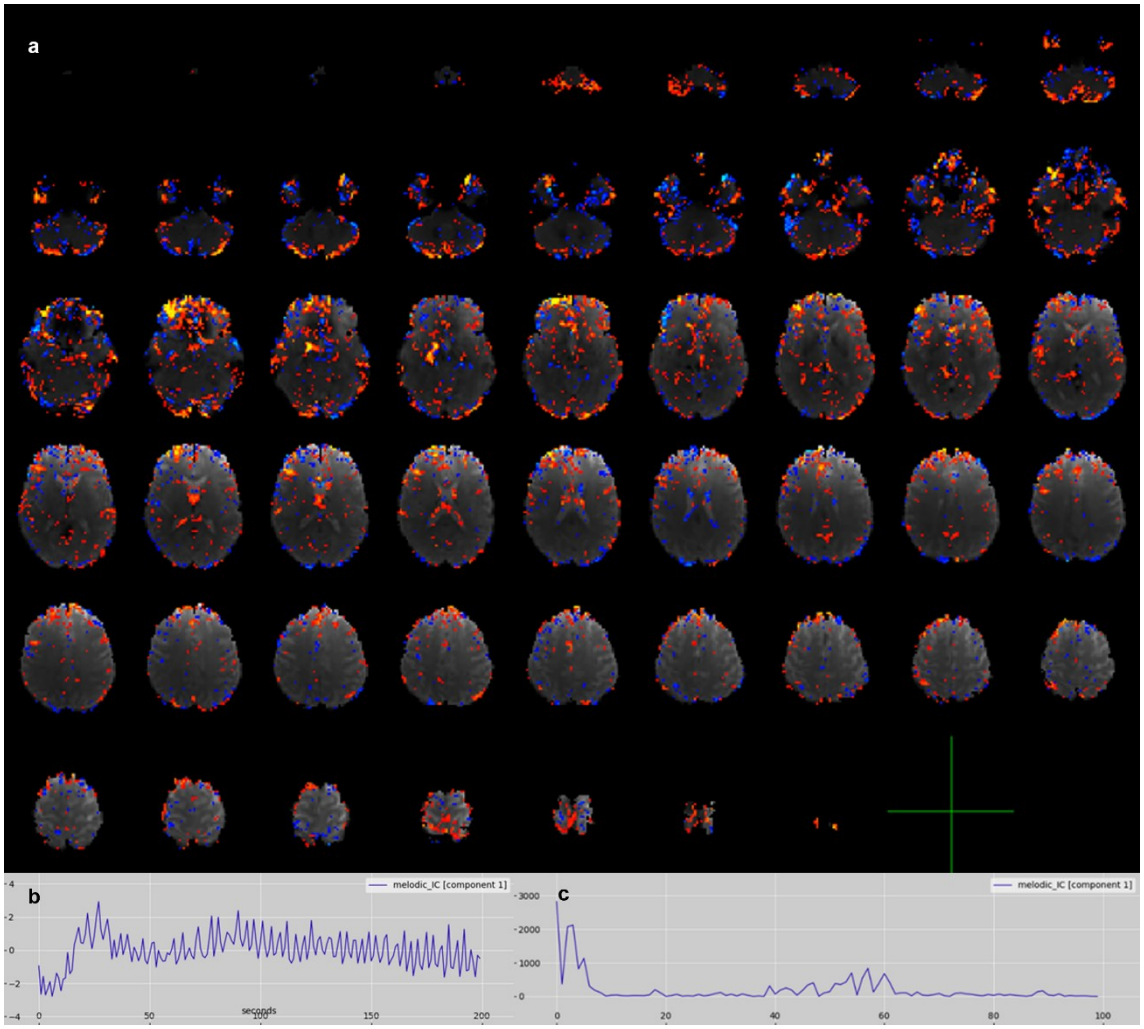

Figure 7: *Noise component. a: Small clusters irregularly distributed across the brain. Spatial map of thresholded z-scores with z>2. b: Time course of the component. c: Power spectrum of the component.*

Figure 8 shows a component that was classified as noise. The large clusters in the spatial map were found primarily in the lateral ventricles and were therefore not grey matter signal. Other smaller clusters were found, mostly at the edge of the brain and could be related to head motion. In addition, a sudden jump was found in the time course, which was indicative of sudden head movement. Therefore, when manually classifying this component, no evidence could be found that this was a signal and the component was therefore removed from the dataset as unclassified noise. In contrast, this component was classified as unknown by the HCP pipeline during ICA denoising and remained in the data with which the first correlation analyses were performed.

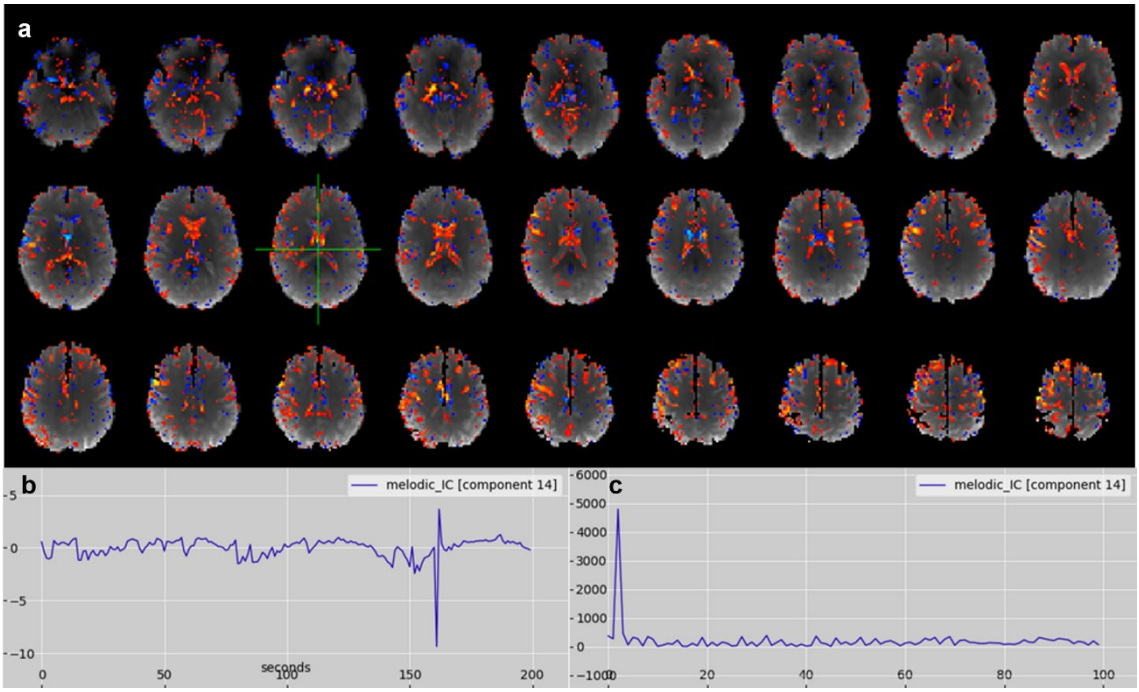

Figure 8: *Noise component. a: Clusters in the lateral ventricles. Spatial map of thresholded z-scores with z>2. b: Time course of the component showed a sudden jump. c: Power spectrum of the component.*

3.2.2 Effects of individual mismatch with predefined ICA components

I calculated correlation analyses for each of the 3 ROIs for each subject, using the data preprocessed by the HCP pipeline after the automated ICA denoising. Thus, I obtained a correlation map for ROI1, ROI2, and ROI3 for each subject. Checking the individual correlation maps it became apparent that for some subjects the correlation maps did not look as expected. For example, some subjects' correlation maps showed almost no high correlation around the seed region and otherwise, there were many small clusters with high correlations everywhere (see Figure 9). In contrast, some subjects' correlation maps showed high correlation around the seed region, as expected, and some clusters with high correlations in the inferior occipitotemporal region and along the intraparietal sulcus (see Figure 10). These regions all corresponded to the typical regions found in task-based action control experiments and were thus in line with expectations.

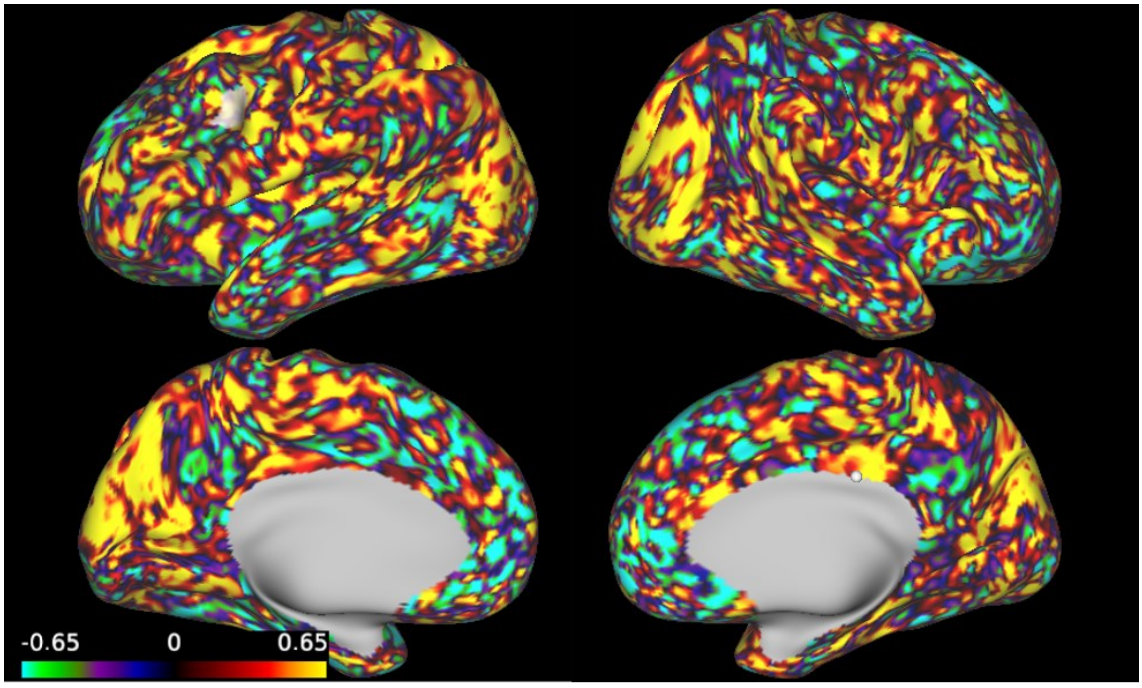

Figure 9: *Correlations with ROI1 (white) of subject C9ORF111 after automated ICA denoising by the HCP pipeline. Yellow corresponds to a high correlation coefficient, dark red to a low one. Almost no correlations around the seed region. Many high correlations everywhere.*

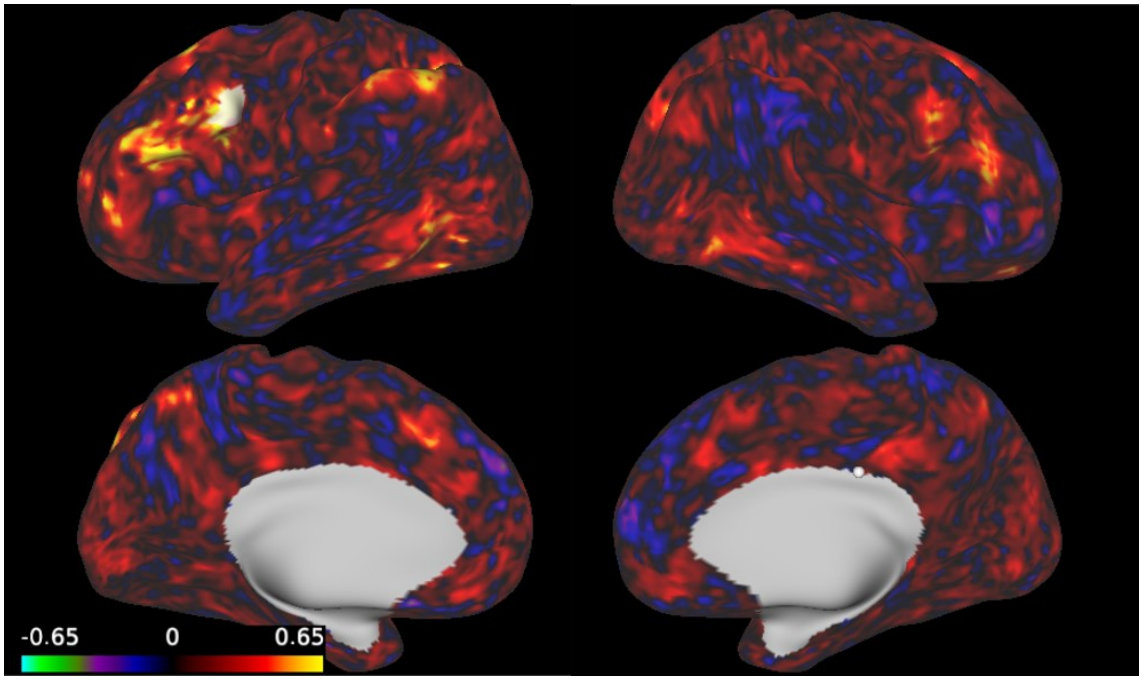

Figure 10: *Correlations with ROI1 (white) of subject C9ORF037 after automated ICA denoising by the HCP pipeline. Yellow corresponds to a high correlation coefficient, dark red to a low one. High correlations around the seed region. High correlations in the inferior occipitotemporal region, and along the intraparietal sulcus.*

Therefore, correlation analyses were then performed with all 3 ROIs for each subject using the preprocessed data after highpass filtering but without ICA denoising and with 6mm smoothing. Since the assumption was that during the automated ICA denoising by the HCP pipeline, errors had occurred in some subjects, leaving mostly noise in the cleaned data. Hence, we wanted to perform a correlation analysis with the data without ICA denoising. It could now be seen that even in the previously problematic subjects the highest correlations were in and around the seed region, as exemplified in Figure 11. There were now very large areas with high correlations especially in the frontal lobe around ROI1 and in the intraparietal sulcus on the left hemisphere.

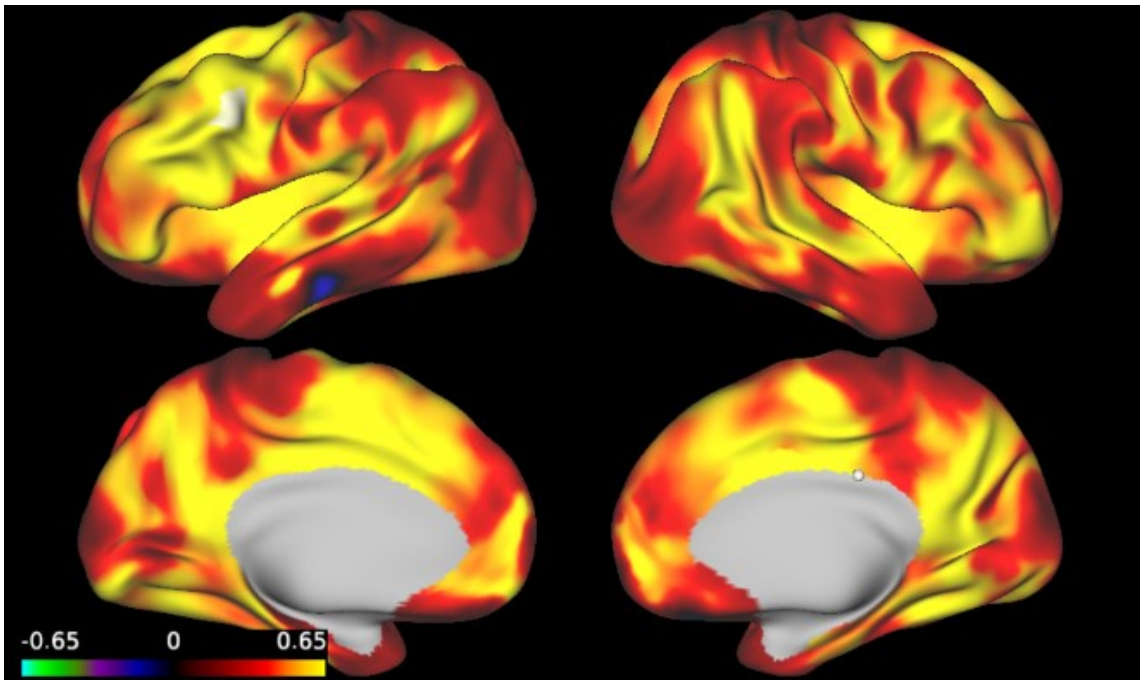

Figure 11: *Correlations with ROI1 (white) of subject C9ORF111 after highpass filtering, with 6 mm smoothing but without ICA denoising. Large clusters with high correlations around the seed region.*

With the manually ICA cleaned data with 6 mm smoothing, a correlation analysis was then performed again for all 3 ROIs for each subject. Here, one could see, exemplified by the subjects already shown above, that there were still large clusters with high correlations in and around the seed region (see Figure 12 and Figure 13). Otherwise, fewer high correlations were now present compared to the correlation analysis without ICA denoising. Comparing Figure 10 and Figure 13 with each other, it was noticeable that due to the manual ICA denoising and

smoothing of 6 mm, the areas of high correlations became larger, but were still located in the expected areas around the seed region, occipitotemporal and the intraparietal sulcus and could now be more sharply delineated. When comparing Figure 9 and Figure 12, a difference between the two correlation maps was noticeable, even though they were from the same subject. In Figure 12 there were now clearly large clusters with high correlations in the expected areas, whereas in Figure 9 these were not yet definable at all. Figure 12 in distinction to Figure 11 shows somewhat smaller clusters with high correlations, which were now more focused on the expected areas.

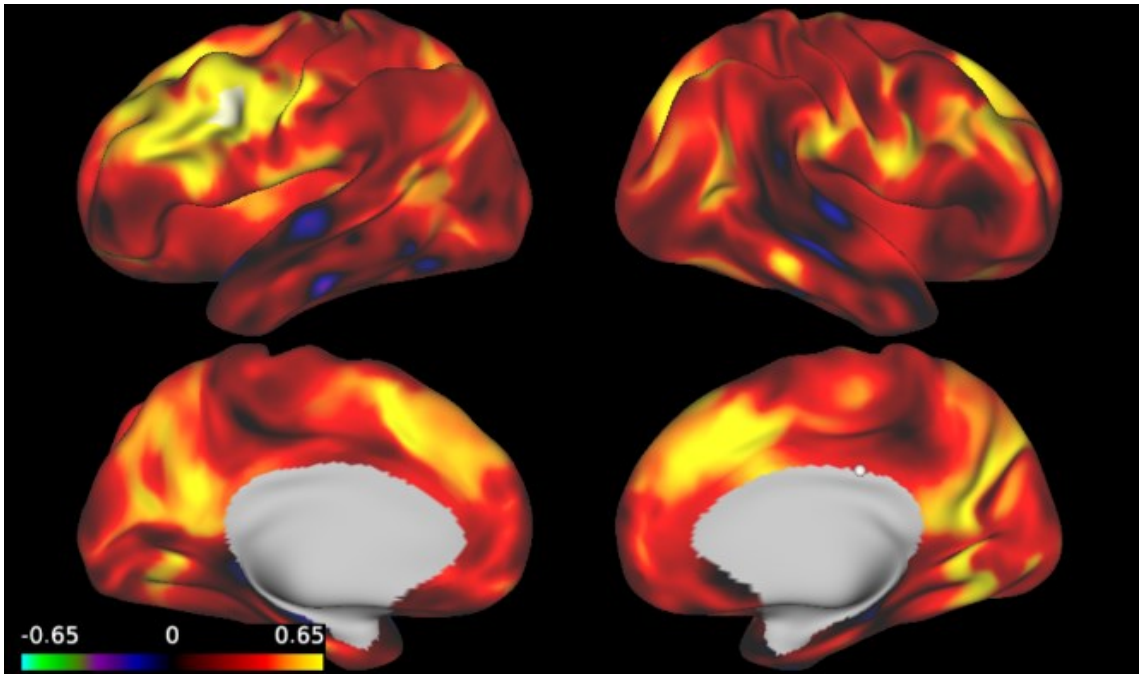

Figure 12: *Correlations with ROI1 (white) of subject C9ORF111 after manual ICA denoising and with 6 mm smoothing. Large cluster with high correlations around the seed region. Small cluster with high correlations in the inferior occipitotemporal region and along the intraparietal sulcus left hemispheric.*

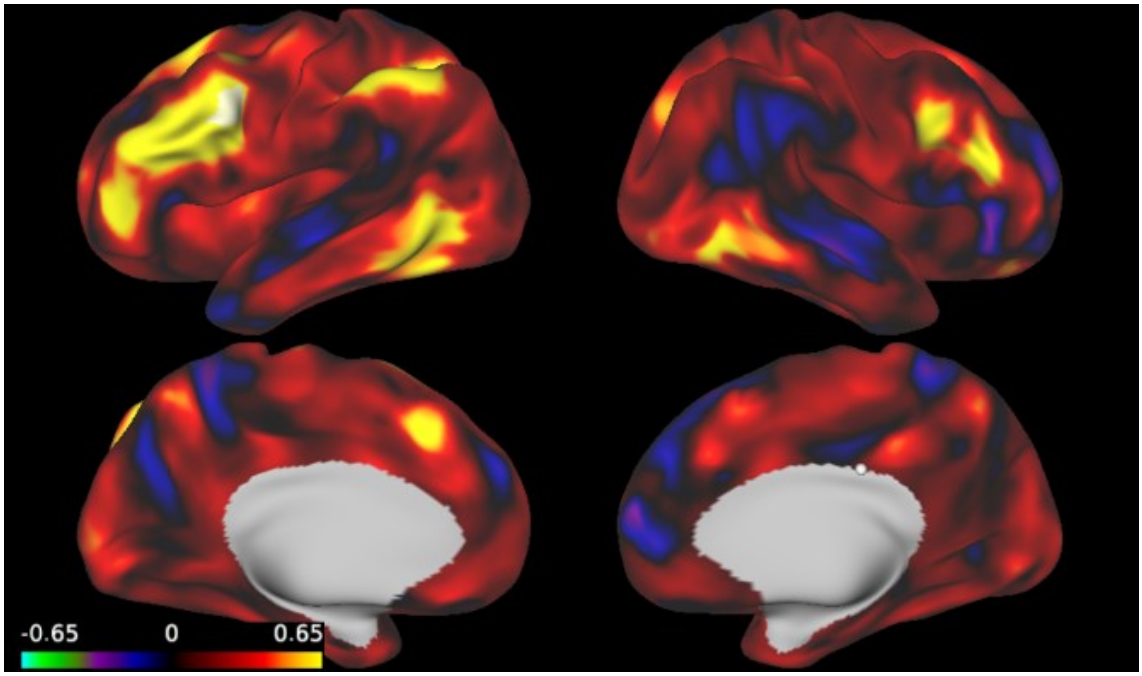

Figure 13: *Correlations with ROI1 (white) of subject C9ORF037 after manual ICA denoising and with 6 mm smoothing. Sharply delineated clusters with high correlations around the seed region, in the inferior occipitotemporal region and along the intraparietal sulcus.*

3.2.3 Comparison of the different ICA denoising methods

3.2.3.1 Subtraction images of different ICA denoising methods

To visualize the changes in the respective denoising method for the entire group of subjects in each vertex, I created difference images of the correlation maps with the different ICA denoising methods. Subtraction images for HCP ICA denoising subtracted from no ICA denoising, manual ICA denoising subtracted from HCP ICA denoising, and manual ICA denoising subtracted from no ICA denoising were created. Figure 14 shows the subtraction images for all 3 ROIs. In each case, this was the group mean of the subtraction images from all 75 subjects. In the subtraction images noICA - hcpICA (Figure 14 a, b, c), high positive difference values were seen, especially in the frontal cortex. This meant that a reduction of signal components by HCP ICA denoising seemed to have taken place here compared to no ICA denoising. In the subtraction images hcpICA - manICA (Figure 14 d, e, f), only very small positive difference values were found distributed over the entire brain. Therefore, there did not seem to be a great difference between the correlation maps with HCP or manual ICA

denoising. However, there was a tendency towards lower correlation values with manual ICA denoising compared to HCP ICA denoising, so greater denoising of the data seemed to take place with manual ICA denoising. The subtraction images noICA - manICA (Figure 14 g, h, i) showed a clear difference between no ICA and manual ICA denoising. Compared to the other subtraction images, there were noticeably higher difference values across the entire brain. The differences between no ICA and manual ICA denoising were particularly pronounced in the frontal and parietal cortex. The slight differences in noICA - hcpICA and hcpICA - manICA thus added up to a major difference in noICA - manICA. It could be seen that the HCP ICA denoising, considered over the whole group, showed a meaningful effect of signal reduction compared to no ICA denoising. However, this must be viewed with caution because, as shown in chapter 3.2.2, no meaningful results were achieved by HCP ICA denoising in some subjects. It was also clear that manual ICA denoising offered a clear advantage over no ICA denoising in cleaning the data and was also superior to HCP ICA denoising for our dataset.

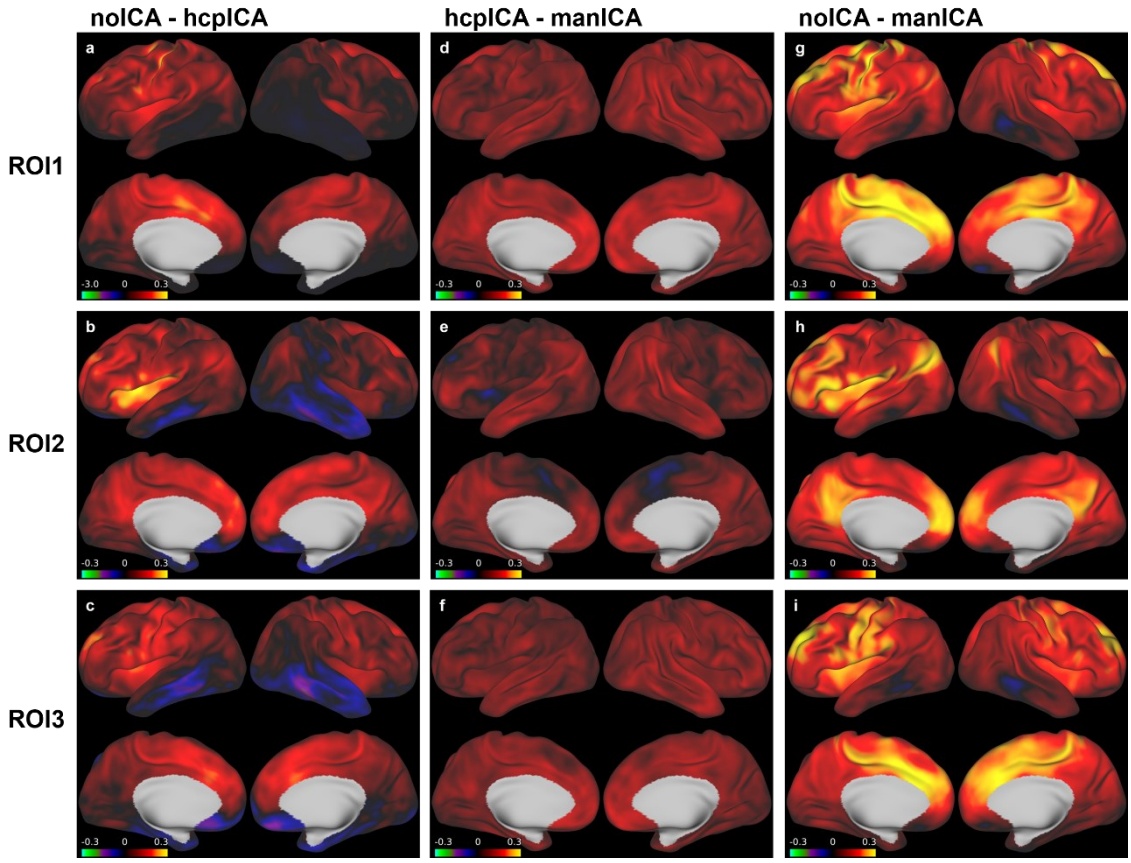

Figure 14: *Subtraction images of the correlation maps with different ICA denoising methods. All correlation maps shown were the group mean values from all 75 subjects. The first column shows the correlation maps for which the correlation maps with HCP ICA denoising were subtracted from the correlation maps without ICA denoising (noICA - hcpICA). The middle column shows the correlation maps for which the correlation maps with manual ICA denoising were subtracted from the correlation maps with HCP ICA (hcpICA - manICA). The third column shows no ICA denoising subtracted by manual ICA denoising (noICA - manICA). The first row represents the differential images of the correlation maps for ROI1, the second row for ROI2 and the third row for ROI3.*

3.2.3.2 Paired t-tests different ICA denoising methods

In order to statistically quantify the changes in the correlation maps due to the different ICA denoising, paired t-tests were carried out with the correlation maps of all subjects. One paired t-test was conducted that tested no ICA denoising against manual ICA denoising, another with no ICA denoising against HCP ICA denoising and one that tested HCP ICA denoising against manual ICA denoising.

The paired t-test, which tested the correlation maps of all subjects with no ICA denoising against the correlation maps with manual ICA denoising, showed highly significant results for the contrast noICA > manICA, distributed across the entire brain. As shown in Figure 15, for $p < 0.001$ with fwer-correction, there were

several large clusters distributed across the whole brain, especially in the frontal and parietal cortex, that had a significantly higher correlation without ICA denoising relative to the correlations that occurred after manual ICA denoising. This effect was visible for all 3 ROIs. This shows that manual ICA denoising removed large signal components across the entire brain and thus provided a good reduction of noise.

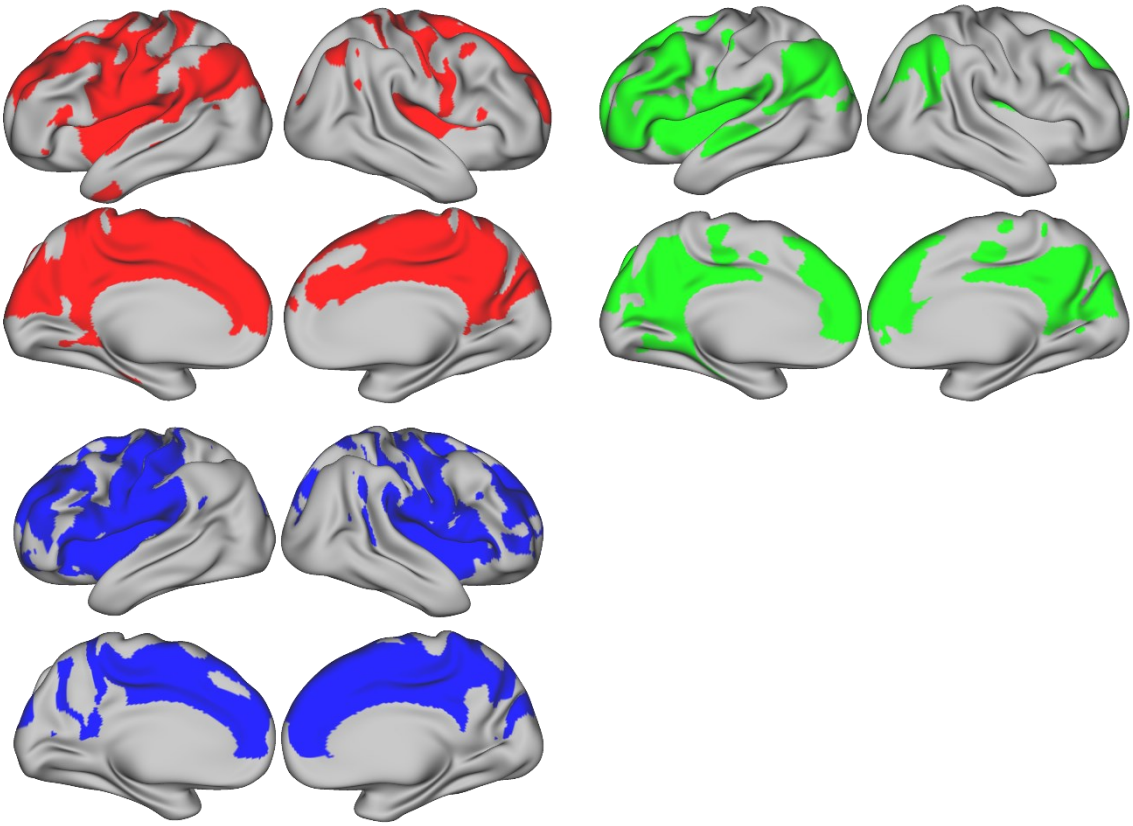

Figure 15: *In red reduced correlations for ROI1, in green for ROI2 and in blue for ROI3 in manually ICA denoised data relative to data without ICA denoising. Vertex-wise global threshold of p < 0.001 with fwer-correction.*

For the paired t-test no ICA against HCP ICA denoising, there were no significant results for both directions of the test at the significance level of $p < 0.001$ with fwer-correction. However, when looking at the data with a $p < 0.05$ uncorrected for multiple comparisons, there were isolated clusters that had increased correlations in the non-ICA denoised data relative to the HCP ICA denoised data.

For the paired t-test HCP ICA against manual ICA denoising, there were also no significant results for both directions of the test for the significance level $p < 0.001$

with fwer-correction. However, here too, very small clusters could be found with a higher correlation for the HCP denoised data compared to the manually denoised data, for a significance level of $p < 0.05$ uncorrected for multiple comparisons. The clusters that could be found in this test were smaller compared to the t-test no ICA against HCP ICA denoising. It seemed that ICA denoising with the HCP pipeline did a slightly better job of cleaning the data than if no ICA denoising was done at all.

In reviewing these results, I decided to continue my analyses with the manually ICA denoised data, since, as shown in Figure 15, these showed a highly significant difference compared to the data without ICA denoising. There also seemed to be an advantage in manual ICA denoising compared to HCP ICA denoising for this dataset, as could be seen from looking at the subtraction images and exploring the paired t-test data in more detail.

3.3 Correlation network maps within groups

Based on the three regions that showed cortical degeneration in FTD patients with apraxia in the studies of Wabersich-Flad (Doctoral thesis, Faculty of Medicine, Eberhard Karls Universität Tübingen, 2021), seed-based correlation analyses were performed. In order to compare the correlation maps between the three groups of subjects, I calculated an average correlation map based on the individual correlation maps of the subjects in the respective group. For this purpose, I used the correlation maps of each subject, created with the manually ICA cleaned data and 9 mm smoothing.

3.3.1 Correlation with ROI1

For the following correlation network maps ROI1 was used as the seed region. The correlation map of group M+A+ (Figure 16) showed a large cluster of high correlations around the seed region in the left hemisphere in the middle frontal gyrus. In addition, a somewhat smaller cluster of high correlations was found in the left intraparietal sulcus. Furthermore, high correlations were found in the area of the anterior cingulum on the left hemisphere. A small cluster of high correlations was also found contralateral to the seed region. The correlation map of group M-A- (Figure 17) showed a somewhat larger cluster with high

correlations around the seed region. The cluster in the area of the intraparietal sulcus on the left was more pronounced. On the right hemisphere, there was also a small cluster in the area of the intraparietal sulcus and the cluster contralateral to the seed region had higher correlations than in group M+A+. The correlation map of M+A- (Figure 18) had a smaller cluster with high correlations around the seed region compared to that of group M+A+ (Figure 16). Similar to group M+A+, there was a small cluster with high correlations contralateral to the seed region. The cluster in the intraparietal sulcus also showed similarly high correlations as in group M+A+.

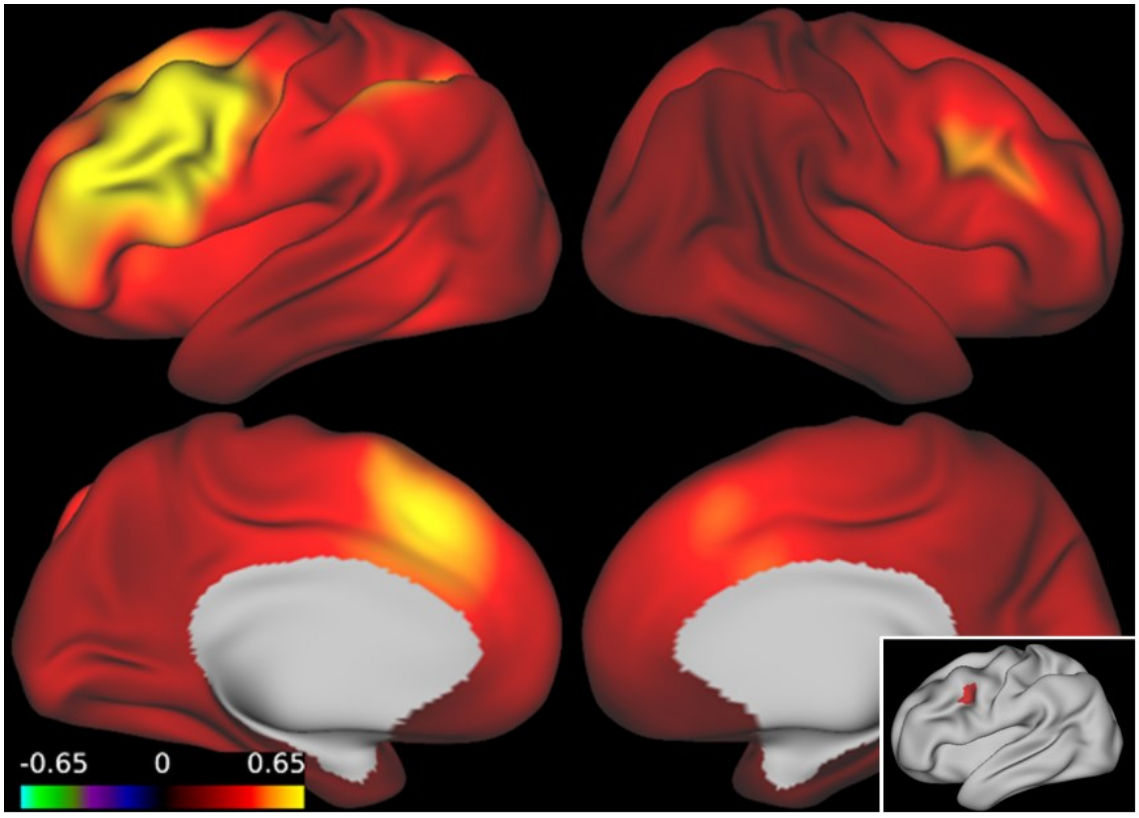

Figure 16: *Mean correlation network map of group M+A+ with ROI1 (bottom right corner in red) as the seed region. High correlations around the middle frontal gyrus. High correlations in the intraparietal sulcus on the left hemisphere.*

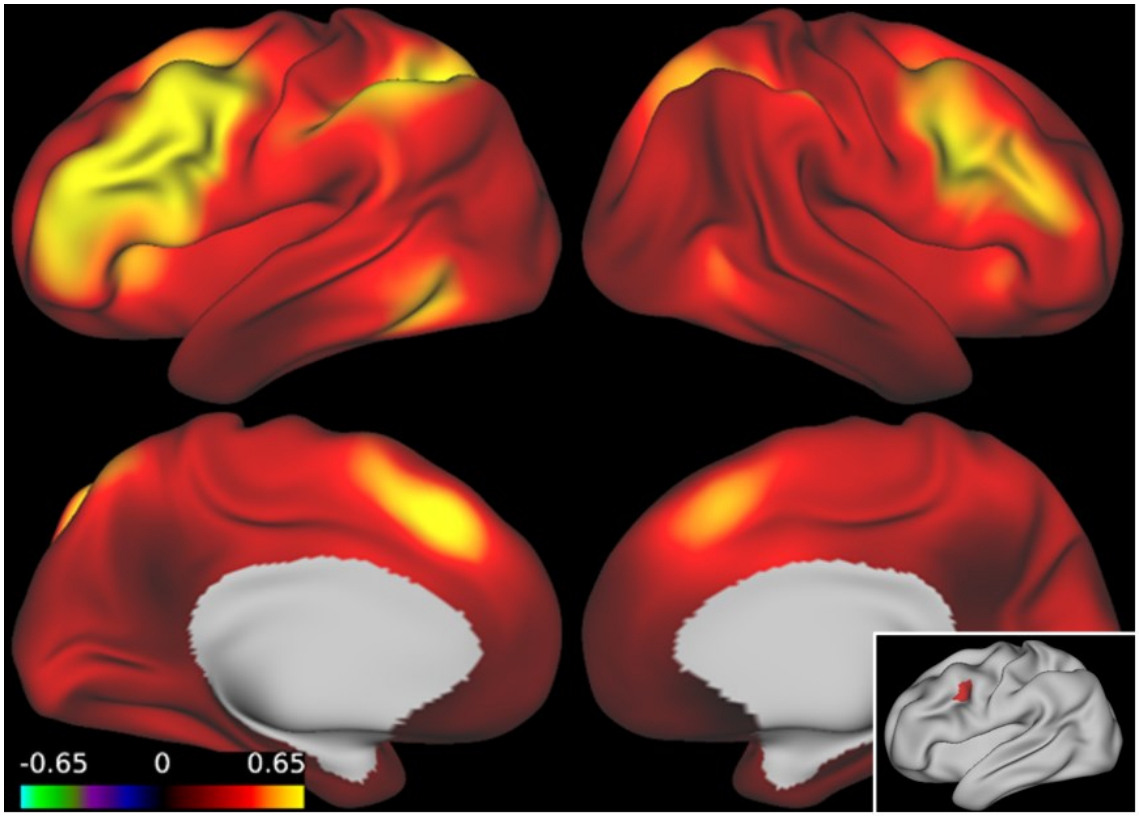

Figure 17: *Mean correlation network map of group M-A- with ROI1 (bottom right corner in red) as the seed region. High correlations around the middle frontal gyrus, in the intraparietal sulcus and the inferior occipitotemporal region.*

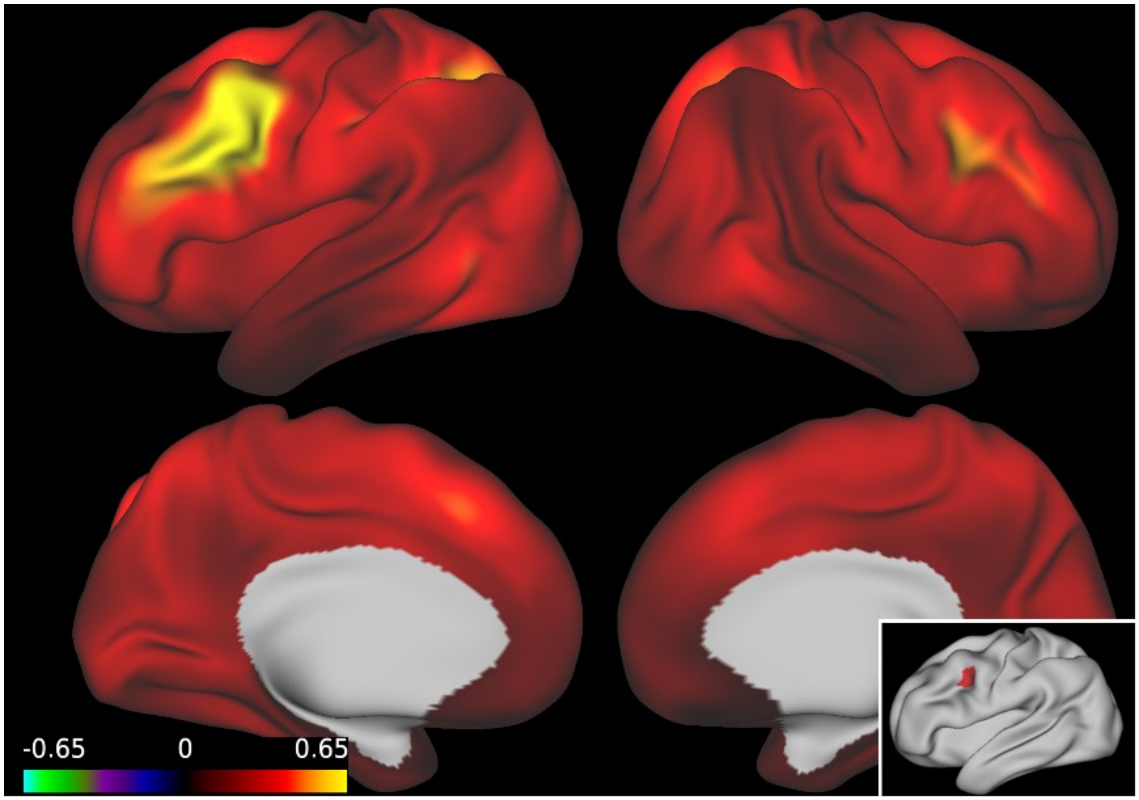

Figure 18: *Mean correlation network map of group M+A- with ROI1 (bottom right corner in red) as the seed region. High correlations around the seed region and in the intraparietal sulcus.*

3.3.2 Correlation with ROI2

The following correlation analyses were made based on ROI2 as seed region. The correlation map of group M+A+ (see Figure 19) showed a large cluster with high correlations around ROI2, especially in the inferior frontal gyrus and in the insula. A small cluster with high correlations was also found contralateral to the seed region. Furthermore, on both hemispheres, relatively high correlations were found in the anterior cingulum. Comparing the correlation map of group M-A- (Figure 20) with that of group M+A+ (Figure 19), a somewhat larger cluster with high correlations around the area of ROI2 could be seen. In group M-A-, this extended into the supramarginal gyrus. In addition, the cluster contralateral to the seed region was more pronounced and higher correlations were also found in the anterior cingulum. A comparison of group M+A- (Figure 21) with group M+A+ (Figure 19) showed a smaller cluster around ROI 2 with high correlations. This was also the case for the cluster contralateral to the seed region.

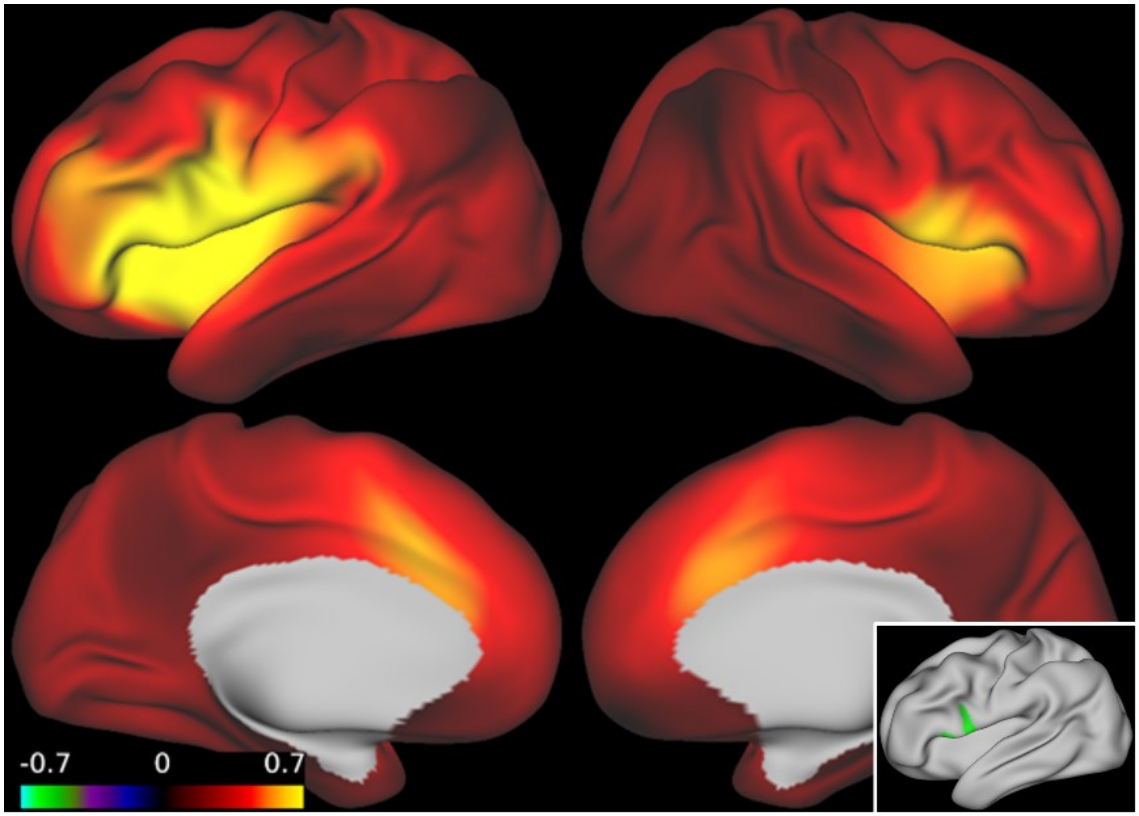

Figure 19: *Mean correlation network map of group M+A+ with ROI2 (bottom right corner in green) as the seed region. High correlations around ROI2 and contralateral.*

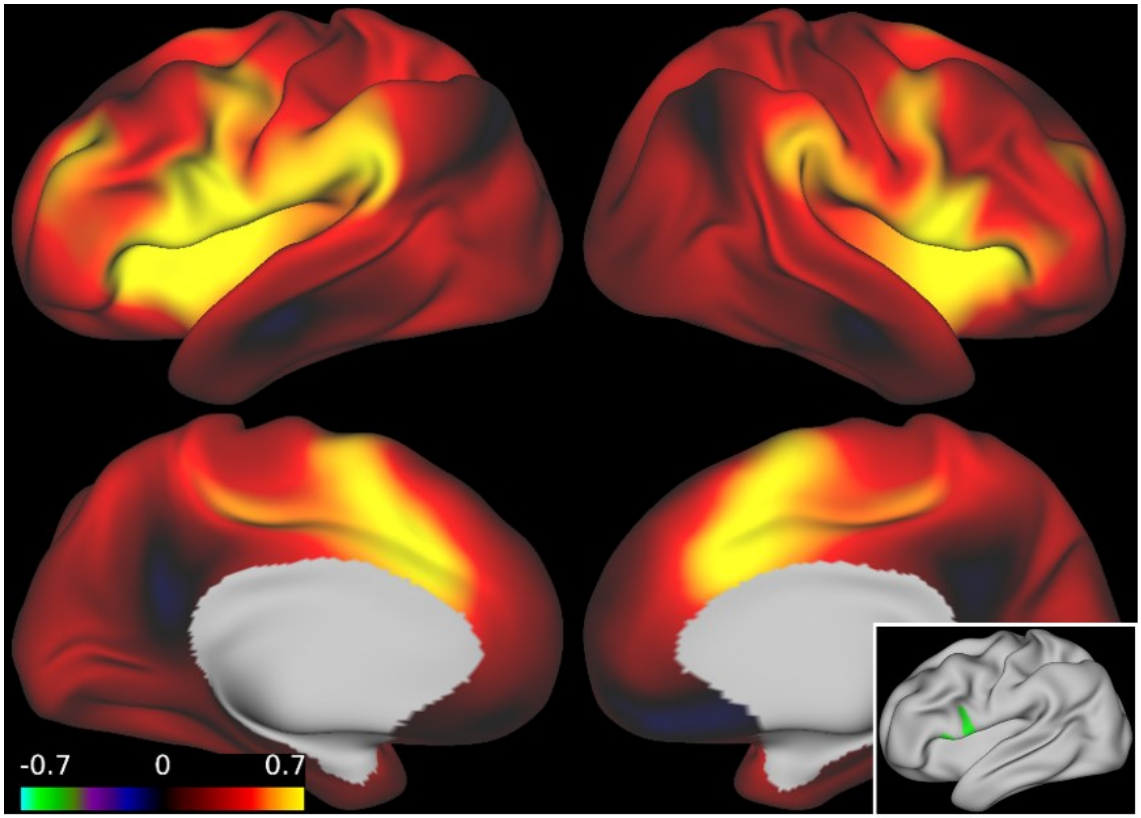

Figure 20: *Mean correlation network map of group M-A- with ROI2 (bottom right corner in green) as the seed region. High correlations around ROI2 and contralateral. High correlations in the anterior cingulum and the supramarginal gyrus on both hemispheres.*

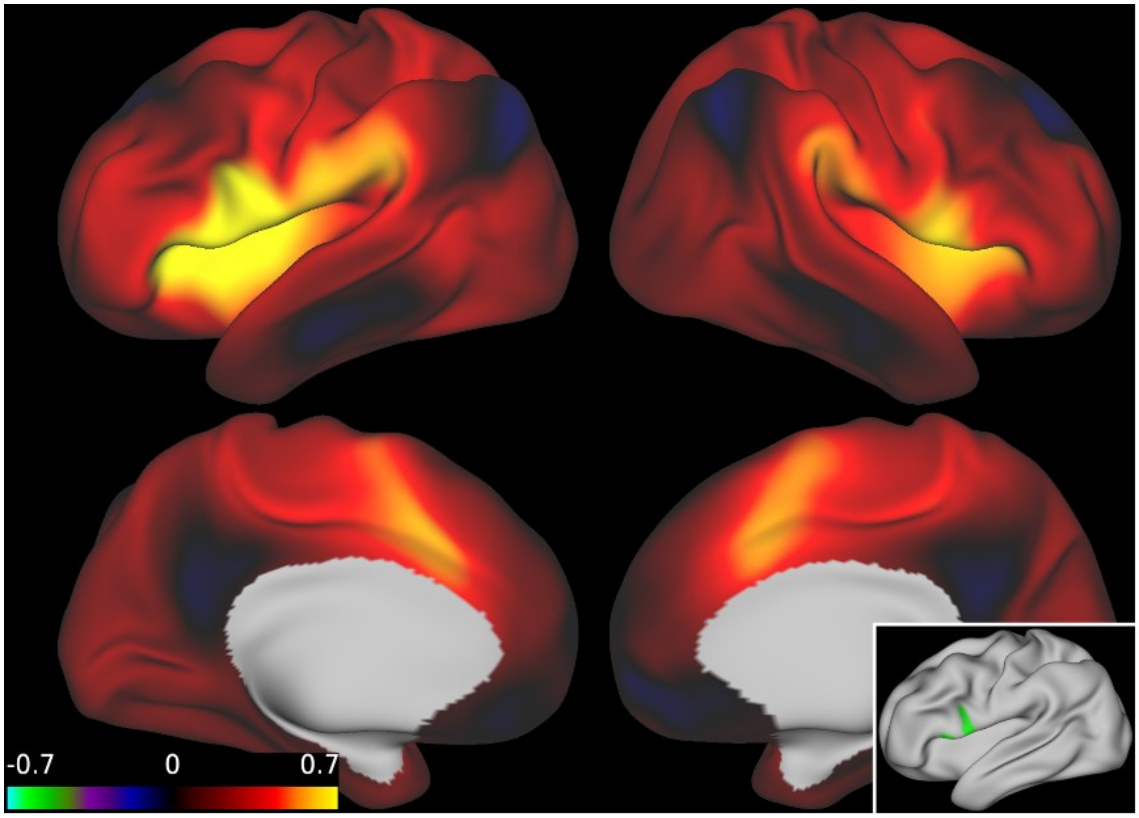

Figure 21: *Mean correlation network map of group M+A- with ROI2 (bottom right corner in green) as the seed region. High correlations around ROI2 and contralateral.*

3.3.3 Correlation with ROI3

These correlation analyses were performed with ROI 3 as the seed region. The correlation map of group M+A+ (Figure 22) showed a large cluster with high correlations in the region of ROI3. High correlations were also found contralateral to the seed region. In addition, relatively high correlations were found in the region of the intraparietal sulcus and inferior occipitotemporal on the left hemisphere. In the anterior cingulum high correlations were found on both hemispheres, especially on the left hemisphere. The correlation map of group M-A- (Figure 23) showed a slightly larger cluster with high correlations in the seed region compared to that of group M+A+ (Figure 22). Noticeably higher correlations were found in the intraparietal sulcus and inferior occipitotemporal on the left hemisphere. A somewhat larger cluster with higher correlations was also found contralateral to the seed region. A comparison of groups M+A- (Figure 24) and M+A+ (Figure 22) revealed a less extended cluster with high correlations in the seed region and contralateral to the seed region for group M+A-.

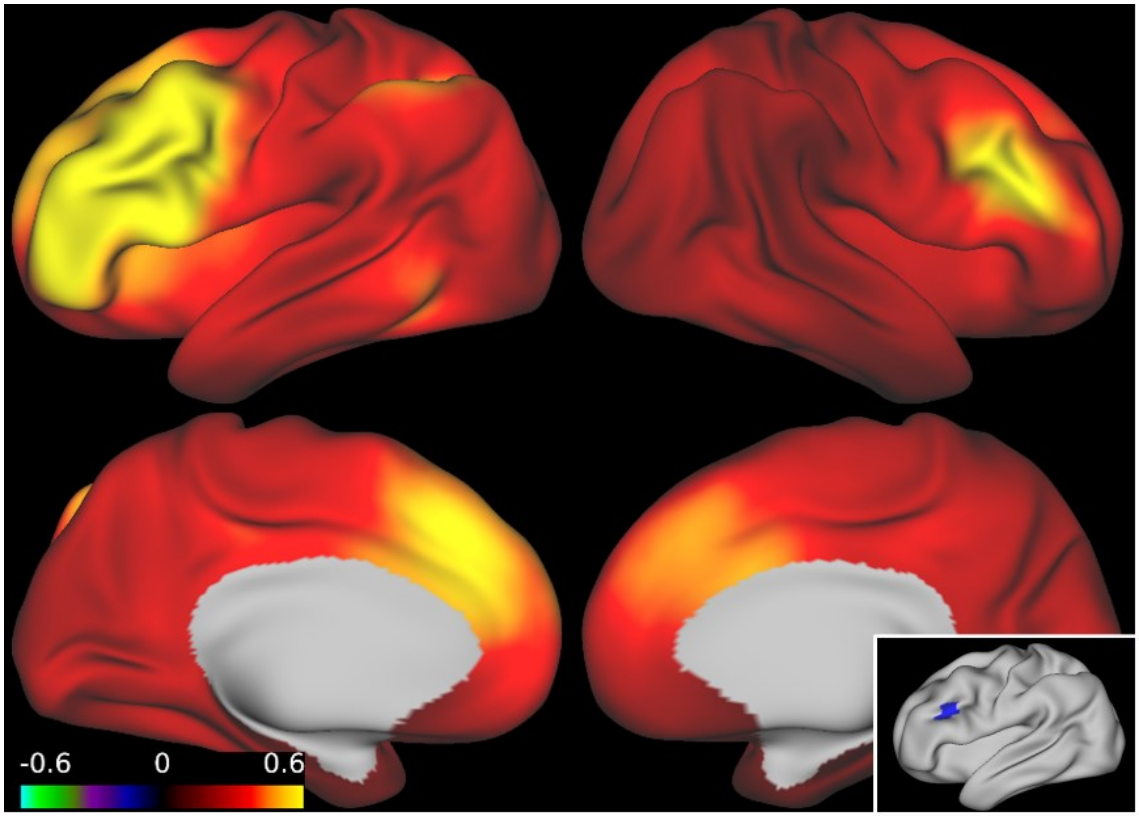

Figure 22: *Mean correlation network map of group M+A+ with ROI3 (bottom right corner in blue) as the seed region. High correlations around ROI3 and contralateral as well as in the anterior cingulum. Small clusters of relatively high correlations in the intraparietal sulcus and inferior occipitotemporal area on the left hemisphere.*

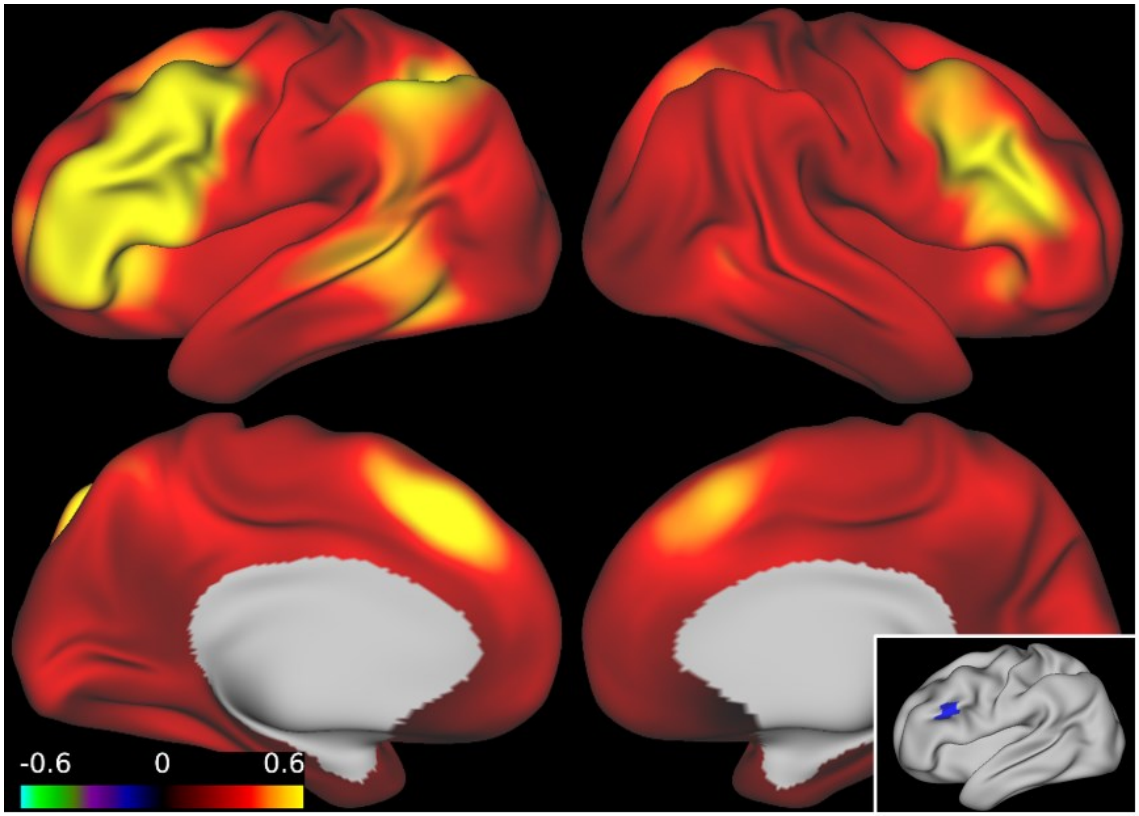

Figure 23: *Mean correlation network map of group M-A- with ROI3 (bottom right corner in blue) as the seed region. High correlations around ROI3 and contralateral as well as on the medial surface in the superior frontal gyrus. High correlations in the intraparietal sulcus and inferior occipitotemporal area predominantly on the left hemisphere.*

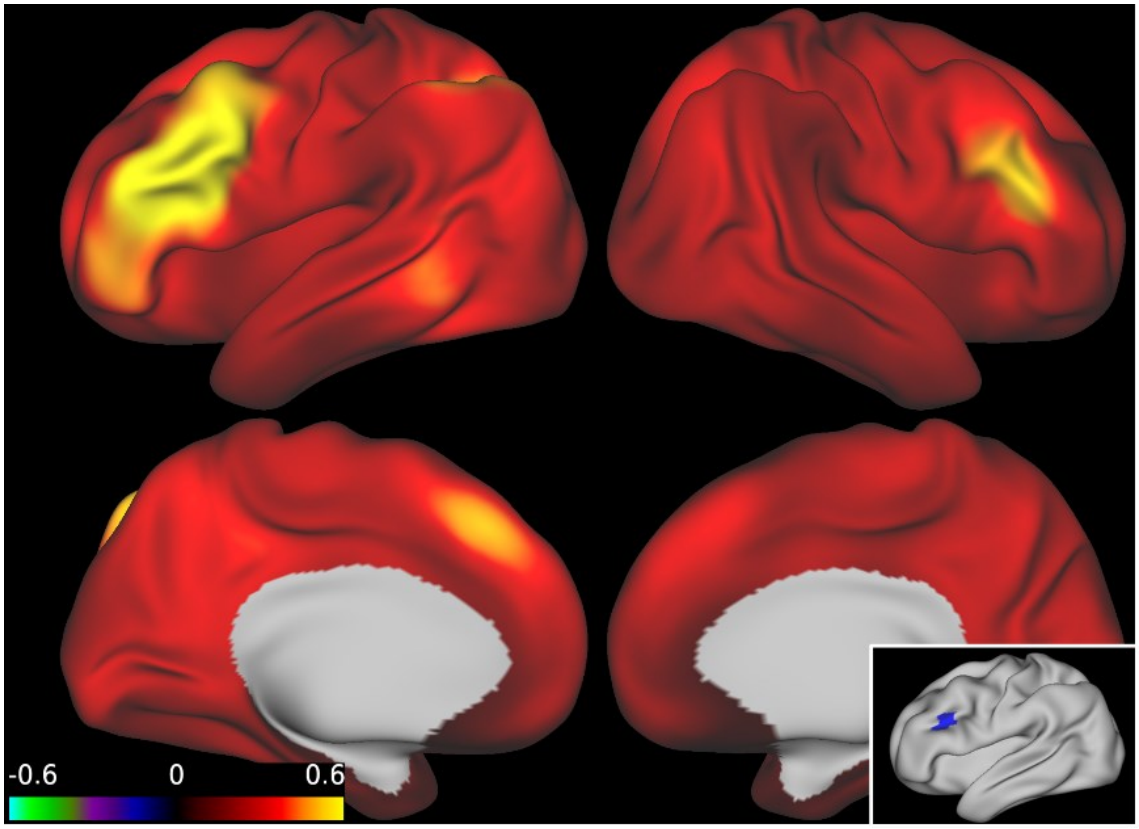

Figure 24: *Correlation map of group M+A- with ROI3 (bottom right corner in blue) as the seed region. High correlations around ROI3 and contralateral as well as on the medial surface in the superior frontal gyrus. Some high correlations in the intraparietal sulcus and inferior occipitotemporal area on the left hemisphere.*

3.3.4 Correlation with ROIall

For the following correlation network maps, ROIall was used as the seed region. The correlation map of M+A+ (Figure 25) showed a very large cluster with high correlations around the seed region ROIall. There was also a small cluster with high correlations contralateral to the seed region. Furthermore, there were high correlations in the area of the anterior cingulum. Compared to this, there was a larger cluster for M-A- (Figure 26) with high correlations contralateral to the seed region. The clusters in the anterior cingulum were also more pronounced. In addition, M-A- had a cluster with high correlations in the intraparietal sulcus and the supramarginal gyrus, predominantly on the left hemisphere. The correlation map of M+A- (Figure 27) showed a slightly smaller cluster of high correlations in the area of and contralateral to the seed region compared to M+A+.

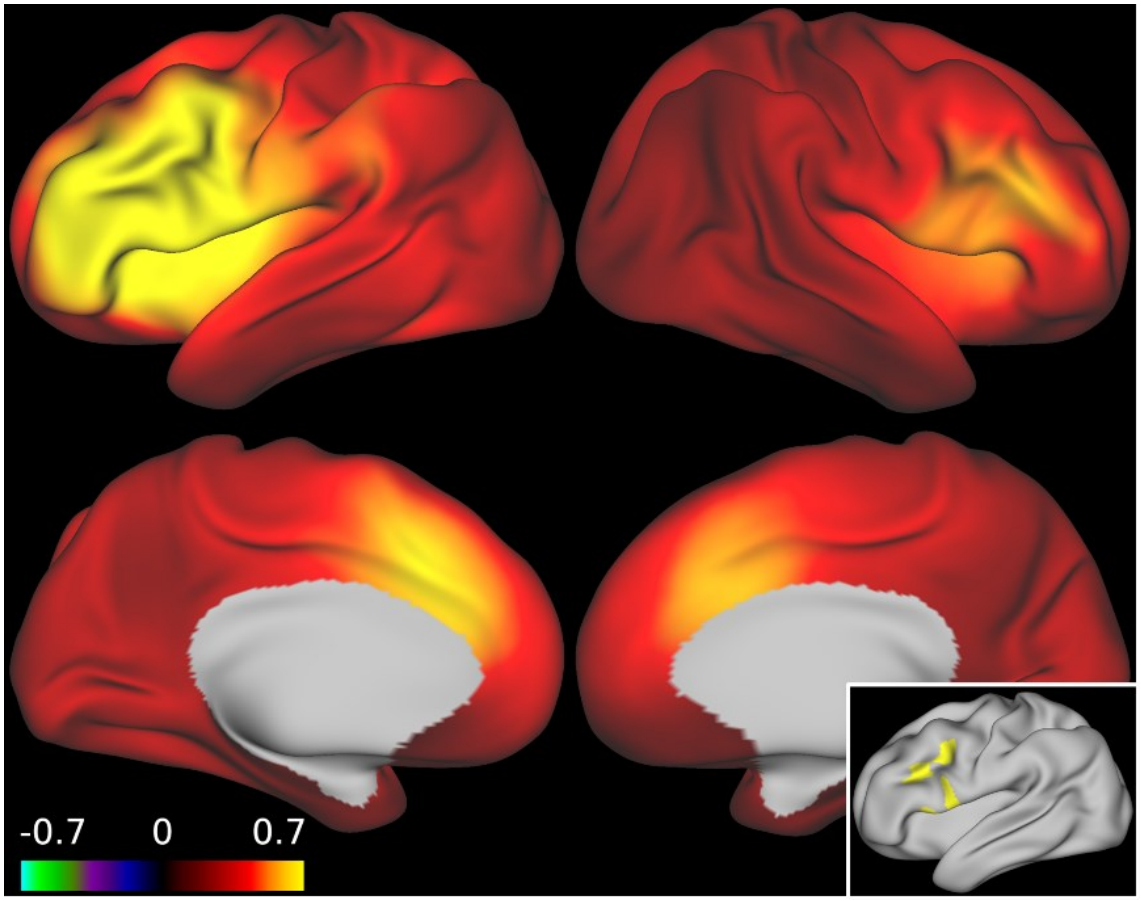

Figure 25: *Mean correlation network map of group M+A+ with ROIall (bottom right corner in yellow) as the seed region. High correlations around ROIall and contralateral as well as in the anterior cingulum.*

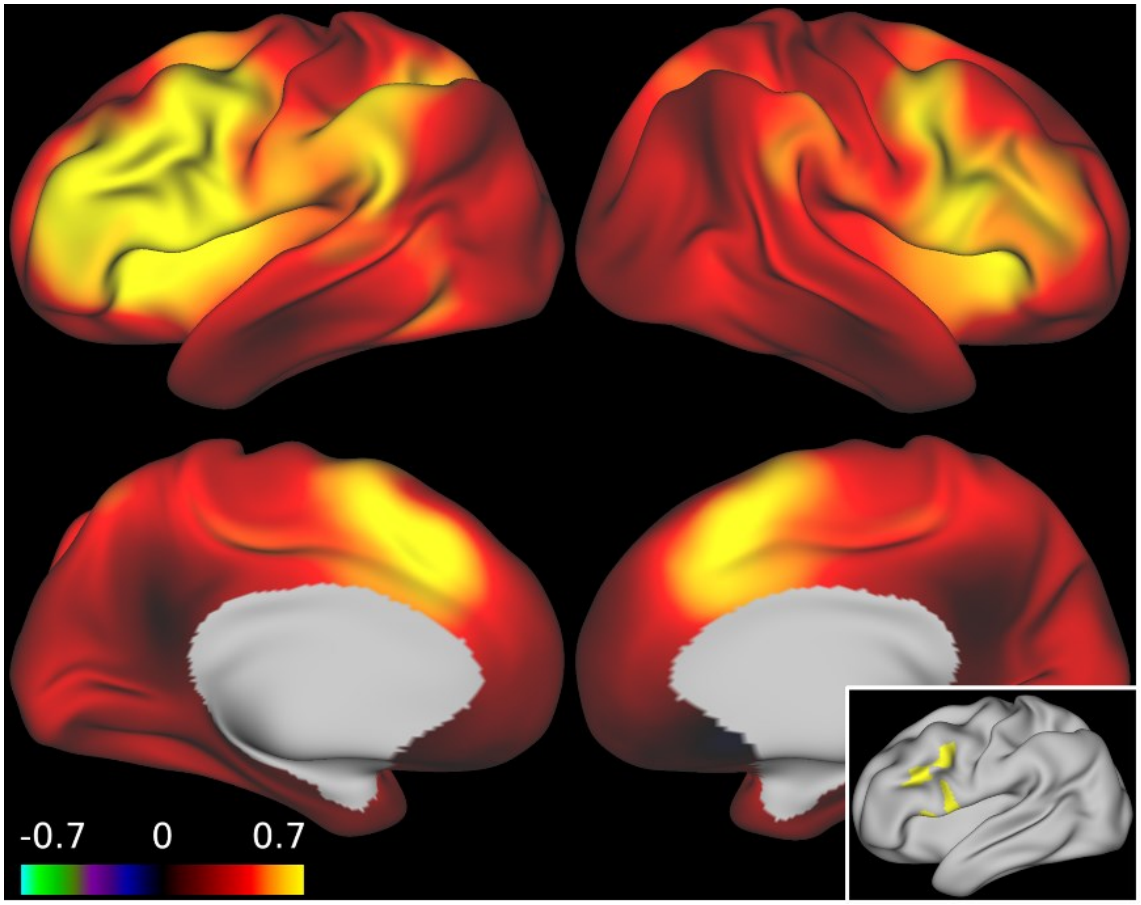

Figure 26: *Mean correlation network map of group M-A- with ROIall (bottom right corner in yellow) as the seed region. High correlations around ROIall and contralateral as well as in the anterior cingulum. Small cluster of relatively high correlations in the intraparietal sulcus and supramarginal gyrus predominantly on the left hemisphere.*

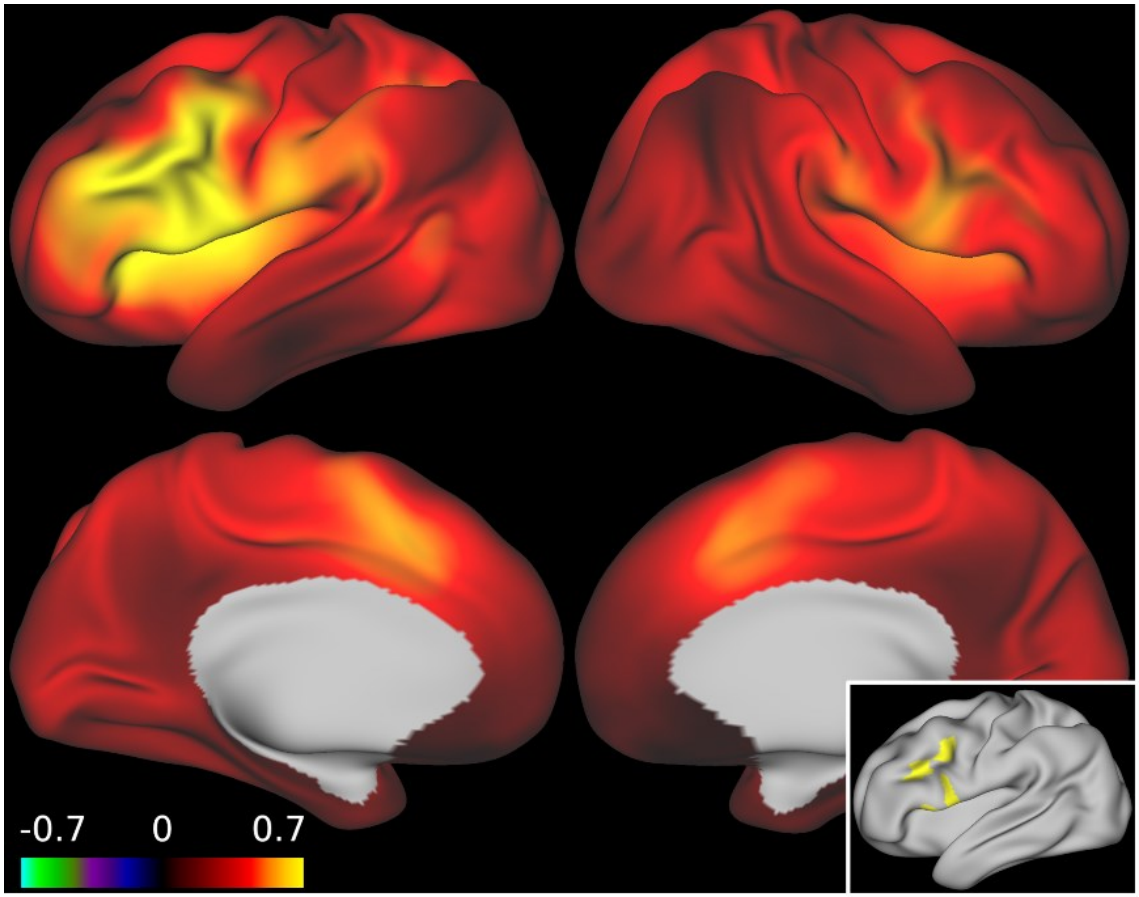

Figure 27: *Mean correlation network map of group M+A- with ROIall (bottom right corner in yellow) as the seed region. High correlations around ROIall. Small cluster of relatively high correlations contralateral to the seed region.*

A one-sample t-test with the correlation coefficients to show that there was indeed a significant difference in the group total from zero and not due to chance was not performed. The reason for this is that if a t-test were to be performed on the correlation maps shown above, the whole brain would become highly significant, as correlations deviating from 0 are consistently found for all subjects across the whole brain. As expected, there were areas that correlate very highly with the seed region, but there were hardly any areas that show no correlation at all. This is because, despite manual ICA denoising, there are still noise components in the data that contribute to low correlation across the brain. Performing such a t-test would therefore have no benefit.

3.4 Between group comparisons of network maps

Next, based on the correlation network maps between group comparisons were performed comparing the correlations of M+A+ with the correlations of M-A-, the correlations of M+A+ with the correlations of M+A- and the correlations of M+A- with M-A-. In each case, voxel-wise 2 sample t-tests were performed to determine whether there were significant differences in the correlations with the 3 seed regions between the two groups. Furthermore, the effect sizes for these between group comparisons were determined in order to obtain a measure about the strength of the differences in the correlations between the groups in addition to the p-values.

3.4.1 Reduced correlations in M+A+ relative to M-A-

The between group comparison of M+A+ relative to M-A- revealed reduced correlations in the apraxia group compared to the non-mutation carrier group for all 3 seed regions. This was in line with our hypothesis. In the bottom left inlay of Figure 28 the 3 seed regions in the left frontal lobe, ROI1 in red, ROI2 in green and ROI3 in blue are shown. Figure 28 shows the regions that had significantly reduced correlations with the corresponding seed region in M+A+ relative to M-A-. The regions shown in red are those with a reduced correlation with ROI1, in green are reduced correlations with ROI2 and in blue are reduced correlations with ROI3. A vertex wise global threshold of $p < 0.001$ was used, uncorrected for multiple comparisons. A large cluster with reduced correlations in group M+A+ relative to M-A- was found in the intraparietal sulcus on both hemispheres. On the right hemisphere, there was a cluster with reduced correlations in the supramarginal gyrus. Furthermore, clusters were found in the area of the premotor and supplementary motor cortex on the right. There was also a cluster of reduced correlations in the superior temporal gyrus on the left and the posterior middle temporal gyrus (pMTG) on the right. For the sake of a good exploration of the data, I also inspected the results with a threshold of $p < 0.01$, uncorrected for multiple comparisons. As expected, the clusters with reduced correlation for M+A+ relative to M-A- described above became larger. In addition, clusters with reduced correlations were now also found contralateral to the clusters already described on the right hemisphere. Thus, clusters were now found on the left

hemisphere in the area of the premotor cortex and the supplementary motor area (SMA), as well as in the area of the supramarginal gyrus. These newly found clusters could also be found when looking at the effect size maps for this analysis (Figure 29). Reduced correlations for M+A+ relative to M-A- were found with a high effect size in the intraparietal sulcus on both hemispheres, as well as inferior parietal, in the premotor cortex and SMA on both hemispheres, but more pronounced on the right hemisphere. Additionally, there were reduced correlations with high effect sizes in the left superior temporal gyrus and the right pMTG.

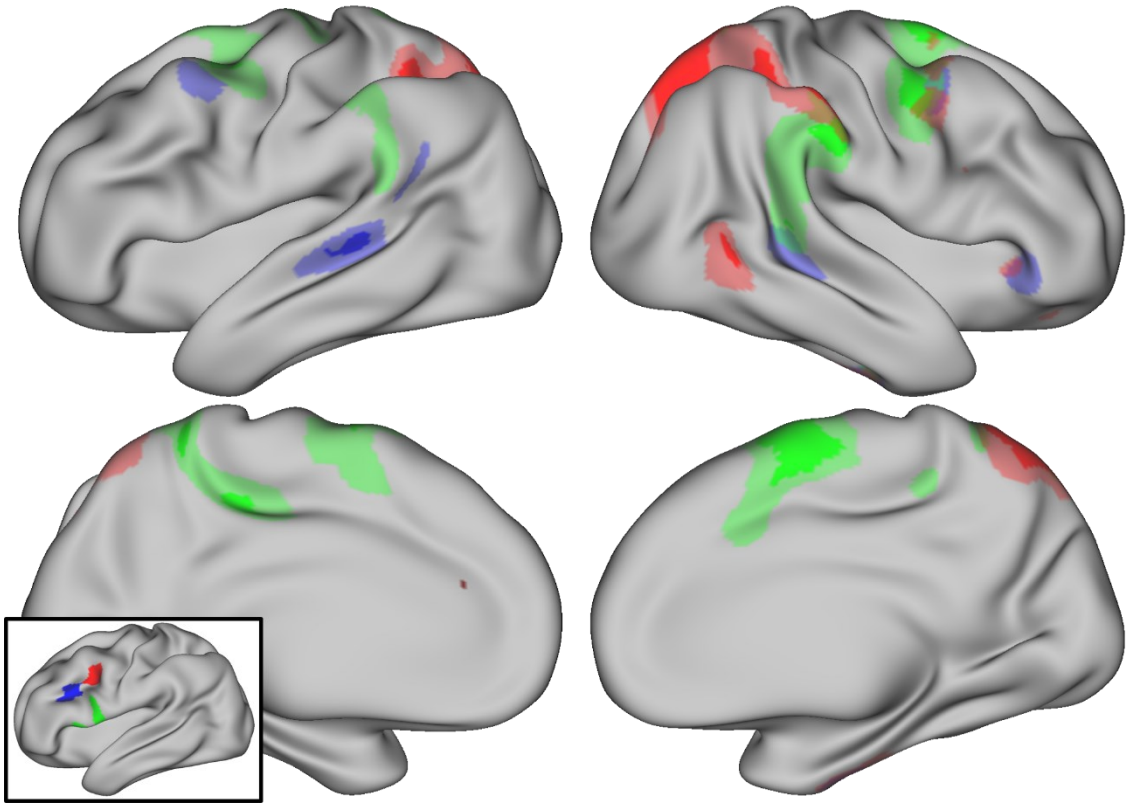

Figure 28: *Reduced correlations in M+A+ relative to M-A-. Vertex-wise global threshold of p < 0.001 uncorrected for multiple comparisons (brightly colored areas) and p < 0.01 uncorrected for multiple comparisons (translucently colored areas). In red reduced correlations with ROI1, in green reduced correlations with ROI2 and in blue reduced correlations with ROI3. In the lower left corner, the 3 seed regions based on which the analyses were carried out are shown, with ROI1 in red, ROI2 in green and ROI3 in blue.*

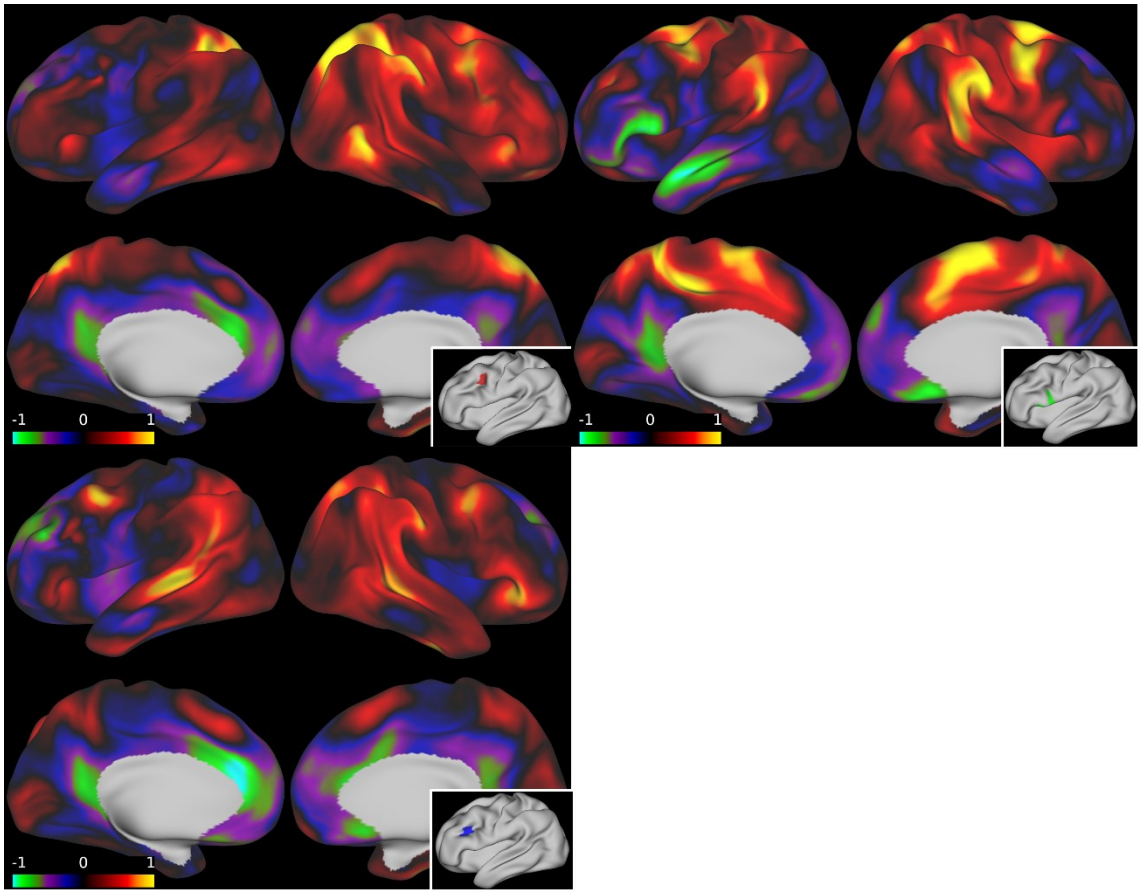

Figure 29: *Effect size maps for the group comparison M+A+ relative to M-A-. The vertex-wise Cohen's d value is shown. Yellow indicates that there is a large effect size for reduced correlations of M+A+ compared to M-A-, while green indicates that there is a large effect size for reduced correlations of M-A- compared to M+A+. The effect size map for the analysis with ROI1 is shown on the top left, for ROI2 on the top right and for ROI3 on the bottom left.*

3.4.2 Reduced correlations in M+A+ relative to M+A-

For the group comparison in which the correlations of M+A+ were compared with those of M+A-, no regions with significantly reduced correlations for the group M+A+ relative to M+A- emerged for a significance level of $p < 0.001$ uncorrected for multiple comparisons. Further exploration of the data with a significance level of $p < 0.01$ uncorrected for multiple comparisons revealed a cluster with reduced correlations for M+A+ relative to M+A- in the area of the intraparietal sulcus on the right hemisphere, as well as a very small cluster in the inferior parietal cortex and superior occipital cortex (see Figure 30). The effect size maps (Figure 31) for these analyses showed large effect sizes for reduced correlations for M+A+ relative to M+A- in the area of the intraparietal sulcus on the right hemisphere.

There were also slightly increased effect sizes in the inferior parietal cortex and supramarginal gyrus on the right. Furthermore, high effect sizes for increased correlations of M+A+ relative to M+A- were found in the frontal cortex, anterior cingulate and temporal lobe, predominantly on the left hemisphere.

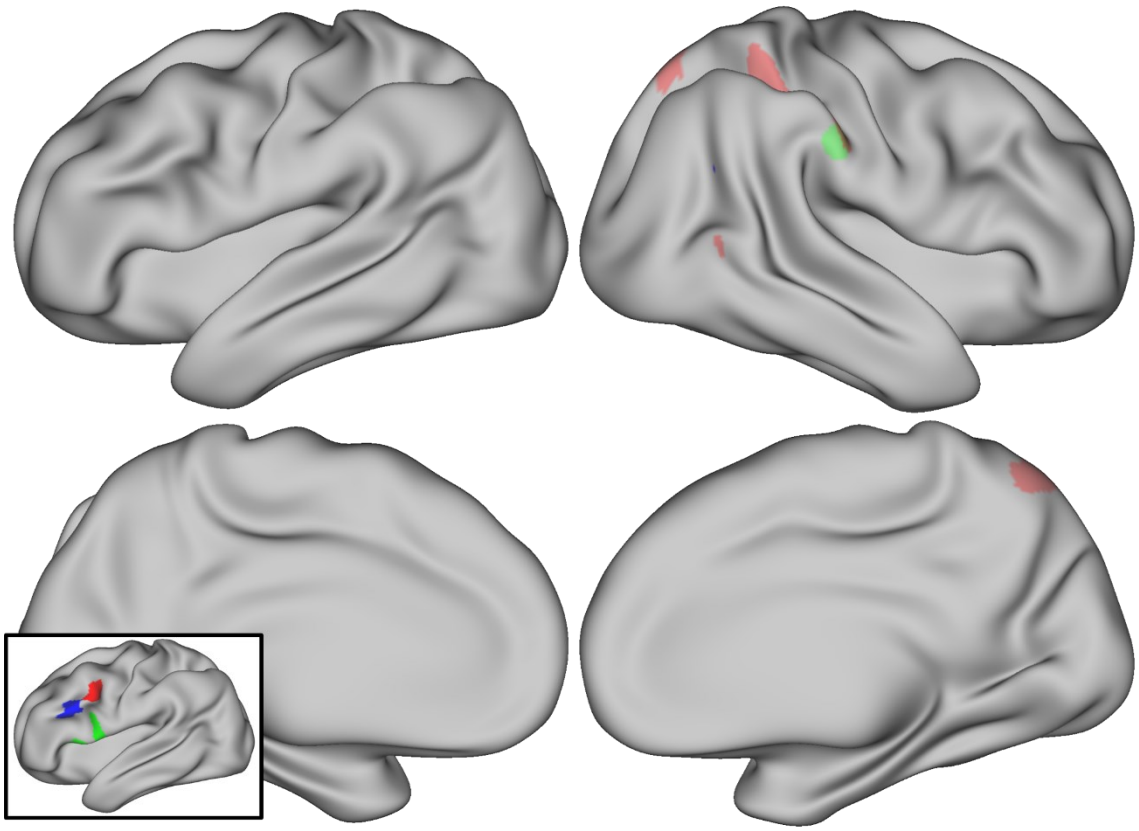

Figure 30: *Reduced correlations in M+A+ relative to M+A-. Vertex-wise global threshold of p < 0.01 uncorrected for multiple comparisons. In red reduced correlations with ROI1, in green reduced correlations with ROI2 and no reduced correlations with ROI3.*

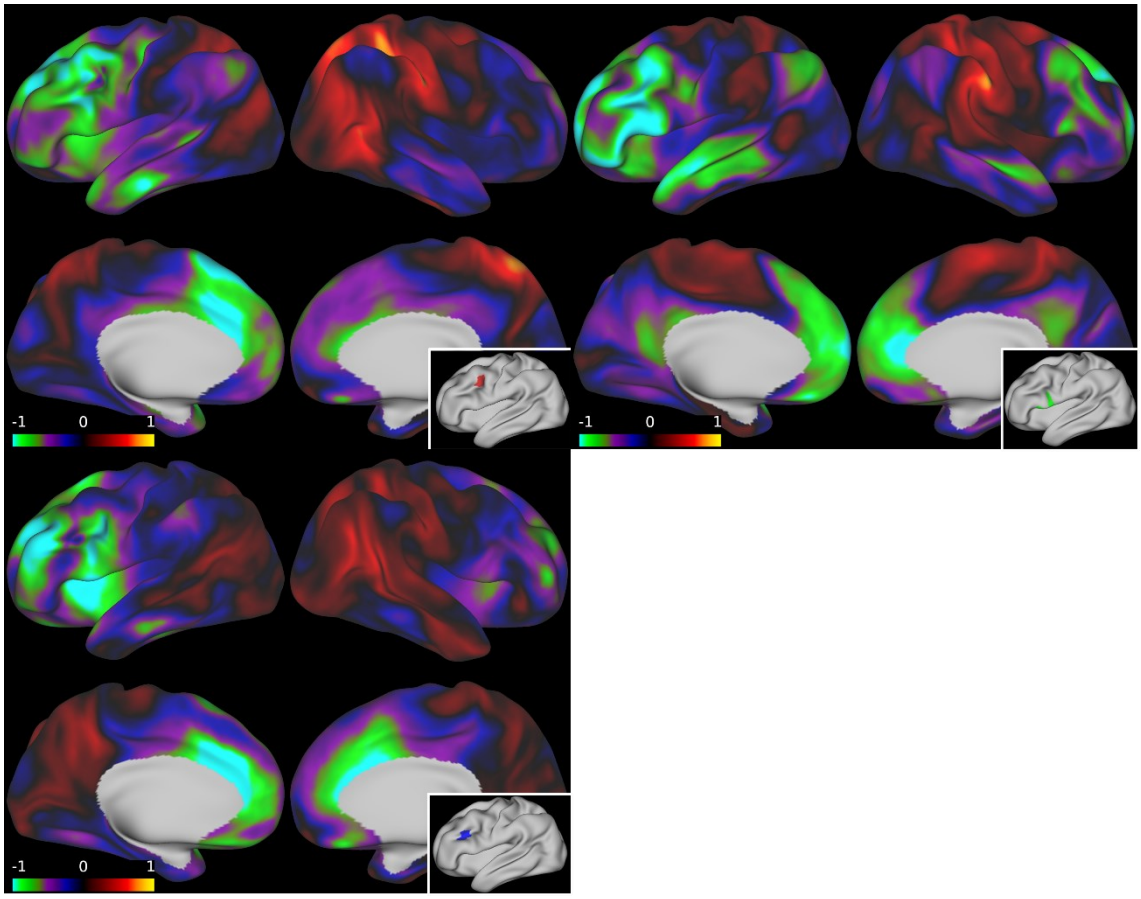

Figure 31: *Effect size maps for the group comparison M+A+ relative to M+A-. The vertex-wise Cohen's d value is shown. Yellow indicates that there is a large effect size for the reduced correlations of M+A+ compared to M+A-, while green means that there is a large effect size for reduced correlations of M+A- compared to M+A+. The effect size map for the analysis with ROI1 is shown on the top left, for ROI2 on the top right and for ROI3 on the bottom left.*

3.4.3 Reduced correlations in M+A- relative to M-A-

For the two-sample t-test M+A- versus M-A-, for a threshold of $p < 0.001$ uncorrected for multiple comparisons (see Figure 32), large clusters with reduced correlations for M+A- relative to M-A- were found in the area of the left middle frontal gyrus and the anterior insula for all 3 ROIs. In addition, clusters with reduced correlations were found in the region of the intraparietal sulcus and the anterior cingulate on both hemispheres. When exploring the data further at $p < 0.01$ uncorrected for multiple comparisons, in addition to the clusters already described that increased in size for this threshold, reduced correlations were found for M+A- relative to M-A- in the temporal lobe on both hemispheres and occipitotemporal on the left. Furthermore, clusters were found in the middle

frontal gyrus and anterior insula on the right hemisphere. The effect size maps (Figure 33) showed high effect sizes for reduced correlations of M+A- relative to M-A- in the area of the middle frontal gyrus, the anterior insula, the intraparietal sulcus and the anterior cingulate, predominantly on the left hemisphere.

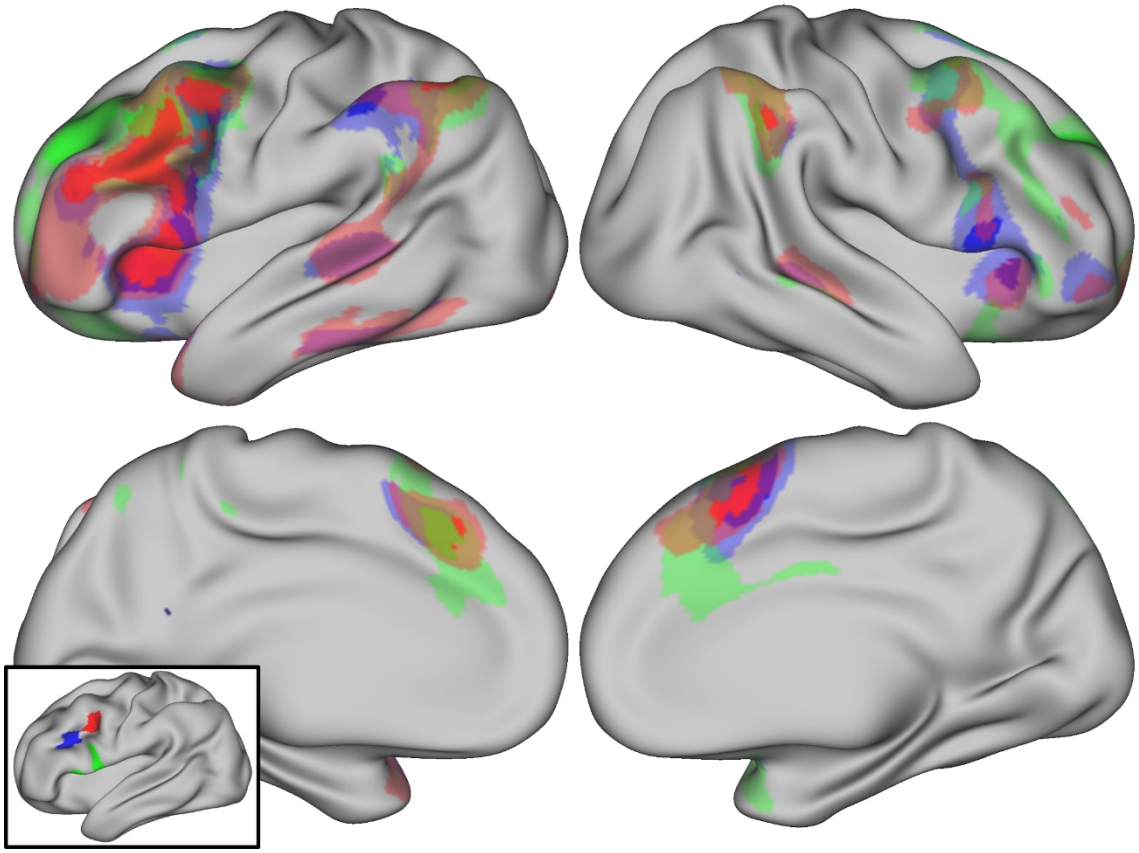

Figure 32: *Reduced correlations in M+A- relative to M-A-. Vertex-wise global threshold of p < 0.001 uncorrected for multiple comparisons (brightly colored areas) and p < 0.01 uncorrected for multiple comparisons (translucently colored areas). In red reduced correlations with ROI1, in green reduced correlations with ROI2 and in blue reduced correlations with ROI3. In the lower left corner, the 3 seed regions based on which the analyses were carried out are shown, with ROI1 in red, ROI2 in green and ROI3 in blue.*

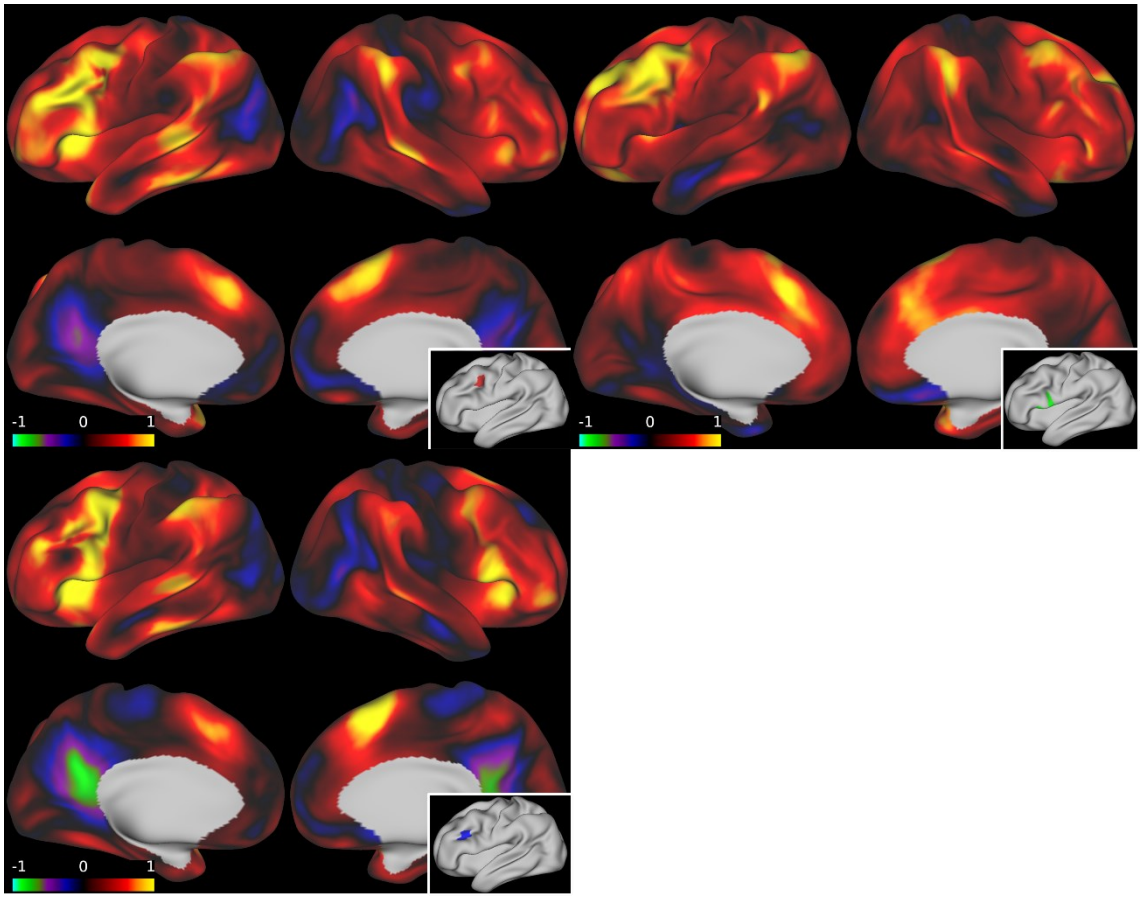

Figure 33: *Effect size maps for the group comparison M+A- relative to M-A-. The vertex-wise Cohen's d value is shown. Yellow indicates that there is a large effect size for the reduced correlations of M+A- compared to M-A-, while green means that there is a large effect size for reduced correlations of M-A- compared to M+A-. The effect size map for the analysis with ROI1 is shown on the top left, for ROI2 on the top right and for ROI3 on the bottom left.*

3.4.4 Between group comparisons of network maps with ROIall

The between group comparisons of network maps presented above were carried out based on 3 separate seed regions. However, the question arose as to whether it made sense to consider the 3 seed regions as 3 functionally separate regions. To investigate the hypothesis that the 3 ROIs were not functionally distinct regions, I performed between group comparisons based on correlation maps where the 3 seed regions were combined into one region of interest.

3.4.4.1 Reduced correlations in M+A+ relative to M-A-

Figure 34 shows the areas with reduced correlations with ROIall in group M+A+ relative to M-A-. With a threshold of $p < 0.001$ uncorrected for multiple comparisons, clusters with reduced correlations were found in the supramarginal

gyrus and intraparietal sulcus on the right hemisphere, as well as in the premotor cortex on the right significantly more than on the left. When looking at the data with a threshold of $p < 0.01$ uncorrected for multiple comparisons, the described clusters became larger. In addition, areas with reduced correlations were also found on the left hemisphere in the supramarginal gyrus and the intraparietal sulcus. When comparing these results with the results of the between group analyses based on the 3 separate seed regions, it was noticeable that the results on the right hemisphere were very similar to the results of the separately conducted between group comparisons. With ROIall, all regions were found that were also found by the separate group comparisons. ROIall also found regions that showed significant differences in the between group comparison only from one seed region. The only main difference compared to the 3 separately conducted between group comparisons was that the small cluster in the anterior insula on the right hemisphere was not shown here. Slightly smaller clusters with reduced correlations were found on the left hemisphere than in the three separate between group comparisons. The effect size map (Figure 35) shows high effect sizes for reduced correlations in M+A+ relative to M-A- in the supramarginal gyrus, intraparietal sulcus, SMA and premotor cortex, each more pronounced on the right than on the left hemisphere.

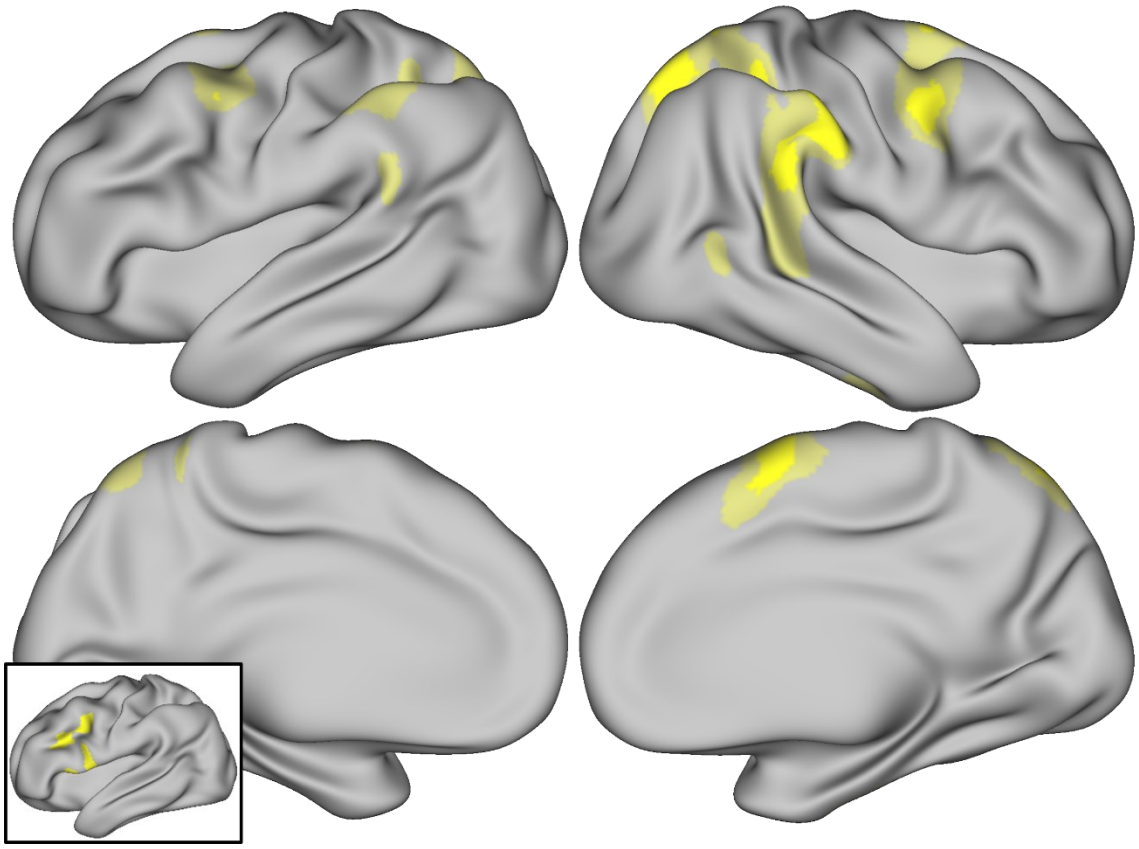

Figure 34: *Reduced correlations in M+A+ relative to M-A-. Vertex-wise global threshold of p < 0.001 uncorrected for multiple comparisons (brightly colored areas) and p < 0.01 uncorrected for multiple comparison (translucently colored areas). In yellow reduced correlations with ROIall are shown. In the lower left corner, the seed region ROIall, based on which the analysis was carried out is shown in yellow.*

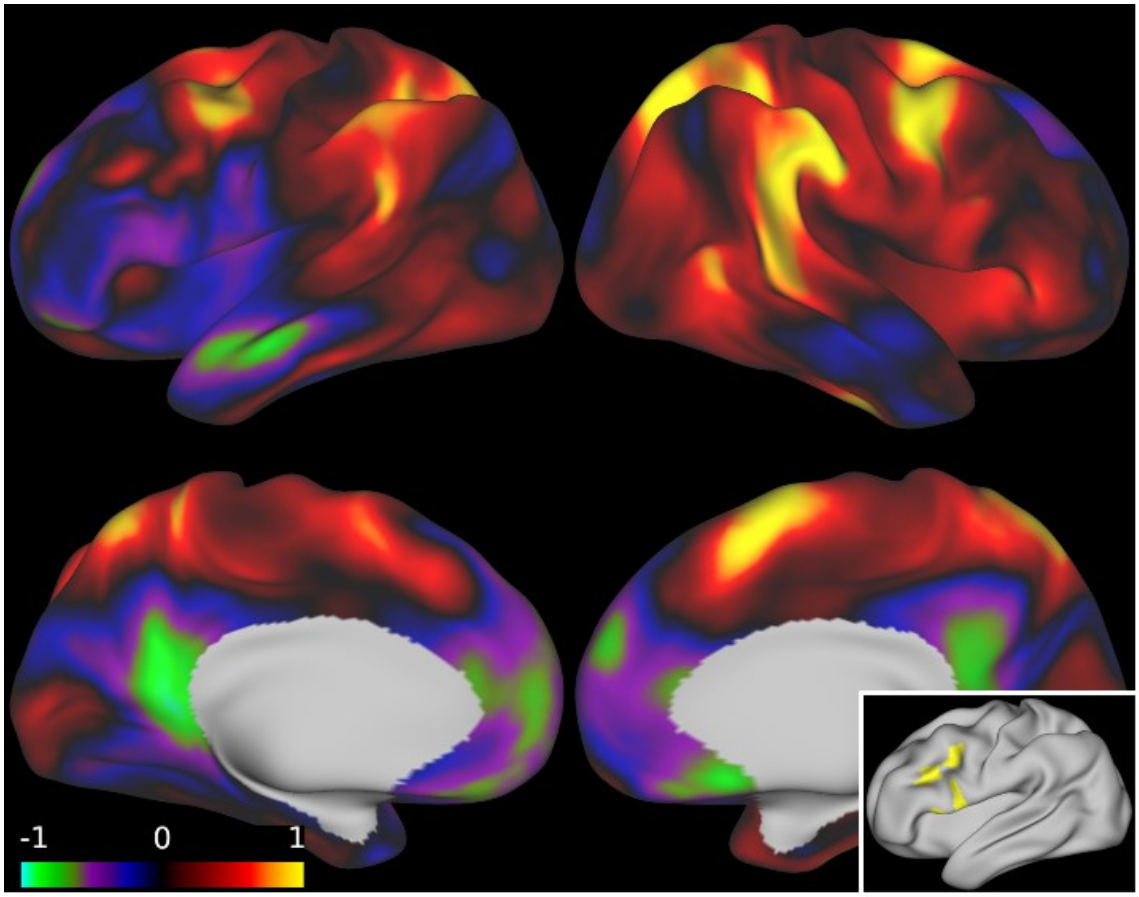

Figure 35: *Effect size map for the group comparison M+A+ relative to M-A-. The vertex-wise Cohen's d value is shown. Yellow indicates that there is a large effect size for the reduced correlations of M+A+ compared to M-A-, while green means that there is a large effect size for reduced correlations of M-A- compared to M+A+. The effect size map for the analysis with ROIall (bottom right corner) is shown.*

3.4.4.2 Reduced correlations in M+A+ relative to M+A-

For the between group comparison of M+A+ with M+A- for ROIall (Figure 36), a small cluster was found in the right intraparietal sulcus for a threshold of $p < 0.001$ uncorrected for multiple comparisons. This cluster became larger for $p < 0.01$ uncorrected for multiple comparisons. Compared to the results of this between group comparison with the results of the 3 separate ROIs, this cluster looked very similar. However, the small clusters in the occipital lobe and inferior parietal were not found for ROIall. The effect size map (Figure 37) shows high effect sizes for reduced correlations in M+A+ relative to M+A- in the area of the right intraparietal sulcus. There were slightly increased effect sizes in the area of the pMTG on both hemispheres, as well as in the intraparietal sulcus on the left. Furthermore, high

effect sizes for increased correlations in M+A+ relative to M+A- were found in the area of the frontal and temporal cortex, more pronounced on the left hemisphere.

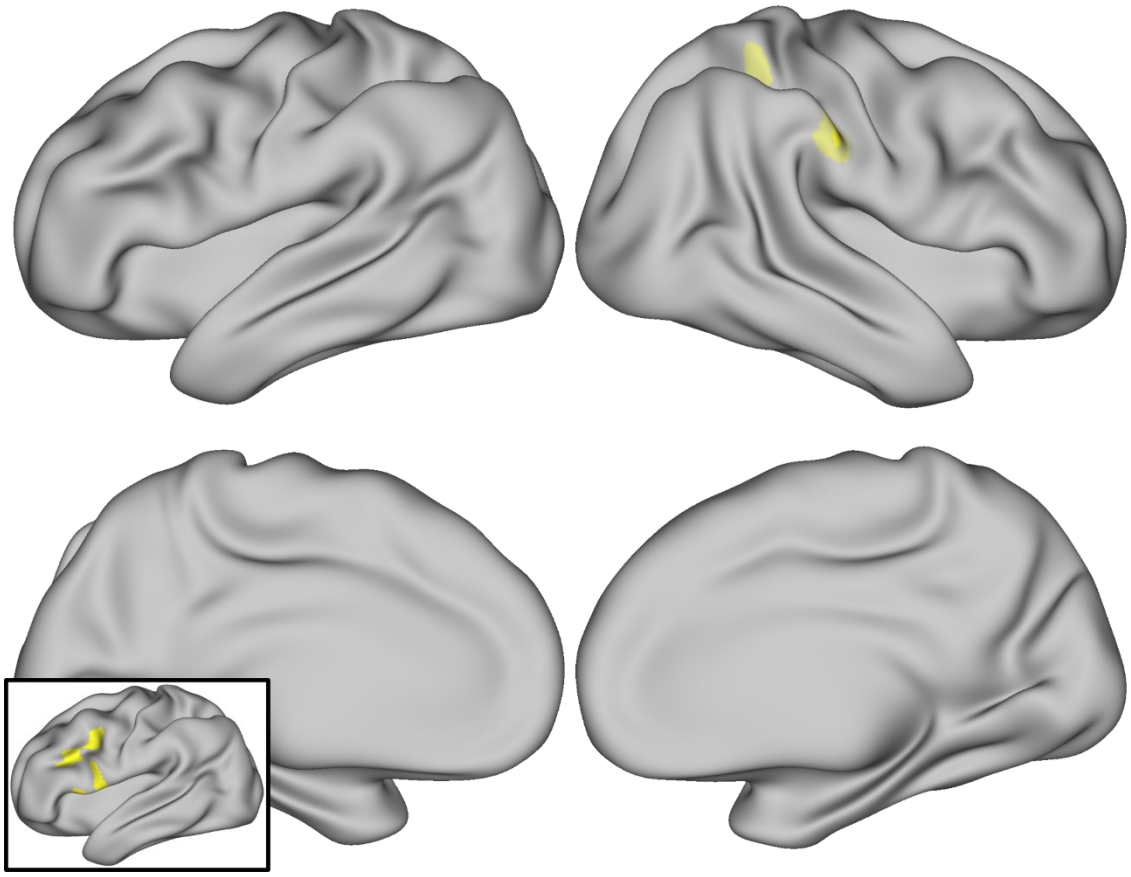

Figure 36: *Reduced correlations in M+A+ relative to M+A-. Vertex-wise global threshold of p < 0.001 uncorrected for multiple comparisons (brightly colored areas) and p < 0.01 uncorrected for multiple comparison (translucently colored areas). In yellow reduced correlations with ROIall are shown. In the lower left corner, the seed region ROIall, based on which the analysis was carried out is shown in yellow.*

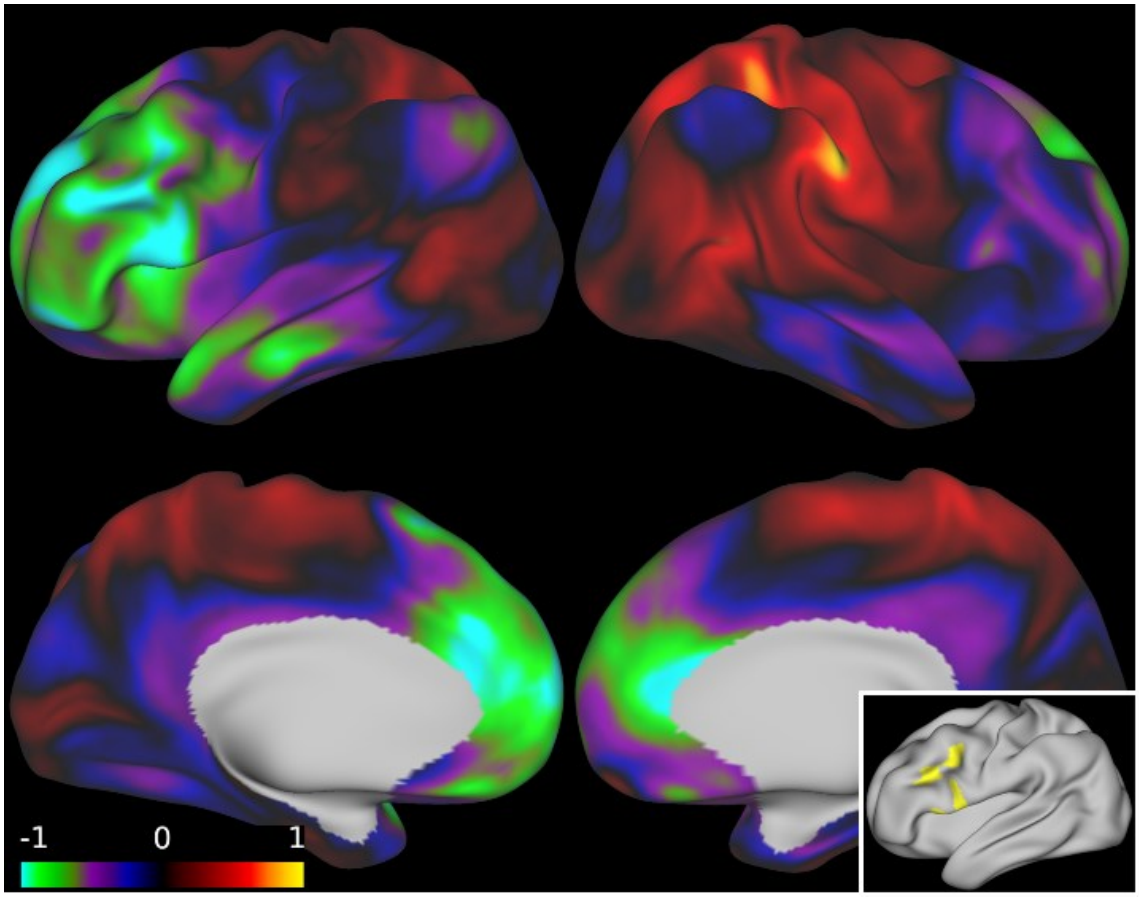

Figure 37: *Effect size map for the group comparison M+A+ relative to M+A-. The vertex-wise Cohen's d value is shown. Yellow indicates that there is a large effect size for the reduced correlations of M+A+ compared to M+A-, while green means that there is a large effect size for reduced correlations of M+A- compared to M+A+. The effect size map for the analysis with ROIall (bottom right corner) is shown.*

3.4.4.3 Reduced correlations in M+A- relative to M-A-

The between group analysis of M+A- vs. M-A- based on ROIall showed a large cluster with reduced correlations in the middle frontal gyrus and the anterior insula on the left hemisphere for a $p < 0.001$ uncorrected for multiple comparisons (Figure 38). Contralateral, several very small clusters were found diffusely distributed in the frontal cortex. In addition, there were reduced correlations in M+A- relative to M-A- in the intraparietal sulcus on the left and inferior parietal on the right. The effect size map (Figure 39) shows high effect sizes for reduced correlations in M+A- relative to M-A- in the area of the middle frontal gyrus and the insula, left more emphasized than on the right. High effect sizes were also found in the inferior parietal cortex and the anterior cingulate. The results of this

analysis were very similar to the results of the between group comparisons based on the 3 separate seed regions.

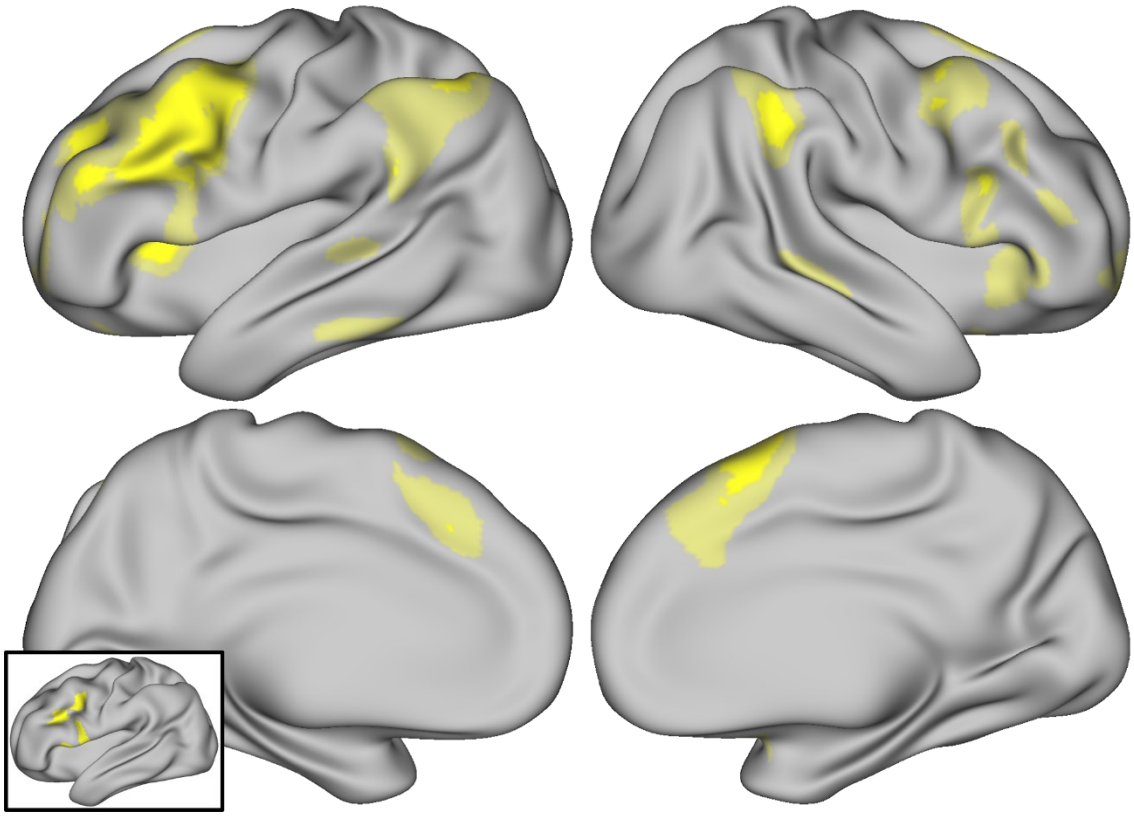

Figure 38: *Reduced correlations in M+A- relative to M-A-. Vertex-wise global threshold of p < 0.001 uncorrected for multiple comparisons (brightly colored areas) and p < 0.01 uncorrected for multiple comparison (translucently colored areas). In yellow reduced correlations with ROIall are shown. In the lower left corner, the seed region ROIall, based on which the analysis was carried out is shown in yellow.*

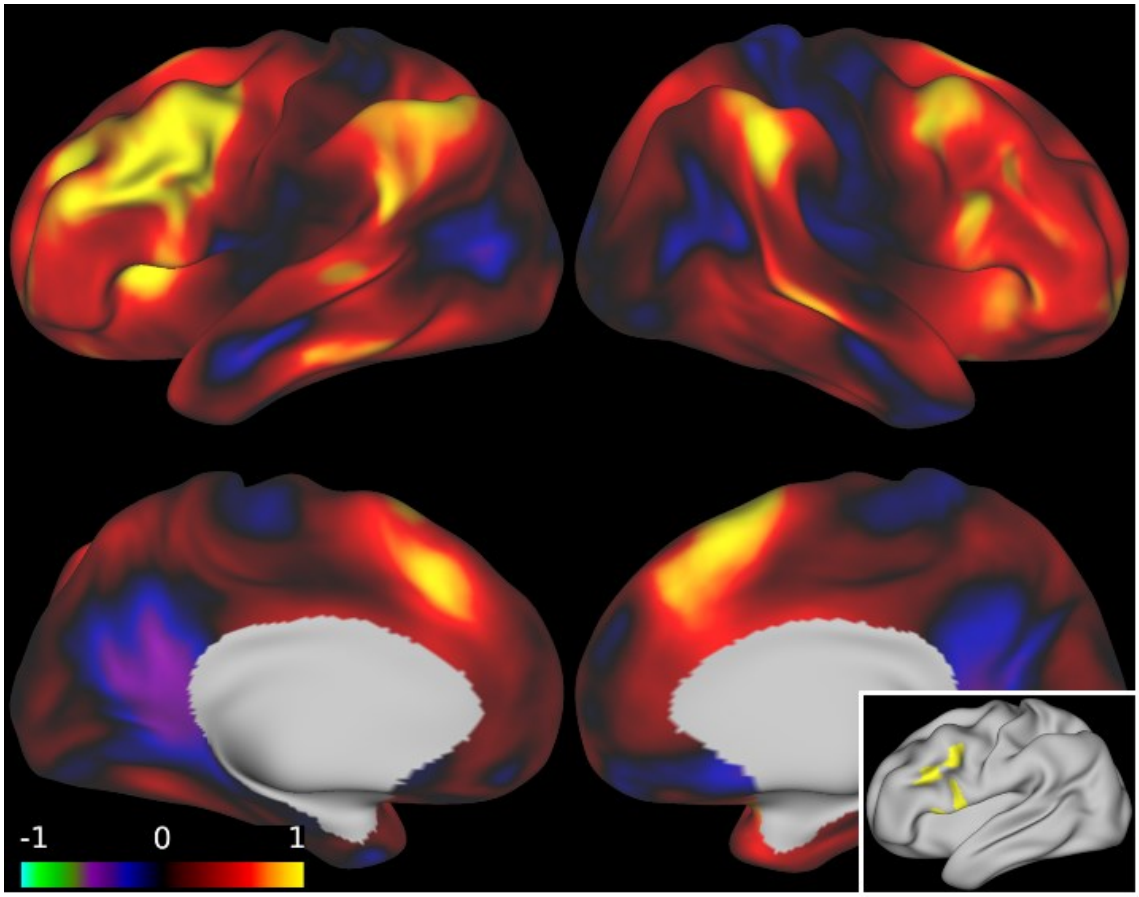

Figure 39: *Effect size map for the group comparison M+A+ relative to M+A-. The vertex-wise Cohen's d value is shown. Yellow indicates that there is a large effect size for the reduced correlations of M+A- compared to M-A-, while green means that there is a large effect size for reduced correlations of M-A- compared to M+A-. The effect size map for the analysis with ROIall (bottom right corner) is shown.*

3.4.5 Comparing our results with the stroke lesion map for apraxia

When comparing our results to the stroke lesion map for apraxia, it was noticeable that the clusters with reduced correlations in M+A+ relative to M-A- in the inferior parietal cortex corresponded to the stroke lesion map. In addition, the cluster with reduced correlations in the superior temporal gyrus also corresponded to the temporal extension of the stroke lesion map. However, in addition to these clusters, our results also showed clusters outside the stroke lesion map, such as in the intraparietal sulcus, premotor cortex and SMA.

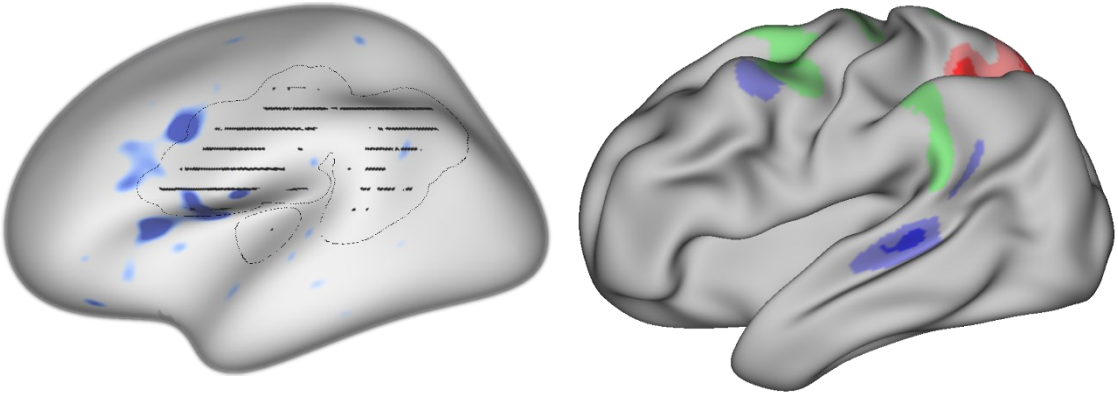

Figure 40: *On the left, the left hemisphere is shown with the areas in blue that show significantly reduced cortical thickness for M+A+ compared to M+A-. In addition, the inferior fronto-parietal region, whose damage correlates with the occurrence of apraxia after stroke, is depicted (shaded in black). (Wabersich-Flad, Doctoral thesis, Faculty of Medicine, Eberhard Karls Universität Tübingen, 2021). On the right, the left hemisphere with reduced correlations in M+A+ relative to M-A- is shown. Vertex-wise global threshold of p < 0.001 uncorrected for multiple comparisons (brightly colored areas) and p < 0.01 uncorrected for multiple comparisons (translucently colored areas). In red reduced correlations with ROI1, in green reduced correlations with ROI2 and in blue reduced correlations with ROI3.*

4 Discussion

I investigated the functional connectivity of three regions in the inferior frontal cortex that showed cortical atrophy specific to apraxia in patients with FTD to determine whether a disruption in the functional inferior frontoparietal network plays a role in the development of the symptom apraxia in FTD in addition to cortical degeneration. I explored the effect of different ICA denoising methods on the data during the preprocessing of the resting state fMRI data from the GenFI dataset. My analyses showed that manual ICA denoising yielded a highly significant noise reduction across the entire brain compared to no ICA denoising. Automatic ICA denoising with FIX through the HCP pipeline showed no significant difference in noise reduction compared to no ICA denoising. Looking at the subtraction images of the average correlation maps of all subjects the automatic HCP ICA denoising also showed a meaningful effect compared to no ICA denoising. However, this had to be considered with caution, as it was apparent when reviewing the correlation maps of individual subjects that no meaningful results were obtained by HCP ICA denoising for some subjects. Furthermore, when looking at the subtraction images, there was also a tendency for manual ICA denoising to achieve stronger denoising than HCP ICA denoising, but this effect was not significant. Due to the highly significant difference between manual ICA denoising and no ICA denoising and the advantage over HCP denoising, the following analyses were therefore performed with the manually ICA denoised data.

Based on the three cortical regions that had shown cortical degeneration in FTD patients specific to apraxia (Wabersich-Flad, Doctoral thesis, Faculty of Medicine, Eberhard Karls Universität Tübingen, 2021), seed-based correlation analyses were performed. Here, the inferior frontoparietal resting state network for cognitive motor control could be identified for all three groups, mutation carriers with apraxia, mutation carriers without apraxia and healthy control subjects. In each case, regions with high correlations to the seed regions were found in the inferior frontal cortex around the seed regions, in the intraparietal sulcus and supramarginal gyrus, and in the anterior cingulate.

In the between group comparisons, reduced correlations were found for mutation carriers with apraxia relative to healthy controls in the left inferior parietal area, as expected. Additionally, reduced correlations were found in the intraparietal sulcus, supramarginal gyrus and in posterior temporal regions on both hemispheres, as well as in the premotor and supplementary motor cortex. The results did not survive family-wise error rate correction for multiple comparisons. However, when looking at the effect size maps, high effect sizes were shown for reduced correlations in the intraparietal sulcus, supramarginal gyrus, SMA and premotor cortex on the right more than on the left, as well as temporally on the left. For the comparison of mutation carriers with apraxia with mutation carriers without apraxia, reduced correlations were found for M+A+ in the intraparietal sulcus on the right, inferior parietal and superior occipital on the right. However, these differences were also not significant when correcting for multiple comparisons. The effect size maps showed precisely these regions with high effect sizes. The between group comparisons of mutation carriers without apraxia with healthy control subjects showed reduced correlations for M+A- in the middle frontal gyrus and the anterior insula on the left more than on the right, as well as in the intraparietal sulcus and anterior cingulate. The effect size maps for these analyses showed high effect sizes in the middle frontal gyrus, anterior insula, intraparietal sulcus and anterior cingulate. The analyses performed with ROIall, the seed region that combined all 3 ROIs into one, found very similar results in all between group comparisons as seen by the analyses with the three individual seed regions.

Previous studies that have identified apraxia-related lesions in stroke patients typically find lesions in the left inferior frontal gyrus, adjacent insular cortex (Goldenberg and Karnath, 2006, Goldenberg et al., 2007, Buxbaum et al., 2014), and left middle frontal gyrus (Buxbaum et al., 2014, Haaland et al., 2000). The three regions with cortical atrophy specific for apraxia in FTD patients (Wabersich-Flad, Doctoral thesis, Faculty of Medicine, Eberhard Karls Universität Tübingen, 2021) are localized in these regions and were used for the seed-based correlation analyses, assuming that the functional network for action control that is affected in apraxia can be identified and thus also further regions that are

typically affected in stroke patients would be identified in patients with FTD. Indeed, the seed-based correlation analyses found high correlations around the seed regions in the middle and inferior frontal gyrus and for ROI2 and ROIall also in the adjacent insular lobe, which corresponds to the typical stroke regions (Goldenberg et al., 2007, Goldenberg and Karnath, 2006, Buxbaum et al., 2014). Furthermore, the correlation analyses based on ROI2 and ROIall found high correlations in the supramarginal left gyrus, which was identified by Buxbaum et al. (2014) as an important region for the kinematic component of gestures. The high correlations I found in the left intraparietal sulcus align with the results of Haaland et al. (2000), who found lesions in the left intraparietal sulcus in stroke patients with ideomotor limb apraxia with impaired imitation of gestures. Thus, it was possible to identify the functional network of action control in my study population, even for the group with neurodegenerative disease. The between group comparisons of M+A+ relative to M-A- showed reduced correlations in the group of mutation carriers with apraxia in the left inferior parietal cortex and supramarginal gyrus. This corresponds to the typical lesion patterns of stroke patients with apraxia (Goldenberg and Karnath, 2006, Buxbaum et al., 2014). Thus, in line with our hypothesis, a disruption of functional connectivity with the left inferior parietal cortex could be shown. Furthermore, reduced correlations were found in the left intraparietal sulcus, which also corresponds to typical stroke lesions (Haaland et al., 2000). The reduced correlations in the left posterior temporal gyrus are consistent with typical stroke lesions in the left middle posterior temporal gyrus (Goldenberg and Karnath, 2006, Buxbaum et al., 2014). Buxbaum et al. (2014) also found lesions in motor and premotor areas in stroke patients with impaired gesture tasks. In agreement with this, I found reduced correlations for M+A+ relative to M-A- in the left premotor and supplementary motor cortex.

The neural correlates of apraxia in FTD are not yet well understood. Johnen et al. (2016) investigated the neural correlates of limb apraxia in bvFTD and AD. They could not find significant results when examining bvFTD and AD individually. However, distinct regions of grey matter (GM) volume reduction for limb imitation and pantomime were identified for the entire dementia sample.

Bilateral atrophy of the superior, inferior and medial parietal cortex was found, which showed a significant correlation between limb imitation and GM volume. Large areas of the precuneus and posterior mid-cingulate cortex were also involved (Johnen et al., 2016). This is consistent with my own results, as I also found reduced correlations of M+A+ relative to M-A- in superior and inferior parietal areas in both hemispheres, as well as in the precuneus and posterior mid-cingulate cortex on the left. For object-pantomime, Johnen et al. (2016) identified GM volume reductions in the right middle temporal gyrus that extended into the middle occipital gyrus and further dorsally into the right inferior parietal lobe and angular gyrus. I found reduced correlations for mutation carriers with apraxia relative to healthy controls in the posterior middle temporal gyrus (pMTG) on the right hemisphere. Between group analyses of M+A+ relative to M+A- showed reduced correlations for M+A+ in the superior parietal cortex on the right and a very small cluster in the pMTG on the right. These results describe the mere effect of apraxia on the changes in connectivity of the network, since in this between-group comparison, the t-test was not performed against healthy subjects, where the mutation of genetic FTD could still have had an influence on the results, but against mutation carriers without apraxia, so that apraxia was the only discriminating factor here. The effect size maps of the between group analyses of M+A+ relative to M+A- showed mainly high effect sizes in the area of the intraparietal sulcus on the right, but these also extended into the intraparietal sulcus of the left hemisphere. Comparing these results with the results of Johnen et al. (2016) for limb imitation, a high degree of similarity between the results is noticeable, especially in the superior parietal lobe on the right hemisphere. In contrast to Johnen et al. (2016), I found less extensive results in the left hemisphere, whereas Johnen et al. (2016) found the maximum GM volume reduction for limb imitation here. Thus, my results are somewhat more right-lateralized. The between group comparison of M+A+ with M+A- also showed high effect sizes for reduced correlations for M+A+ in the right pMTG extending into the middle occipital gyrus. Johnen et al. (2016) found these same regions for object-pantomime. Unlike the study population of Johnen et al. (2016), in which patients with clinical bvFTD were included, the special feature of the GenFI

sample is that only patients with genetically confirmed FTD are included. Moreover, in Johnen et al. (2016), patients with AD were also included in the evaluation of the results, so that not the mere effect of FTD could be shown here, but rather the changes that were common to bvFTD and AD. In contrast, the GenFI population has the advantage that by recruiting genetically confirmed FTD patients, it is clear that it is FTD and no atypical presentation of another neurological disease. In addition, my study showed the neural correlates of apraxia in FTD alone and not in combination with AD. Interestingly, despite these systematic differences in patient recruitment, the regions found in the superior parietal lobe and the right pMTG correspond very well. Thus, very similar regions were found that are related to apraxia in neurodegenerative diseases. In contrast to the typical stroke lesions, both my results and the results of Johnen et al. (2016) showed damage to the right parietal lobe. Stroke lesion studies have so far typically found damage to the left frontoparietal-temporal network (Buxbaum and Randerath, 2018). Furthermore, the lesions found by Johnen et al. (2016) and myself in the left parietal lobe were more posterior than the typical stroke lesions in the inferior frontal and parietal lobes (Goldenberg and Karnath, 2006).

However, regarding the large discrepancy that the vast majority of recent studies on neural correlates of apraxia symptoms in stroke have not found correlates in the right hemisphere, it is also interesting to look at fMRI studies of healthy subjects regarding imitation. Unfortunately, there is no clear standard within the GenFI consortium on how apraxia should be diagnosed. However, imitation of meaningless hand gestures is commonly used for diagnosis. Therefore, my findings on the functional network for apraxia are most likely based on problems with imitation and should therefore be compared with fMRI studies that deal with imitation. fMRI studies in healthy subjects indicate bilateral neuronal activation for imitation. In their meta-analysis of 20 fMRI studies, Molenberghs et al. (2009) investigated the role of the frontal and parietal brain regions for imitation. They found significant activation in the superior and inferior parietal lobes and in dorsal parts of the premotor cortex in both hemispheres. Consistent with these results are the high effect sizes I found for reduced correlations for M+A+ relative to M+A- in the area of the intraparietal sulcus, as well as reduced correlations for

M+A+ relative to M-A- in the premotor cortex in both hemispheres. In their meta-analysis of 139 fMRI and PET studies, Caspers et al. (2010) also demonstrated a bilateral network in the frontal premotor, parietal and temporo-occipital cortex for action-observation and imitation.

So far, there is controversy in the literature as to whether there is lateralization for the action imitation network, as there is contradictory evidence from previous studies. My results suggest the presence of a bilateral network, whereas the majority of studies on neural correlates of apraxia in stroke patients could not find involvement of the right hemisphere. The question therefore arises whether the results from stroke lesions are actually the more valid results or whether it is an advantage to investigate the neuronal correlates of apraxia on the basis of neuronal degeneration. The disadvantage of stroke lesion studies is that there is always a regional bias due to the territory of the affected artery. In most cases, patients studied are those with an infarct in the middle cerebral artery. Thus, it may well be that the discrepancy between the more ventrally located lesions in the inferior frontal and inferior parietal cortex for stroke patients with apraxia in contrast to the more posterior damage in Johnen et al. (2016) and the current study come about. Stroke data could show inferior parietal regions disproportionately often, as these are mainly supplied by the middle cerebral artery. It is possible that brain areas relevant for apraxia in neurodegenerative diseases extend beyond the regions supplied by the middle cerebral artery and that these cannot be detected due to the spatial bias of the vascular supply in stroke studies. In contrast to stroke studies, neuronal degenerative diseases have the advantage that there is no regional bias due to vascular supply. There is also a regional bias for neuronal degeneration, as FTD usually starts with atrophy fronto-temporally, while AD is typically characterized by degeneration in the posterior parietal network (Rabinovici et al., 2007). The progression of the atrophy pattern in FTD from initial insular and temporal cortices, to the frontal cortex and subcortical areas, then parietal and cingulate cortices, and finally occipital cortex and cerebellum (Rohrer et al., 2015), could cause a regional bias depending on the stage of the disease at which the neural correlates of apraxia are examined. However, it is interesting to note that for the combined study

population of AD and bvFTD by Johnen et al. (2016), very similar neural correlates for apraxia could be found as for my study population, which only included patients with genetic FTD. Another advantage of this study over stroke-based studies is that I investigated the functional connectivity of all regions of the cortex and was not limited to the region affected by stroke. Further research should therefore be conducted using neuronal degenerations, as these may reflect the true extent of the neuronal correlates for apraxia more completely and without the regional biases of stroke lesion maps. The strong involvement of the right hemisphere in apraxia in FTD and AD could possibly also be due to stronger deficits in visuospatial and attentional impairments, while in left hemispheric stroke patients, deficits in pantomime and comorbid aphasia are more likely to be due to deficits in semantic memory and linguistic abilities (Johnen et al., 2016). The similar clinical presentation of apraxia could therefore be based on different causes in stroke and FTD and hence show different neuronal correlates.

Limitations of this study are that in the between group comparisons with a FWER correction for multiple testing, no significant results were found. However, this study revealed large effect sizes for the reduced correlations of M+A+ relative to M-A- and M+A-. Cohen (1992) defined the effect sizes for t-tests of the difference between independent means as d=0.20 being a small effect size, d=0.50 a medium effect size and 0.80 as a large effect size. Accordingly, for the between group comparison of M+A+ with M+A-, large effect sizes were found in the area of the intraparietal sulcus on the right and the pMTG on the right, and medium effect sizes in the intraparietal sulcus on the left and pMTG on the left. Based on the effect size maps, it could therefore be shown that there is a relevant difference in the correlations between the groups, even though no significant p-values for the reductions in correlations in the functional network for apraxia could be found. This is probably due to the very small individual groups. In the GenFI datafreeze of 2017, there were only 31 subjects who are mutation carriers and have apraxia. Unfortunately, comparable resting state fMRI data were not available for all subjects, or there were problems during the preprocessing, so the analyses could only be performed with 22 mutation carriers with apraxia. The p-value is highly dependent on the sample size and gives no indication of the strength of a

difference between the means of two groups. Accordingly, the large differences in correlations between the groups, which could be proven by the effect sizes, are presumably not significant due to the very small sample sizes. In addition, when examining the corrected p-values of the between-group analyses, it must be considered that the FWER correction performed by PALM calculates permutation-adjusted p-values for step-down multiple testing procedures (Winkler et al., 2014). However, this method of correction for multiple testing assumes that all tests performed are independent of each other, which is not the case in rs-fMRI data, as neighboring voxels are functionally related, especially if spatial smoothing has been performed previously, as it had in this study. Moreover, this permutation-based correction is very close to a Bonferroni correction for large datasets. Hence, this performed correction for multiple testing is very conservative. This study lays a foundation for further studies, as it was able to show that reduced correlations do exist for mutation carriers with apraxia, but these cannot yet be conclusively assessed at present, as the sample size is still too small. The GenFI consortium is a prospective study, so it would make sense to carry out these analyses again as soon as more data is available and significant differences between the groups can be determined.

A methodological limitation of this study is the lack of clearly defined diagnostic criteria for apraxia within the GenFI consortium. There is no clear protocol by which the investigators diagnose apraxia. In most cases, diagnosis is based on the imitation of meaningless gestures. However, imitation of gestures is only part of the functions that may be impaired in apraxia. Goldenberg (2014) divides the core manifestations of apraxia into difficulties in imitating gestures, use of single tool and object and production of communicative gestures on command. Thus, it is problematic to apply only a subset of these manifestations to diagnose apraxia, as previous studies have also shown that these specific subcategories of apraxia show different correlates of brain regions (Buxbaum et al., 2014, Goldenberg et al., 2007, Goldenberg and Karnath, 2006). To enable better comparability of the neural correlates of apraxia in FTD with the neural correlates of apraxia in stroke, it would therefore be necessary to establish a uniform test battery within the GenFI consortium that examines all facets of apraxia in a standardized manner.

5 Summary

The neural correlates of apraxia in neurodegenerative diseases such as FTD are not yet well understood and researched, although neuropsychological deficits such as apraxia are quite frequent in these diseases. Based on previously identified atrophic areas of the cerebral cortex in the inferior frontal cortex that are relevant to apraxia in genetic FTD, I identified the functional network of apraxia with seed-based correlation analyses and showed that, in addition to the cortical atrophy of the frontal cortex, changes in functional connectivity, especially in the intraparietal sulcus on the right and in the pMTG on the right, probably also contribute to the development of the symptom apraxia in genetic FTD. My results suggest the presence of a bilateral action control network, whereas most studies on neural correlates of apraxia in stroke patients have not found involvement of the right hemisphere. These results contribute to the already prevailing controversial discussion in the literature about the lateralization of the action control network to the left hemisphere. In addition, my work investigated the advantages and disadvantages of different ICA denoising methods and was able to show for the dataset used here, which deviates from the standards of the Human Connectome Project and includes patients with a neurodegenerative disease, that a manual classification provides better cleanup of the data. My work thus contributes to scientific research in the field of apraxia, familial FTD, as well as the general context of neuropsychological deficits and their neural correlates.

6 Zusammenfassung

Die neuronalen Korrelate von Apraxie in neurodegenerativen Erkrankungen wie FTD sind bisher noch nicht gut verstanden und erforscht, obwohl neuropsychologische Defizite wie Apraxie bei diesen Erkrankungen relativ häufig sind. Ausgehend von zuvor identifizierten atrophischen Arealen der Hirnrinde im inferior frontalen Kortex, die für Apraxie bei genetischer FTD relevant sind, konnte ich mit seed basierten Korrelationsanalysen das funktionelle Netzwerk der Apraxie identifizieren und zeigen, dass neben der kortikalen Atrophie des frontalen Kortex vermutlich auch Veränderungen der funktionellen Konnektivität vor allem im intraparietalen Sulcus rechts und im im posterioren Gyrus temporalis medialis rechts zu der Ausbildung des Symptoms Apraxie bei genetischer FTD beitragen. Meine Ergebnisse deuten auf das Vorhandensein eines bilateralen Handlungskontrollnetzwerks hin, während die meisten Studien über neuronale Korrelate der Apraxie bei Schlaganfallpatienten keine Beteiligung der rechten Hemisphäre feststellen konnten. Diese Ergebnisse tragen somit zu der in der Literatur bereits vorherrschenden kontroversen Diskussion über die Lateralisierung des Handlungskontrollnetzwerks auf die linke Hemisphäre bei. Darüber hinaus untersuchte meine Arbeit die Vor- und Nachteile verschiedener ICA Denoising Methoden und konnte für den hier verwendeten Datensatz, der von den Standards des Human Connectome Project abweicht und Patienten mit einer neurodegenerativen Erkrankung umfasst, zeigen, dass eine manuelle Klassifizierung eine bessere Bereinigung der Daten ermöglicht. Meine Arbeit trägt somit zur wissenschaftlichen Forschung im Bereich Apraxie, familiärer FTD, sowie den generellen Zusammenhängen von neuropsychologischen Defiziten und deren neuronalen Korrelaten bei.

7 List of literature

BIJSTERBOSCH, J., SMITH, S., BECKMANN, C. & OXFORD UNIVERSITY PRESS 2017. *Introduction to resting state fMRI functional connectivity,* Oxford, United Kingdom, Oxford University Press.

BISWAL, B., YETKIN, F. Z., HAUGHTON, V. M. & HYDE, J. S. 1995. Functional connectivity in the motor cortex of resting human brain using echo-planar MRI. *Magn Reson Med,* 34**,** 537-41.

BRIDEL, C., VAN WIERINGEN, W. N., ZETTERBERG, H., TIJMS, B. M., TEUNISSEN, C. E., AND THE, N. F. L. G., ALVAREZ-CERMENO, J. C., ANDREASSON, U., AXELSSON, M., BACKSTROM, D. C., BARTOS, A., BJERKE, M., BLENNOW, K., BOXER, A., BRUNDIN, L., BURMAN, J., CHRISTENSEN, T., FIALOVA, L., FORSGREN, L., FREDERIKSEN, J. L., GISSLEN, M., GRAY, E., GUNNARSSON, M., HALL, S., HANSSON, O., HERBERT, M. K., JAKOBSSON, J., JESSEN-KRUT, J., JANELIDZE, S., JOHANNSSON, G., JONSSON, M., KAPPOS, L., KHADEMI, M., KHALIL, M., KUHLE, J., LANDEN, M., LEINONEN, V., LOGROSCINO, G., LU, C. H., LYCKE, J., MAGDALINOU, N. K., MALASPINA, A., MATTSSON, N., MEETER, L. H., MEHTA, S. R., MODVIG, S., OLSSON, T., PATERSON, R. W., PEREZ-SANTIAGO, J., PIEHL, F., PIJNENBURG, Y. A. L., PYYKKO, O. T., RAGNARSSON, O., ROJAS, J. C., ROMME CHRISTENSEN, J., SANDBERG, L., SCHERLING, C. S., SCHOTT, J. M., SELLEBJERG, F. T., SIMONE, I. L., SKILLBACK, T., STILUND, M., SUNDSTROM, P., SVENNINGSSON, A., TORTELLI, R., TORTORELLA, C., TRENTINI, A., TROIANO, M., TURNER, M. R., VAN SWIETEN, J. C., VAGBERG, M., VERBEEK, M. M., VILLAR, L. M., VISSER, P. J., WALLIN, A., WEISS, A., WIKKELSO, C. & WILD, E. J. 2019. Diagnostic Value of Cerebrospinal Fluid Neurofilament Light Protein in Neurology: A Systematic Review and Meta-analysis. *JAMA Neurol,* 76**,** 1035-1048.

BUXBAUM, L. J. & RANDERATH, J. 2018. Limb apraxia and the left parietal lobe. *Handb Clin Neurol,* 151**,** 349-363.

BUXBAUM, L. J., SHAPIRO, A. D. & COSLETT, H. B. 2014. Critical brain regions for tool-related and imitative actions: a componential analysis. *Brain,* 137**,** 1971-85.

CABALLERO-GAUDES, C. & REYNOLDS, R. C. 2017. Methods for cleaning the BOLD fMRI signal. *Neuroimage,* 154**,** 128-149.

CASPERS, S., ZILLES, K., LAIRD, A. R. & EICKHOFF, S. B. 2010. ALE meta-analysis of action observation and imitation in the human brain. *Neuroimage,* 50**,** 1148-67.

CHOW, T. W., MILLER, B. L., HAYASHI, V. N. & GESCHWIND, D. H. 1999. Inheritance of frontotemporal dementia. *Arch Neurol,* 56**,** 817-22.

COHEN, J. 1992. A power primer. *Psychol Bull,* 112**,** 155-9.

CUBELLI, R. 2017. Definition: Apraxia. *Cortex,* 93**,** 227.

DE BLASI, B., CACIAGLI, L., STORTI, S. F., GALOVIC, M., KOEPP, M., MENEGAZ, G., BARNES, A. & GALAZZO, I. B. 2020. Noise removal in resting-state and task fMRI: functional connectivity and activation maps. *J Neural Eng,* 17**,** 046040.

DEVENNEY, E. M., AHMED, R. M. & HODGES, J. R. 2019. Frontotemporal dementia. *Handb Clin Neurol,* 167**,** 279-299.
DU, A. T., SCHUFF, N., KRAMER, J. H., ROSEN, H. J., GORNO-TEMPINI, M. L., RANKIN, K., MILLER, B. L. & WEINER, M. W. 2007. Different regional patterns of cortical thinning in Alzheimer's disease and frontotemporal dementia. *Brain,* 130**,** 1159-66.
FISCHL, B., SALAT, D. H., BUSA, E., ALBERT, M., DIETERICH, M., HASELGROVE, C., VAN DER KOUWE, A., KILLIANY, R., KENNEDY, D., KLAVENESS, S., MONTILLO, A., MAKRIS, N., ROSEN, B. & DALE, A. M. 2002. Whole brain segmentation: automated labeling of neuroanatomical structures in the human brain. *Neuron,* 33**,** 341-55.
FOUNDAS, A. L. 2013. Apraxia: neural mechanisms and functional recovery. *Handb Clin Neurol,* 110**,** 335-45.
FOUNDAS, A. L. & DUNCAN, E. S. 2019. Limb Apraxia: a Disorder of Learned Skilled Movement. *Curr Neurol Neurosci Rep,* 19**,** 82.
GLASSER, M. F., SOTIROPOULOS, S. N., WILSON, J. A., COALSON, T. S., FISCHL, B., ANDERSSON, J. L., XU, J., JBABDI, S., WEBSTER, M., POLIMENI, J. R., VAN ESSEN, D. C., JENKINSON, M. & CONSORTIUM, W. U.-M. H. 2013. The minimal preprocessing pipelines for the Human Connectome Project. *Neuroimage,* 80**,** 105-24.
GOLDENBERG, G. 2014. Apraxia - the cognitive side of motor control. *Cortex,* 57**,** 270-4.
GOLDENBERG, G., HERMSDORFER, J., GLINDEMANN, R., RORDEN, C. & KARNATH, H. O. 2007. Pantomime of tool use depends on integrity of left inferior frontal cortex. *Cereb Cortex,* 17**,** 2769-76.
GOLDENBERG, G. & KARNATH, H. O. 2006. The neural basis of imitation is body part specific. *J Neurosci,* 26**,** 6282-7.
GREAVES, C. V. & ROHRER, J. D. 2019. An update on genetic frontotemporal dementia. *J Neurol,* 266**,** 2075-2086.
GRIFFANTI, L., DOUAUD, G., BIJSTERBOSCH, J., EVANGELISTI, S., ALFARO-ALMAGRO, F., GLASSER, M. F., DUFF, E. P., FITZGIBBON, S., WESTPHAL, R., CARONE, D., BECKMANN, C. F. & SMITH, S. M. 2017. Hand classification of fMRI ICA noise components. *Neuroimage,* 154**,** 188-205.
GRIFFANTI, L., SALIMI-KHORSHIDI, G., BECKMANN, C. F., AUERBACH, E. J., DOUAUD, G., SEXTON, C. E., ZSOLDOS, E., EBMEIER, K. P., FILIPPINI, N., MACKAY, C. E., MOELLER, S., XU, J., YACOUB, E., BASELLI, G., UGURBIL, K., MILLER, K. L. & SMITH, S. M. 2014. ICA-based artefact removal and accelerated fMRI acquisition for improved resting state network imaging. *Neuroimage,* 95**,** 232-47.
HAALAND, K. Y., HARRINGTON, D. L. & KNIGHT, R. T. 2000. Neural representations of skilled movement. *Brain,* 123 (Pt 11)**,** 2306-13.
JOHNEN, A., BRANDSTETTER, L., KARGEL, C., WIENDL, H., LOHMANN, H. & DUNING, T. 2016. Shared neural correlates of limb apraxia in early stages of Alzheimer's dementia and behavioural variant frontotemporal dementia. *Cortex,* 84**,** 1-14.
KELLY, R. E., JR., ALEXOPOULOS, G. S., WANG, Z., GUNNING, F. M., MURPHY, C. F., MORIMOTO, S. S., KANELLOPOULOS, D., JIA, Z., LIM,

K. O. & HOPTMAN, M. J. 2010. Visual inspection of independent components: defining a procedure for artifact removal from fMRI data. *J Neurosci Methods,* 189**,** 233-45.
KOVACS, G. G. 2017. Tauopathies. *Handb Clin Neurol,* 145**,** 355-368.
LIKEMAN, M., ANDERSON, V. M., STEVENS, J. M., WALDMAN, A. D., GODBOLT, A. K., FROST, C., ROSSOR, M. N. & FOX, N. C. 2005. Visual assessment of atrophy on magnetic resonance imaging in the diagnosis of pathologically confirmed young-onset dementias. *Arch Neurol,* 62**,** 1410-5.
LV, H., WANG, Z., TONG, E., WILLIAMS, L. M., ZAHARCHUK, G., ZEINEH, M., GOLDSTEIN-PIEKARSKI, A. N., BALL, T. M., LIAO, C. & WINTERMARK, M. 2018. Resting-State Functional MRI: Everything That Nonexperts Have Always Wanted to Know. *AJNR Am J Neuroradiol,* 39**,** 1390-1399.
MASTERS, C. L., BATEMAN, R., BLENNOW, K., ROWE, C. C., SPERLING, R. A. & CUMMINGS, J. L. 2015. Alzheimer's disease. *Nat Rev Dis Primers,* 1**,** 15056.
MOLENBERGHS, P., CUNNINGTON, R. & MATTINGLEY, J. B. 2009. Is the mirror neuron system involved in imitation? A short review and meta-analysis. *Neurosci Biobehav Rev,* 33**,** 975-80.
NEARY, D., SNOWDEN, J. S., GUSTAFSON, L., PASSANT, U., STUSS, D., BLACK, S., FREEDMAN, M., KERTESZ, A., ROBERT, P. H., ALBERT, M., BOONE, K., MILLER, B. L., CUMMINGS, J. & BENSON, D. F. 1998. Frontotemporal lobar degeneration: a consensus on clinical diagnostic criteria. *Neurology,* 51**,** 1546-54.
OLNEY, N. T., SPINA, S. & MILLER, B. L. 2017. Frontotemporal Dementia. *Neurol Clin,* 35**,** 339-374.
PARK, J. E. 2017. Apraxia: Review and Update. *J Clin Neurol,* 13**,** 317-324.
RABINOVICI, G. D., SEELEY, W. W., KIM, E. J., GORNO-TEMPINI, M. L., RASCOVSKY, K., PAGLIARO, T. A., ALLISON, S. C., HALABI, C., KRAMER, J. H., JOHNSON, J. K., WEINER, M. W., FORMAN, M. S., TROJANOWSKI, J. Q., DEARMOND, S. J., MILLER, B. L. & ROSEN, H. J. 2007. Distinct MRI atrophy patterns in autopsy-proven Alzheimer's disease and frontotemporal lobar degeneration. *Am J Alzheimers Dis Other Demen,* 22**,** 474-88.
RATNAVALLI, E., BRAYNE, C., DAWSON, K. & HODGES, J. R. 2002. The prevalence of frontotemporal dementia. *Neurology,* 58**,** 1615-21.
ROHRER, J. D., GUERREIRO, R., VANDROVCOVA, J., UPHILL, J., REIMAN, D., BECK, J., ISAACS, A. M., AUTHIER, A., FERRARI, R., FOX, N. C., MACKENZIE, I. R., WARREN, J. D., DE SILVA, R., HOLTON, J., REVESZ, T., HARDY, J., MEAD, S. & ROSSOR, M. N. 2009. The heritability and genetics of frontotemporal lobar degeneration. *Neurology,* 73**,** 1451-6.
ROHRER, J. D., NICHOLAS, J. M., CASH, D. M., VAN SWIETEN, J., DOPPER, E., JISKOOT, L., VAN MINKELEN, R., ROMBOUTS, S. A., CARDOSO, M. J., CLEGG, S., ESPAK, M., MEAD, S., THOMAS, D. L., DE VITA, E., MASELLIS, M., BLACK, S. E., FREEDMAN, M., KEREN, R., MACINTOSH, B. J., ROGAEVA, E., TANG-WAI, D., TARTAGLIA, M. C., LAFORCE, R., JR., TAGLIAVINI, F., TIRABOSCHI, P., REDAELLI, V.,

PRIONI, S., GRISOLI, M., BORRONI, B., PADOVANI, A., GALIMBERTI, D., SCARPINI, E., ARIGHI, A., FUMAGALLI, G., ROWE, J. B., COYLE-GILCHRIST, I., GRAFF, C., FALLSTROM, M., JELIC, V., STAHLBOM, A. K., ANDERSSON, C., THONBERG, H., LILIUS, L., FRISONI, G. B., PIEVANI, M., BOCCHETTA, M., BENUSSI, L., GHIDONI, R., FINGER, E., SORBI, S., NACMIAS, B., LOMBARDI, G., POLITO, C., WARREN, J. D., OURSELIN, S., FOX, N. C., ROSSOR, M. N. & BINETTI, G. 2015. Presymptomatic cognitive and neuroanatomical changes in genetic frontotemporal dementia in the Genetic Frontotemporal dementia Initiative (GENFI) study: a cross-sectional analysis. *Lancet Neurol,* 14**,** 253-62.

ROHRER, J. D. & WARREN, J. D. 2011. Phenotypic signatures of genetic frontotemporal dementia. *Curr Opin Neurol,* 24**,** 542-9.

ROHRER, J. D., WARREN, J. D., FOX, N. C. & ROSSOR, M. N. 2013. Presymptomatic studies in genetic frontotemporal dementia. *Rev Neurol (Paris),* 169**,** 820-4.

RUMMEL, C., VERMA, R. K., SCHOPF, V., ABELA, E., HAUF, M., BERRUECOS, J. F. & WIEST, R. 2013. Time course based artifact identification for independent components of resting-state FMRI. *Front Hum Neurosci,* 7**,** 214.

SALIMI-KHORSHIDI, G., DOUAUD, G., BECKMANN, C. F., GLASSER, M. F., GRIFFANTI, L. & SMITH, S. M. 2014. Automatic denoising of functional MRI data: combining independent component analysis and hierarchical fusion of classifiers. *Neuroimage,* 90**,** 449-68.

SEELAAR, H., KAMPHORST, W., ROSSO, S. M., AZMANI, A., MASDJEDI, R., DE KONING, I., MAAT-KIEVIT, J. A., ANAR, B., DONKER KAAT, L., BREEDVELD, G. J., DOOIJES, D., ROZEMULLER, J. M., BRONNER, I. F., RIZZU, P. & VAN SWIETEN, J. C. 2008. Distinct genetic forms of frontotemporal dementia. *Neurology,* 71**,** 1220-6.

SEELAAR, H., ROHRER, J. D., PIJNENBURG, Y. A., FOX, N. C. & VAN SWIETEN, J. C. 2011. Clinical, genetic and pathological heterogeneity of frontotemporal dementia: a review. *J Neurol Neurosurg Psychiatry,* 82**,** 476-86.

SMITHA, K. A., AKHIL RAJA, K., ARUN, K. M., RAJESH, P. G., THOMAS, B., KAPILAMOORTHY, T. R. & KESAVADAS, C. 2017. Resting state fMRI: A review on methods in resting state connectivity analysis and resting state networks. *Neuroradiol J,* 30**,** 305-317.

SNOWDEN, J. S., NEARY, D. & MANN, D. M. 2002. Frontotemporal dementia. *Br J Psychiatry,* 180**,** 140-3.

SWIFT, I. J., SOGORB-ESTEVE, A., HELLER, C., SYNOFZIK, M., OTTO, M., GRAFF, C., GALIMBERTI, D., TODD, E., HESLEGRAVE, A. J., VAN DER ENDE, E. L., VAN SWIETEN, J. C., ZETTERBERG, H. & ROHRER, J. D. 2021. Fluid biomarkers in frontotemporal dementia: past, present and future. *J Neurol Neurosurg Psychiatry,* 92**,** 204-215.

VAN DER ENDE, E. L. & VAN SWIETEN, J. C. 2021. Fluid Biomarkers of Frontotemporal Lobar Degeneration. *Adv Exp Med Biol,* 1281**,** 123-139.

WABERSICH-FLAD, D. D. & EBERHARD KARLS UNIVERSITÄT TÜBINGEN 2021. MRI substrates of specific neuropsychological dysfunctions within

and across FTD genotypes at the presymptomatic and symptomatic disease stage. Tübingen.
WARREN, J. D., ROHRER, J. D. & ROSSOR, M. N. 2013. Clinical review. Frontotemporal dementia. *BMJ,* 347**,** f4827.
WHITWELL, J. L., JOSEPHS, K. A., AVULA, R., TOSAKULWONG, N., WEIGAND, S. D., SENJEM, M. L., VEMURI, P., JONES, D. T., GUNTER, J. L., BAKER, M., WSZOLEK, Z. K., KNOPMAN, D. S., RADEMAKERS, R., PETERSEN, R. C., BOEVE, B. F. & JACK, C. R., JR. 2011. Altered functional connectivity in asymptomatic MAPT subjects: a comparison to bvFTD. *Neurology,* 77**,** 866-74.
WINKLER, A. M., RIDGWAY, G. R., WEBSTER, M. A., SMITH, S. M. & NICHOLS, T. E. 2014. Permutation inference for the general linear model. *Neuroimage,* 92**,** 381-97.
YLIRANTA, A. & JEHKONEN, M. 2020. Limb and face apraxias in frontotemporal dementia: A systematic scoping review. *Cortex,* 129**,** 529-547.
ZHOU, J., GREICIUS, M. D., GENNATAS, E. D., GROWDON, M. E., JANG, J. Y., RABINOVICI, G. D., KRAMER, J. H., WEINER, M., MILLER, B. L. & SEELEY, W. W. 2010. Divergent network connectivity changes in behavioural variant frontotemporal dementia and Alzheimer's disease. *Brain,* 133**,** 1352-67.

8 Erklärung zum Eigenanteil

Die Arbeit wurde im Hertie-Institut für klinische Hirnforschung unter Betreuung von Marc Himmelbach durchgeführt. Die Konzeption der Studie erfolgte in Zusammenarbeit mit Marc Himmelbach. Die in der Arbeit beschriebene Datensatzaufbereitung wurde nach Einarbeitung durch Amin Dadashi von mir durchgeführt. Die statistische Auswertung erfolgte nach Beratung mit Marc Himmelbach durch mich. Ich versichere, das Manuskript selbständig verfasst zu haben und keine weiteren als die von mir angegebenen Quellen verwendet zu haben.

Tübingen, den 26.06.2023